Chair of Ferrous Metallurgy

Doctoral Thesis

Measurement of diffusion and activity coefficients in slags

Dipl.-Ing. Alexander Halwax, BSc

February 2024

MONTANUNIVERSITÄT LEOBEN
www.unileoben.ac.at

AFFIDAVIT

I declare on oath that I wrote this thesis independently, did not use any sources and aids other than those specified, have fully and truthfully reported the use of generative methods and models of artificial intelligence, and did not otherwise use any other unauthorized aids.

I declare that I have read, understood and complied with the "Good Scientific Practice" of the Montanuniversität Leoben.

Furthermore, I declare that the electronic and printed versions of the submitted thesis are identical in form and content.

Date 22.02.2024

Halwax

Signature Author
Alexander Halwax

Abstract

Slags are important in iron and crude steel making as well as in secondary metallurgical treatments. Slag properties, such as viscosity, density, liquidus temperature, oxidation potential, foaming behavior, etc., have a significant influence on the efficiency of metallurgical processes. These properties are largely defined by the slag composition. The slag composition is adjusted in all metallurgical processes by the addition of additives. These are usually CaO- and/or MgO-containing additives. Knowledge of diffusion coefficients of the respective oxide in slags is necessary to describe dissolution processes of additives in slags and therefore to optimize existing processes or develop new ones. Furthermore, the knowledge of thermodynamic activities of individual slag components is of great interest for understanding and optimizing metallurgical processes. A low activity of the species to be extracted (e.g. P or S) in the slag leads to an efficient removal of these components from the steel. The capacity of slags to absorb unwanted steel by-elements is influenced by the composition of the slag. The determination of these two parameters (diffusion coefficient and activity) in slags was the objective of this work.

For the investigation of diffusion coefficients in slags, an experimental setup was designed which allows dissolution experiments to be carried out under reproducible conditions. In addition to the construction of the experimental setup, a calculation model was developed, which enables the calculation of the diffusion coefficient from the data of the dissolution tests. This model includes a density model and five different viscosity models. Since each viscosity model is valid for a certain temperature and composition range, it was necessary to use several models to investigate different slags. Besides the design of the experimental setup and the development of a suitable calculation model, a device as well as procedures for CaO sample production had to be planned. The diffusion coefficients of CaO and MgO in a blast furnace,

calcium aluminate and wollastonite slag at 1500 and 1600 °C, and in a BOF slag at 1400 and 1500 °C were obtained by various dissolution experiments. Additionally, the diffusion coefficients or dissolution rates of Al_2O_3, SiO_2 and $MgAl_2O_4$ were measured in a ladle furnace slag at 1550 °C. The results and the comparison with literature data showed in general a decrease of the diffusion coefficient with increasing slag viscosity. Comparison with literature data also confirmed the suitability of the experimental setup and the calculation model.

A method allowing the determination of activities of individual slag components without the need for literature data was required. Such a procedure could be realized using Knudsen effusion mass spectrometry (KEMS). The KEMS measurements were carried out at Forschungszentrum Jülich. Since this method was rarely used in the metallurgical research field, the experiments, in the course of this work, were able to establish a basis for further research. In addition to the determination of the activity of CaO and MgO in various slags, the KEMS measurements also allowed the calculation of the enthalpies of formation of both oxides. Comparison of the measurements with literature values confirmed the suitability of this method for activity measurements of slag components.

Kurzfassung

Bei der Eisen- und Stahlherstellung sowie bei sekundär metallurgischen Behandlungen spielen Schlacken eine wichtige Rolle. Die Schlackeneigenschaften, wie z.B. Viskosität, Dichte, Liquidustemperatur, Oxidationspotential, Schäumungsverhalten etc., haben einen erheblichen Einfluss auf die Effizienz metallurgischer Prozesse. Diese Eigenschaften werden weitgehend von der Schlackenzusammensetzung bestimmt. Die Schlackenzusammensetzung wird bei allen metallurgischen Prozessen durch die Zugabe von Additiven eingestellt. Dabei handelt es sich meist um CaO- und/oder MgO-haltige Zuschlagstoffe. Um Auflösungsprozesse von Additiven in Schlacken beschreiben und somit bestehende Prozesse optimieren oder neuartige entwickeln zu können, ist das Wissen über Diffusionskoeffizienten des jeweiligen Oxids in Schlacken notwendig. Des Weiteren ist die Kenntnis thermodynamischer Aktivitäten einzelner Schlackenkomponenten von großer Bedeutung, um metallurgische Vorgänge zu verstehen und optimieren zu können. So führt eine niedrige Aktivität der zu extrahierenden Spezies (z.B. P oder S) in der Schlacke zu einer effizienten Entfernung dieser Komponenten aus dem Stahl. Die Aufnahmefähigkeit von Schlacken für unerwünschte Stahlbegleitelemente wird wiederum durch die Zusammensetzung der Schlacke beeinflusst. Die Ermittlung dieser beiden Parameter (Diffusionskoeffizient und Aktivität) in Schlacken war Ziel dieser Arbeit.

Für die Bestimmung von Diffusionskoeffizienten in Schlacken wurde ein experimenteller Aufbau konstruiert, welcher es ermöglicht, Auflösungsversuche unter reproduzierbaren Bedingungen durchzuführen. Zusätzlich zur Konstruktion des Versuchsaufbaus wurde ein Berechnungsmodell aufgesetzt, welches es ermöglicht, aus den Daten der Auflösungsersuche den Diffusionskoeffizienten zu berechnen. In diesem Modell sind ein Dichtemodell und fünf unterschiedliche Viskositätsmodelle enthalten. Da jedes Viskositätsmodell für einen gewissen

Temperatur- und Zusammensetzungsbereich gültig ist, war es notwendig, mehrere Modelle zu verwenden, um unterschiedliche Schlacken zu untersuchen. Neben der Konstruktion des Versuchsaufbaus und der Entwicklung eines geeigneten Berechnungsmodells, musste eine Vorrichtung sowie Vorgehensweise zur CaO-Probenherstellung geplant werden. Mittels diverser Auflösungsversuche wurden die Diffusionskoeffizienten von CaO und MgO in einer Hochofen-, Calcium-Aluminat- und Wollastonitschlacke bei 1500 und 1600 °C sowie in einer LD-Schlacke bei 1400 und 1500 °C bestimmt. Des Weiteren wurden die Diffusionskoeffizienten bzw. Auflösungsraten von Al_2O_3, SiO_2 und $MgAl_2O_4$ in einer Pfannenofenschlacke bei 1550 °C gemessen. Die Ergebnisse und der Vergleich mit Literaturwerten zeigten Im Allgemeinen eine Abnahme des Diffusionskoeffizienten mit zunehmender Schlackenviskosität. Zudem konnte die Eignung des Versuchsaufbaus sowie des Berechnungsmodells durch den Vergleich mit Literaturwerten bestätigt werden.

Es wurde nach einem Verfahren gesucht, welches die Bestimmung von Aktivitäten einzelner Schlackenkomponenten ohne die Notwendigkeit von Literaturdaten ermöglicht. Eine solche Vorgehensweise konnte mittels der Knudsen Effusion Massenspektrometrie (KEMS) realisiert werden. Die KEMS-Untersuchungen wurden im Forschungszentrum Jülich durchgeführt. Da dieses Verfahren auf dem metallurgischen Forschungssektor nur selten eingesetzt wurde, konnte mit den Experimenten, im Zuge dieser Arbeit, ein Grundstein für weitere Forschungen gelegt werden. Die KEMS-Messungen ermöglichten neben den Aktivitätsbestimmungen von CaO und MgO in diversen Schlacken auch die Ermittlung der Bildungsenthalpien beider Oxide. Der Vergleich der Messungen mit Literaturwerten bestätigte die Eignung dieser Methode für Aktivitätsbestimmungen von Schlackenkomponenten.

Table of contents

1 Introduction and Objectives

In addition to new technologies, the sustainable production of metallic products also requires the development of digital systems. These serve to quantify the resource efficiency of circular economy systems. The so-called digital twins are based on fundamental knowledge of metallurgical processes and serve as a basis for the control and optimization of circular systems according to scientific and technical aspects. Using models, simulations, and connections of metallurgical processes, they represent the material and energy consumption as well as the environmental impact of a circular economy system. Linking metallurgical systems allows maximum utilization of primary or secondary resources. These linkages include, among others, the following elements:

- Inline measurements of ore and scrap properties, coupled with modeling, simulation and optimization of metallurgical reactors and systems for processing primary and secondary raw materials
- Theory, technology, simulation and analysis tools for raw material processing and metallurgical operations
- Evaluation of model/simulation results to estimate resource efficiency of the circular system
- Integration of tools and methods to evaluate resource efficiency and develop sustainable solutions

The digital twin of a circular economy system provides real-time information that can be used to assess the sustainability of the system, taking into account the points mentioned above. As already mentioned, resource efficiency can be defined from this, which in turn provides a direction for innovation. In addition to product centric recycling, mineralogy of recyclates, energy and material efficiency, and several others, analysis and simulation tools for raw material treatment and metallurgical process control are a requirement for creating a digital twin of a circular economy system. Embedded in these tools is the thermodynamic and kinetic simulation of metallurgical processes, in addition to the application of artificial intelligence, computer-aided design, computational fluid dynamics, design for recycling, sustainability, and some others. The challenge here is to develop appropriate tools to optimize metallurgical systems. However, in order to develop such tools, the necessary thermodynamic data must be available. The objective of this thesis is the determination of two quantities essential for modeling metallurgical processes: the diffusion coefficient and the activity of CaO and MgO in metallurgical slags. As the literature data are partly based on doubtful experimental methods or mathematical models, new methods were developed in this work or methods not yet used for such measurements were applied. [1]–[4]

2 Metallurgical slags

Slags play a crucial role in metallurgy with respect to the efficiency of smelting and refining processes through controlled slag-metal-gas reactions. The properties of slags that are crucial for the efficiency of metallurgical processes, such as liquidus temperature, viscosity, density, surface tension, diffusivity, reactivity with refractory material, oxidation potential and foaming, are largely determined by the composition of the slags. Slags are by-products of the smelting and refining of metals, mats, and alloys. They are formed by reactions between slag formers introduced into the metallurgical aggregates, the gangue of the ores and/or reducing agents during the melting process. In addition, slag is also formed, or its chemical composition is changed by reactions between the slag formers introduced and impurities dissolved in the molten metal during refining processes. Dissolution processes of non-metallic inclusions, which are absorbed by the slag, and the refractory furnace lining occur, also leading to a change in the slag composition. For example, the reactions between impurities in the molten metal and the slag mentioned here are desulfurization reactions. The equilibrium reactions between the slag components CaO and MgO with the sulfur dissolved in the molten metal with the associated equilibrium constants K can be described as shown in equation 2-1 to 2-4. [5]-[7]

$$(CaO) + [S] \rightleftharpoons (CaS) + [O] \qquad 2\text{-}1$$

$$K = \frac{a_{(CaS)} \cdot a_{[O]}}{a_{(CaO)} \cdot a_{[S]}} \qquad 2\text{-}2$$

$$(MgO) + [S] \rightleftharpoons (MgS) + [O] \qquad 2\text{-}3$$

$$K = \frac{a_{(MgS)} \cdot a_{[O]}}{a_{(MgO)} \cdot a_{[S]}} \qquad 2\text{-}4$$

a_i stands here for the activity of the respective component in the slag () or metal phase []. From the reactions shown, it is evident that knowledge of thermodynamic activities of various slag components is necessary for the understanding of metallurgical reactions as well as the calculation of equilibrium states and, subsequently, for the control and optimization of metallurgical processes. [8]

As already mentioned, dissolution of slag additives as well as inclusions occurs in metallurgical slags. The rapid dissolution of CaO, for example, significantly determines the productivity of some pyrometallurgical processes. Furthermore, effective and efficient dissolution of inclusions in secondary metallurgy is essential in the context of achieving high steel cleanliness. Different modeling approaches for dissolution of oxide particles are shown in the literature. However, what most to all of these modeling approaches have in common is the need to have knowledge of the diffusion coefficient of the dissolving oxide in the particular slag at the appropriate temperature. [9]–[15]

Kinetic as well as thermodynamic modeling is used for the description of dissolution processes, equilibrium calculations, and changes of state associated with material and energy transport. These models are used to increase the efficiency of existing processes but also to develop new ones. A fundamental understanding of the elementary thermodynamic and kinetic relationships of the processes under consideration is essential to achieve this goal. Since digital computing power is no longer a problem nowadays, the reliability of the model results depends primarily on the accuracy of the thermodynamic data used. [9],[16]

Metallurgical slags can be classified in terms of the type of metal or alloy and the process by which they are formed. Basically, the classification can be made into ferrous, ferro-alloy and non-ferrous slags. In this thesis, the focus is on ferrous slags, which are generated during the production as well as the refining of iron and steel products. This type of slag can mainly be described by the system CaO-SiO_2-Al_2O_3-MgO-FeO or subsystems. [5],[17]

The following chapters will provide an overview of the main process routes in iron and steel making and the processes involved in slag formation. Furthermore, general physicochemical fundamentals and the basics on the dissolution of solids in melts, which are necessary for the determination of diffusion coefficients, will be given. In addition, common experimental methods for activity measurement with their advantages and disadvantages will be discussed.

2.1 Iron and steelmaking

Steel is one of mankind's most important technical materials. The wide, sometimes irreplaceable spectrum of applications for this material, e.g., in construction, mining, transport, agriculture and energy, make it a major driving force for industrialization and economic growth. The two main process routes to produce steel are the so-called integrated route, which consists of pig iron production in the blast furnace (BF) and its further processing into crude steel in the basic oxygen furnace (BOF), and the electric arc furnace (EAF) route. On average, 71.5% of the 1884.2 million tons of crude steel produced worldwide in 2022 was produced by the integrated route and 28.2% by the EAF route. To achieve the required quality requirements, the crude steel produced via both routes must be further refined by means of secondary metallurgical processes. These are ladle furnace treatments (LF) or, in some cases, vacuum treatments. [5],[18]–[21]

2.1.1 Ironmaking

The BF is a gas-solid-liquid reactor which is operated in countercurrent. This means that the charged solids as well as the resulting liquid phase move through the BF from top to bottom, while the gas phase rises from bottom to top. During the process, ferrous input materials are transformed into pig iron and slag together with slag formers at high temperatures and in the presence of coke. The complex physicochemical processes involved in this process include, for example, the reduction of oxides, the combustion and gasification of carbon, the formation, melting and separation of slag and metal, reactions between slag and coke (reduction of liquid metal compounds), and the refining of the resulting pig iron by slag-metal-gas reactions. Lump ore, in the form of hematite (Fe_2O_3) or magnetite (Fe_3O_4), sinter and pellets serve as ferrous input material. Furthermore, DRI and ferrous recycled material are also used to a certain extent. The amount of gangue, the reducibility as well as the softening and melting behavior of the iron carriers, affect the productivity of the BF. [5],[19]–[21]

To adjust slag chemistry and the associated liquidus temperature as well as the required slag volume, slag formers are added. These are limestone ($CaCO_3$), dolomite ($CaMg(CO_3)_2$), olivine ($(Mg,Fe)_2SiO_4$) or quartz (SiO_2). Sinter or pellets offer the advantage that they already contain the right amount of slag formers to achieve the desired slag composition and quantity. [5],[19]–[21]

Coke as well as pulverized coal blown in via the tuyeres (PCI) and other auxiliary fuels (natural gas, fuel oil) serve as energy sources for the endothermic reduction reactions and for melting the furnace charge. The carbon carriers also provide the chemical potential needed for the reduction of iron oxides as well as the carbon needed for direct reduction. Preheated, oxygen-enriched air is introduced via the tuyeres. It reacts with the coke and the PCI to produce high temperatures and a CO-H_2-N_2 gas mixture, which is required for indirect reduction and heat transfer in the furnace. Due to the heat transfer of the gas to the coke and burden, they are heated to such an extent that a liquid phase is formed, in other words, melting occurs. Due to the counterflow of gases, liquids and solids in the BF, efficient heat and mass transfer results. [5],[19]–[21]

The products of the blast furnace process include C-saturated pig iron, slag, top gas and flue dust. Pig iron as well as slag are tapped at specific time intervals through tapping holes, of which modern large blast furnaces have up to four. [5],[19]–[21]

The pig iron produced in the BF can either be processed directly in the steel plant into crude steel or undergoes pretreatment in advance. These treatments are used to optimize the overall process (BF+BOF) by removing unwanted impurities such as sulfur, phosphorus, or silicon from the pig iron. Pretreatment of the pig iron reduces the costs of the subsequent steelmaking steps. [5],[19]

The slag formed during iron making in the BF is part of the CaO-SiO_2-Al_2O_3-MgO system. In addition to the main components, small amounts of MnO, FeO, K_2O, Na_2O, TiO_2, S and P are present in the slag. The slag is generated by the reaction of the gangue components of the ore (silicates, aluminosilicates, sulfides) and the ash of coke and PCI with the charged slag formers. Slag formation in the BF is a three-step process. First, the formation of the primary slag takes place, which is mainly composed of FeO and oxides such as CaO, Al_2O_3, MgO, SiO_2 and MnO. Slag formation begins with the melting of FeO. This acts as a flux and dissolves gangue components to form low-melting phases. The reaction of the iron oxide dissolved in the slag with the carbon of the coke leads to the reduction of FeO. More and more CaO and MgO are dissolved in the slag and FeO is completely reduced. The resulting slag is called secondary slag and is high-melting and basic. Dissolution of the ash components of coke and PCI in the secondary slag finally produces the final slag. A typical composition (in wt.-%) of the final slag is in the range of 40% CaO, 36% SiO_2, 10% MgO, 10% Al_2O_3. Physical and chemical properties of the final slag (liquidus temperature, basicity, viscosity, sulfide capacity, slag rate) have a significant influence on the pig iron quality as well as the productivity of the BF. [5],[19]

The basicity of slags results from the ratio of basic and acidic slag components. Because CaO and SiO_2 are commonly the dominant slag components, basicity is often defined as the CaO/SiO_2 ratio (C/S). Here, this form is referred to as binary basicity B_2 and is calculated as shown in equation 2-5. [20]

$$B_2 = \frac{CaO}{SiO_2} \tag{2-5}$$

For the calculation of B_2, the amounts of CaO and SiO_2 in wt.-% are used. When calculating the slag basicity in blast furnace operation, the four-component basicity B_4 is also often calculated. It is defined as follows (equation 2-6). [20]

$$B_4 = \frac{CaO + MgO}{SiO_2 + Al_2O_3} \tag{2-6}$$

To achieve a liquid slag with sufficient sulfide capacity, B_4 of blast furnace slags should be in the range of 1.05 to 1.15. [5],[20]

2.1.2 Steelmaking

The term steelmaking refers to a sequence of chemical reactions and refining steps that happen either sequentially or simultaneously. The aim is to convert pig iron or crude steel composition into a specific steel composition. Steelmaking can be divided into two main categories. Primary metallurgy and secondary metallurgy. Primary steelmaking involves refining pig iron in a BOF or melting scrap steel, DRI and other metallic additives in an EAF to produce crude steel. Secondary steelmaking, on the other hand, involves further refining of the crude steel by, for example, further removal of impurities, degassing and additional alloying and temperature adjustment before continuous casting. [5],[20]

2.1.2.1 Basic oxygen steelmaking

In oxygen steelmaking, the base input material is pig iron from the BF, in which the iron constituents are reduced to a specified content using technically pure oxygen (>99% O_2). Depending on the type of oxygen input, the process can be divided into oxygen top-blowing and oxygen bottom-blowing processes. The so-called LD process is the most important process. Here, the oxygen is blown vertically from above through a water-cooled lance onto the metal bath. The term basic oxygen furnace (BOF) is also widely used for the LD converter. The BOF is a tiltable crucible lined with magnesia bricks as refractory material. The exothermic reaction between the injected O_2 and the associated elements contained in the molten metal, such as C, Si, Mn, and P, causes an increase of the temperature of the molten metal from the pig iron input temperature (1250-1400 °C) to the steel temperature (≥1600 °C). Scrap or even iron ore is fed into the converter for temperature control, which makes 20-30% of the total metal quantity, while the fed pig iron has a quantity of 70-80%. In addition to scrap, slag formers and fluxes are introduced into the process, which are mainly limestone, dolomite, and fluorspar

(CaF_2). The slag in the BOF removes phosphorus and sulfur dissolved in the molten metal. [5],[19]–[21]

The BOF process is a discontinuous process involving several subsequent steps. First, scrap, pig iron, fine iron ore and other ferrous input materials are charged into the tilted converter. Then, the crucible is placed vertically again and basic slag forming additives are added. The water-cooled oxygen lance is then introduced and the injection of oxygen for the oxidation of dissolved impurities begins. The oxygen exits the nozzle mouth at supersonic velocity. Slag formation in the BOF starts with the oxidation of Si, Mn, P dissolved in the pig iron and of the iron itself, forming a thin and acidic slag. The CaO and/or MgO introduced as additives dissolve in this slag. The reaction of the injected oxygen with the carbon in the pig iron leads to the formation of CO. This in turn leads to an intensive bath movement and foaming of the slag. The dissolution of all the added slag formers as well as other oxidation products (such as SiO_2, P_2O_5, MnO, FeO) and the wear of the refractory lining finally leads to the adjustment of the chemical composition of the final BOF slag. Due to the strong oxidizing conditions in the converter, the final slag has a high basicity (B_2>3) and the FeO content might be up to 35-38 wt.%. The consumption of fluxes and the final volume of the BOF slag depends on the amount of dissolved silicon, manganese, and phosphorus in the input materials. To determine the required amount of oxygen, the bath temperature is measured after approximately 15 minutes of blowing time and a chemical analysis of the melt is performed. The total blowing time is about 17 minutes. After reaching the required composition and temperature, the steel is tapped through the tap hole by tilting the converter. To tap the slag, the crucible is flipped to the other side. During tapping, alloying elements can be added to the crude steel to prepare it for possible further secondary metallurgical treatment. [5],[19]

Depending on the initial composition and temperatures, as well as the required chemical composition and temperatures of the tapped steel, the quantities of pig iron, scrap, oxygen and slag formers vary. [5],[20],[21]

2.1.2.2 Electric arc furnace steelmaking

To produce crude steel, solid steel scrap, DRI/HBI, ore, slag formers and other additives are melted in the electric arc furnace (EAF) by using electrical energy. This is done by passing electric current through three graphite electrodes and igniting an arc between the input material and the electrode. The heat generated by the arc melts the feedstock. Additional chemical energy is also generated in the melting phase by injecting oxygen, or a fuel-gas mixture supplied by specially designed burners and lances. Similar to the BOF, basic slag formers such as burnt lime and dolomitic lime are used in the refining stage to form basic slags (C/S>1.5). [5],[20]–[22]

As in the LD process, crude steel production with an EAF is also a discontinuous batch process. The furnace is charged with the input materials using so-called scrap baskets. For this purpose, the lid together with the electrodes is lifted and rotated to the side. After charging, the lid and the electrodes are rotated back over the furnace. The lid and electrodes are then lowered. Then, an arc is ignited between the scrap and the electrode, causing current to flow through the electrodes and the material itself. The arc and the electrical resistance of the metal create the heat that melts the scrap. Once a melt pool is formed, the arc stabilizes and the mean power input increases. Calcium oxide in the form of burnt lime or dolomite is added to the furnace together with the scrap or is blown into the furnace during the melting process. After the first batch is melted down, another one can be placed. Typically, 2 to 3 baskets are charged. After the melting process, metallurgical refining operations (such as decarburization and dephosphorization) are executed. Therefore, oxygen is injected into the molten steel via a lance. Iron constituents such as aluminum, silicon, manganese, phosphorus and carbon, and some iron itself, are oxidized during the oxygen supply. The oxidation products, together with the introduced CaO, form the slag. During refining of the steel, carbon powder is also injected into the slag floating on the steel bath. This leads to the formation of CO, which on the one hand causes intensive bath agitation and thus promotes mass transfer between metal and slag, and on the other hand causes the slag foaming. As soon as the required chemical composition of the steel is reached, the EAF is tilted, and the slag is tapped. The steel is tapped by tilting the EAF in the opposite direction. In the classic process sequence, the "black" oxide-rich slag must be removed after the oxidation phase and a "white" refining slag added to achieve reducing conditions. This is a time-consuming and cost-intensive process, so the classic method has lost importance for large production plants. Nowadays, the EAF serves mainly as a melting unit where only the dephosphorization and oxidation phases take place. [20],[22]

2.1.2.3 Secondary steelmaking

After the liquid steel has been tapped from BOF or EAF, it can undergo further refining processes to remove remaining impurities or to achieve the required chemical composition and quality of the product by the addition of alloying elements. This refining process is referred to as secondary or ladle metallurgy because it takes place in the transport ladle. Secondary metallurgy is common in the production of high-quality steels. Major tasks of secondary metallurgy are desulfurization, deoxidation, degassing (removal of nitrogen and hydrogen), separation of reaction products in the slag, inclusion modification, and final decarburization (for ultra-low carbon steels). Depending on the quality required, most of the steels produced in the BOF and EAF undergo any or all of the above-mentioned refining processes. Injecting desulfurization agents (such as Ca, Mg, CaSi, CaC_2) through a lance can reduce the sulfur content of the steel to 0.0002%. The addition of silicon and aluminum leads to the formation of SiO_2 and Al_2O_3 during deoxidation. These oxides are incorporated by the slag added during the refining process. To precisely adjust the chemical composition of the steel to produce different steel grades, the required alloying elements are also added to the molten steel via an alloy hopper connected to the ladle furnace. The ladle slag is formed by adding synthetic slag formers, entrainment slag from the furnace, deoxidation or desulfurization products. [5],[20]-[23]

2.1.2.4 Steelmaking slags

Steel making slags are crucial for the removal of impurities and non-metallic inclusions from the steel. They also act as protection against reoxidation by atmospheric oxygen and the absorption of atmospheric nitrogen and hydrogen, as well as providing thermal insulation and reducing heat losses. In addition, these slags fulfill other important tasks in some processes. For example, slag foaming is an important practice in modern EAFs because an optimally foaming slag seals the heat from the electric arc, minimizing heat losses and protecting the refractory and water-cooled plates of the furnace from thermal radiation. Thus, energy efficiency can be increased, and higher energy input and productivity can be achieved. The physicochemical properties of steel making slags are mainly influenced by the chemical (e.g. basicity and oxidation potentials) and physical properties (e.g. density, liquidus temperature and viscosity). [5],[22]

2.2 General physicochemical fundamentals

Iron and steelmaking involve multiple chemical reactions and other physicochemical processes (viscous flow, interfacial phenomena, mass transfer, etc.) at high temperatures. An understanding of the metallurgical processes involved in iron and steel production is therefore based on physical chemistry, which is one of the most important scientific tools. In addition to the fundamentals of physical chemistry, chemical thermodynamics, which consists of reaction free energies and enthalpies as well as chemical equilibria, has the broadest usage. It was only possible to apply the laws of thermodynamics to iron and steel production after experimental measurements had been carried out to obtain the necessary data, such as free energies and enthalpies of reaction, relationships between activity and composition, etc. [21]

2.2.1 Thermodynamic equilibrium

The thermodynamic equilibrium is the final stable state of a system in interaction with its environment. It includes the following conditions [21]:

a. Mechanical equilibrium, which means uniform pressure in the entire system when no other forces are present.
b. Thermal equilibrium, which means uniform temperature in the entire system.
c. Chemical equilibrium, i.e., uniform chemical potentials of all components in the entire system.

2.2.2 Activity, free energy and equilibrium

These quantities are to be used for thermodynamic calculations of isothermal reactions and processes (initial and end temperatures are equal).

2.2.2.1 Activity

Per definition, the activity of a substance can be described as shown in formula 2-7.

$$a_i = \frac{f_i}{f_i^\circ} \tag{2-7}$$

Here, a_i represents the activity of component i (element or compound) in a solution at a temperature T, f_i represents the fugacity of component i in a solution at a temperature T, and f_i° is the fugacity of component i in its standard state (i.e., pure element or compound i at T and at standard pressure (usually 1 atm or 1 bar)). [21]

Therefore, the activity corresponds per definition in the standard state (equation 2-8):

$$a_i = \frac{f_i^\circ}{f_i^\circ} = 1 \tag{2-8}$$

In an ideal gas, f_i equals p_i and f_i° equals p_i°. This results in the definition of the activity, which is shown in equation 2-9.

$$a_i = \frac{p_i}{p_i^\circ} \tag{2-9}$$

p_i stands for the partial pressure of component i in an ideal gas mixture and p_i° represents the partial pressure of component i in its standard state (i.e., pure element or compound i at T).

2.2.2.2 Activity and free energy

Equation 2-10 shows a basic relationship between the free energy and the activity at constant temperature. [21]

$$\bar{G}_i^m = \bar{G}_i - G_i^\circ = R \cdot T \cdot \ln a_i \qquad \text{2-10}$$

$\bar{G}_i^m$ is the partial molar free energy of mixing of component i in solution, $\bar{G}_i$ is the partial molar free energy of component i in solution, G_i° is the molar free energy of component i in its standard state, T is the temperature in Kelvin, and R is the universal gas constant (8.314 J/mol·K).

The average of a property (including the free energy) per mole of the solution is called an integral molar property. Therefore, G (integral molar free energy of the solution at temperature T) is equal to (formula 2-11): [21]

$$G = \sum_{i=1}^{k} X_i \cdot \bar{G}_i \qquad \text{2-11}$$

In a solution with k components, the molar fraction X_i is calculated as shown in formula 2-12.

$$X_i = \frac{n_i}{n_1 + n_2 + \cdots + n_i + \cdots + n_k} = \frac{n_i}{\sum_{i=1}^{k} n_i} \qquad \text{2-12}$$

n_i represents the number of moles of component i. Thus, the relationship shown in equation 2-13 is valid for the integral molar free energy of mixing of the solution. [21]

$$\Delta G^m = \sum_{i=1}^{k} X_i \cdot \bar{G}_i = R \cdot T \cdot \sum_{i=1}^{k} X_i \cdot \ln a_i \qquad \text{2-13}$$

2.2.2.3 Free energy and equilibrium

In equilibrium at constant temperature and pressure, the approach $(\Delta G)_{T,P} = 0$ is valid. [21]

Based on the isothermal chemical reaction shown in equation 2-14

$$aA + bB = lL + mM \qquad \text{2-14}$$

a, b, l and m represent the number of moles of components A, B, L and M. The change in Gibbs energy corresponds ΔG to (formula 2-15):

$$\Delta G = \Delta G^{\circ} + R \cdot T \cdot \ln K \qquad \text{2-15}$$

ΔG° corresponds to the value of ΔG if the reactants and products are in the respective standard state. K stands for the activity quotient under equilibrium conditions and is also called the equilibrium constant. It can be calculated as shown in equation 2-16.

$$K = \frac{a_L^l \cdot a_M^m}{a_A^a \cdot a_B^b} \qquad \text{2-16}$$

a_I in this case represents the activity of the corresponding component. If the reaction shown in equation 2-14 also takes place at constant pressure, then $(\Delta G)_{T,P} = 0$ is valid at equilibrium. Therefore, the following relationship holds for this reaction under equilibrium conditions (formula 2-17):

$$\Delta G^{\circ} = -R \cdot T \cdot \ln K \qquad \text{2-17}$$

2.3 Fundamentals of the dissolution of solids in melts

Dissolution of solids in melts is assumed to be a diffusion-controlled mechanism. The pure diffusive mass flux j is described by Fick`s first law. This is shown in equation 2-18. [6],[24]

$$j = D_{eff} \cdot \frac{(c_1^l - c_0^l)}{\delta} = D_{eff} \cdot \frac{(c_s^l - c_0^l)}{\delta} \qquad \text{2-18}$$

D_{eff} stands for the effective binary diffusion coefficient of the dissolving substance, c_1^l and c_0^l are the concentrations of the dissolving species at the solid-melt interface and the bulk concentration of the melt of the respective substance, respectively. Because the difference between c_1^l and the saturation concentration of the melt for the considered species c_s^l is very small in most cases, it can be used to simplify the calculation. c_s^l is usually known or can be easily calculated using thermodynamic programs. δ is the effective diffusive boundary layer thickness.

By introducing the mass transfer coefficient β, this equation can be simplified. β is the ratio of the effective diffusion coefficient and the boundary layer thickness. The simplified formula can be seen in equation 2-19.

$$j = \beta \cdot \left(c_s^l - c_0^l\right) \tag{2-19}$$

In addition to diffusivity, the mass transfer also depends on the fluid flow, the kinematic viscosity of the melt and the geometry of the arrangement. All these parameters influence the effective boundary layer thickness. These dependencies or relationships are usually represented by dimensionless ratios, such as the Sherwood number Sh, the Reynolds number Re, and the Schmidt number Sc. The relationships for these ratios can be taken from formulas 2-20 to 2-22. [6]

$$Sh = \frac{\beta \cdot L}{D_{eff}} \tag{2-20}$$

$$Re = \frac{u \cdot L}{\nu} \tag{2-21}$$

$$Sc = \frac{\nu}{D_{eff}} \tag{2-22}$$

L stands for a characteristic length and u for a characteristic flow velocity, which are chosen depending on the present system. ν is the kinematic viscosity of the melt, which is the ratio of the dynamic viscosity η and the density of the melt ρ.

Depending on the present system, further simplexes or complexes Γ_i can be included, which contain geometric parameters. Using a power law (equation 2-23), these dimensionless numbers can be related to each other. [6]

$$Sh = const.\cdot Re^a \cdot Sc^b \cdot \prod_i \Gamma_i^{c_i} \tag{2-23}$$

It is possible to determine the constant as well as the exponents in equation 2-23 by fitting the results of several simulations. By representing β using this equation, the power law for it is obtained. This can be seen in formula 2-24. [6]

$$\beta = const.\cdot D_{eff}^{1-b} \cdot \nu^{b-a} \cdot u^a \cdot L^{a-1} \cdot \prod_i \Gamma_i^{c_i} \tag{2-24}$$

Substituting this equation into the relationship for mass flow yields the relationship in equation 2-25.

$$j = \underbrace{D_{eff}}_{D_{eff}} \cdot \underbrace{D_{eff}^{-b} \cdot const.\cdot \nu^{b-a} \cdot u^a \cdot L^{a-1} \cdot \prod_i \Gamma_i^{c_i}}_{1/\delta} \cdot \underbrace{\left(c_s^l - c_0^l\right)}_{\Delta c} \tag{2-25}$$

This equation represents the dependence of the mass flow on various parameters. The combination of solid and melt influences the concentration difference Δc as well as the effective diffusion coefficient. The fluid flow and geometrical parameters affect the mass flow by their influence on δ and $1/\delta$, respectively.

Two different methods of investigation are commonly used to evaluate dissolution processes of solids in melts or slags. The first method is high temperature laser scanning confocal microscopy (HT-LSCM). It allows in-situ observation of the dissolution of particles in melts. Due to possible temperature gradients within the crucible, investigations of this type can result in uncontrolled and unmeasurable relative motion between the dissolving particle and the melt. This causes the effective boundary layer thickness to be undefined. Furthermore, this technique is limited to transparent or at least translucent slags. The second commonly used method to investigate dissolution behavior is the rotating cylinder or disc method. In this method, rotationally symmetrical specimens are immersed in melts at high temperatures and rotated using a rotating device. Usually, the specimens are removed from the melt after a certain time and the material loss is determined. Compared to HT-LSCM, this type of investigation offers the advantages that there is no need for transparent slags and that the effective boundary layer thickness for rotating cylinders in liquids can be well defined and adjusted or described by the rotation speed of the test specimens. Furthermore, experimental conditions, including slag dynamics, are exactly reproducible. [25],[26]

The dissolution is basically controlled by diffusion processes in the liquid phase, therefore diffusivity is the most important parameter for the determination of the dissolution behavior. Equations for mass transfer can be used to determine diffusivity from experiments with rotating cylinders or disks. The mass transfer coefficient is often calculated using Sherwood relationships. In the following, those relations are considered in more detail which are relevant for this work. [6],[27],[28]

Based on the Cochran equation from [29], Levich in [30] established equation 2-26 for the mass transfer of a disk-shaped surface with infinite radius immersed in a semi-infinite medium. This equation provides a precise approximation to the mass flux density for real finite geometries, provided that the thickness of the velocity boundary layer is much smaller than the disk radius. The mass flux density is also constant over the entire disk surface, allowing this equation to be used to estimate the change in length of a cylindrical sample. This was noted by Cooper and Kingery in [31]. [6],[28]

$$Sh_{0,Lev} = 0.62 \cdot Re^{1/2} \cdot Sc^{1/3} \tag{2-26}$$

Here, the characteristic velocity u for calculating the Reynolds number is the circumferential velocity of the disk and the characteristic length L is the radius of the disk. Re is then calculated as shown in equation 2-27.

$$Re = \frac{u \cdot L}{\nu} = \frac{\omega \cdot L^2}{\nu} \tag{2-27}$$

The circumferential velocity is the product of angular velocity ω and disk radius.

For the description of the mass flow density, an analogy between heat and mass transport is used in many cases. For this purpose, Nusselt equations are transformed into Sherwood relations. For example, in [32], Tachibana and Fukui established empirical equations for heat transfer in an annular gap between a rotating inner cylinder and a stationary outer cylinder. With exception of the axial gap between the lower end of the dissolving cylinder specimen and the crucible this experimental setup is similar to that of the rotating cylinder method, so the Nusselt relations defined for it may be suitable for conversion to Sherwood equations and description of mass transfer. Equation 2-28 represents this Sherwood relationship. The characteristic length here is the radial gap between the inner and outer cylinders. When converting Nusselt relationship to Sherwood relationship and using it to calculate mass flow density, variable boundary conditions due to the relative motion of the interface between the solid and the melt, due to the dissolution of the solid, as well as the influence of the Stefan flow on the flow field should be considered. These parameters are missing in the consideration of the heat transfer. [6]

$$Sh_{0,Tach} = 0.21 \cdot \left(Ta_{Tach}^2 \cdot Sc\right)^{1/4} = \frac{\beta \cdot (R_2 - R_1)}{D_{eff}} \tag{2-28}$$

This relationship is valid up to a Taylor number $Ta_{Tach} \leq 10^4$. R_2 is the inner radius of the crucible in which the specimen is rotated, and R_1 is the average radius of the cylindrical specimen. Ta_{Tach} can be calculated as shown in formula 2-29.

$$Ta_{Tach} = \frac{u \cdot (R_2 - R_1)^{3/2}}{\nu \cdot R_1^{1/2}} = \frac{\omega \cdot R_1^{1/2} \cdot (R_2 - R_1)^{3/2}}{\nu} \tag{2-29}$$

The dimensionless Taylor number indicates the ratio of the centrifugal forces to the viscous forces and describes the tendency to form so-called Taylor vortices. These Taylor vortices represent instabilities in the flow between two concentrically arranged rotating cylinders, which occur as soon as the rotational speed of the inner cylinder reaches a critical value.

2.4 Calculation of the diffusion coefficient

In the following, the exact procedure for calculating the diffusion coefficient of an oxide in a slag is explained.

To consider the convective part of the mass flow, which occurs perpendicular to the solid-melt interface due to the Stefan flow, and the influence of the Stefan flow on the boundary layer thickness, the equation for pure diffusive mass flow must be extended. These extensions result in equation 2-30. [6],[27]

$$j = \chi_D \cdot \frac{D_{eff}}{L} \cdot \frac{1}{1 - w_s} \cdot Sh_0 \cdot \Delta c \tag{2-30}$$

Here j stands for the mass flow density and w_s is the saturation concentration in mass percent. Sh_0 corresponds to the Sherwood number without considering the effect of the convective component of the mass flow on the boundary layer thickness and χ_D is a correction factor for it. The quantity χ_D is defined by the ratio of the true Sherwood number Sh also including the impact of the convective flow increasing the effective diffusive boundary layer thickness and Sh_0. Using the concept of effective binary diffusivity, as well as assuming a constant slag density ρ_s, Δc can be replaced by $\rho_s * (w_s - w_0)$, where w_0 is the concentration for the dissolving oxide in the slag bulk. This is shown in equation 2-31. In the concept of effective binary diffusivity, the diffusing species is considered as one species and all other species in the melt are combined into a second species. Thus, only a single diffusion coefficient exists. With this approach, acceptable results are usually obtainable, as long as there is one main diffusing species which dilutes all others, as is the case in almost all dissolution processes. [33]

$$j = \chi_D \cdot \frac{D_{eff}}{L} \cdot \frac{1}{1 - w_s} \cdot Sh_0 \cdot \rho_s \cdot (w_s - w_0) \tag{2-31}$$

By inserting the mass transfer parameter B, described by equation 2-32, it is possible to simplify equation 2-31 resulting in equation 2-33.

$$B = \frac{w_s - w_0}{1 - w_s} \tag{2-32}$$

$$j = \chi_D \cdot \frac{D_{eff}}{L} \cdot Sh_0 \cdot \rho_s \cdot B \tag{2-33}$$

Merk expressed in [34] χ_D as a function of B. This relation and the necessary parameters can be seen in formulas 2-34 to 2-36.

$$\chi_D = \frac{Sh}{Sh_0} = 1 - \left[0.566 \cdot (1-\sigma_2) + 0.246 \cdot Sc^{-2/3}(1-\sigma_1)\right] \cdot B + O(B^2) \tag{2-34}$$

$$\sigma_1 = \frac{1}{45} \cdot Sc^{-1} - \frac{2}{675} \cdot Sc^{-2} + \frac{1168}{3007125} \cdot Sc^{-3} + O(Sc^{-4}) \tag{2-35}$$

$$\sigma_2 = 0.15555 \cdot Sc^{-1} - 0.00818 \cdot Sc^{-2} - 0.00032 \cdot Sc^{-3} + O(Sc^{-4}) \tag{2-36}$$

The approximation given in equation 2-37 is valid for high Schmidt numbers and is therefore usually sufficient for slags. [34]

$$\chi_D = \frac{1}{1 + [0.566 \cdot (1-\sigma_2) + 0.246 \cdot Sc^{-2/3} \cdot (1-\sigma_1)] \cdot B} \approx \frac{1}{1 + 0.566 \cdot B} \tag{2-37}$$

The total average mass flow can be described by equations 2-38 to 2-41.

$$\bar{j}_{tot} \cdot A_{tot} = \bar{j}_m \cdot A_m + \bar{j}_b \cdot A_b \tag{2-38}$$

$$A_m = 2 \cdot R_1 \cdot \pi \cdot l \tag{2-39}$$

$$A_b = R_1^2 \cdot \pi \tag{2-40}$$

$$A_{tot} = A_m + A_b \tag{2-41}$$

$\bar{j}_{tot}$, $\bar{j}_m$, $\bar{j}_b$ and A_{tot}, A_m, A_b, are the average mass flow densities and surface areas, of the total surface and the mantle or bottom surface of the cylindrical specimen, respectively. l and R_1, respectively, correspond to the immersion length of the specimen covered by the slag and the specimen radius, respectively. By combining the equations for the total mass flow, the Sherwood relations for the cylinder mantle as well as bottom and considering the convective part of the mass flow and the effect of the Stefan flow on the flow field, equations 2-42 and 2-43 result.

$$\bar{j}_{tot} \cdot A_{tot} = \chi_D \cdot D_{eff} \cdot \left(A_m \cdot \frac{Sh_{0,Tach}}{R_2 - R_1} + A_b \cdot \frac{Sh_{0,Lev}}{R_1}\right) \cdot \rho_s \cdot B \tag{2-42}$$

$$\bar{j}_{tot} = \frac{\chi_D}{2l + R_1} \cdot D_{eff}\left(2l \cdot \frac{Sh_{0,Tach}}{R_2 - R_1} + Sh_{0,Lev}\right) \cdot \rho_s \cdot B \tag{2-43}$$

By inserting the formulas for $Sh_{0,Tach}$, $Sh_{0,Lev}$, χ_D, Ta_{Tach}, Sc, and Re and rearranging the equation, the following relationship is obtained (equation 2-44).

$$0.42 \cdot l \cdot \left(\frac{R_1}{\nu \cdot (R_2 - R_1)}\right)^{\frac{1}{4}} \cdot D_{eff}^{\frac{3}{4}} + 0.62 \cdot \frac{R_1}{\nu^{\frac{1}{6}}} \cdot D_{eff}^{\frac{2}{3}} - \bar{j}_{tot} \cdot \frac{2 \cdot l + R_1}{\omega^{\frac{1}{2}}} \cdot \frac{1 + 0.566 \cdot B}{\rho_s \cdot B} = 0 \tag{2-44}$$

This form allows the calculation of the diffusion coefficient as the root of the left-hand side polynomial of equation 2-44. To determine the two unknown quantities (ν and ρ_s) necessary for this purpose, the density model according to Xin as well as the viscosity models by Watt-Fereday, BBHLW (Browning, Bryant, Hurst, Lucas, Wall), Iida, Kalmanovitch-Frank and the NPL model are used.

2.4.1 Density model

In the density model according to Xin et al. from [35], slag density can be described with formula 2-45.

$$\rho_S = \frac{\sum X_i \cdot M_i}{V_m} \tag{2-45}$$

ρ_s is the slag density, X_i the molar fraction of component i, M_i the molar mass of component i and V_m the molar volume of the slag. The molar volume of the slag is calculated according to the molar volume of the pure components and the molar excess volume of the slag (equation 2-46).

$$V_m = \sum X_i \cdot V_i(T) + V^{EX} \tag{2-46}$$

$V_i(T)$ represents the temperature-dependent partial molar volume of component i and V^{EX} the temperature-independent molar excess volume of the slag. In the modeling of $V_i(T)$, the temperature dependence is considered, while in that of V^{EX}, the slag composition is included by considering the binary interactions of the individual components. The two quantities are calculated as shown in equations 2-47 and 2-48.

$$\begin{aligned} V_i(T) &= V_{i,R} + \frac{\partial V_i}{\partial T} \cdot (T - T_R) \\ &= V_{SiO_2} + \frac{\partial V_{SiO_2}}{\partial T} \cdot (T - T_R) + V_{Al_2O_3} + \frac{\partial V_{Al_2O_3}}{\partial T} \cdot (T - T_R) + V_{CaO} \\ &+ \frac{\partial V_{CaO}}{\partial T} \cdot (T - T_R) + V_{MgO} + \frac{\partial V_{MgO}}{\partial T} \cdot (T - T_R) + V_{FeO} + \frac{\partial V_{FeO}}{\partial T} \\ &\cdot (T - T_R) + V_{Fe_2O_3} + \frac{\partial V_{Fe_2O_3}}{\partial T} \cdot (T - T_R) \end{aligned} \tag{2-47}$$

$$
\begin{aligned}
V^{EX} = \sum_{i<j} a_{ij} \cdot X_i \cdot X_j \\
= a_{12} \cdot X_{SiO_2} \cdot X_{Al_2O_3} + a_{13} \cdot X_{SiO_2} \cdot X_{CaO} + a_{14} \cdot X_{SiO_2} \cdot X_{MgO} + a_{15} \\
\cdot X_{SiO_2} \cdot X_{FeO} + a_{16} \cdot X_{SiO_2} \cdot X_{Fe_2O_3} + a_{23} \cdot X_{Al_2O_3} \cdot X_{CaO} + a_{24} \cdot X_{Al_2O_3} \\
\cdot X_{MgO} + a_{25} \cdot X_{Al_2O_3} \cdot X_{FeO} + a_{26} \cdot X_{Al_2O_3} \cdot X_{Fe_2O_3} + a_{34} \cdot X_{CaO} \cdot X_{MgO} \\
+ a_{35} \cdot X_{CaO} \cdot X_{FeO} + a_{36} \cdot X_{CaO} \cdot X_{Fe_2O_3} + a_{45} \cdot X_{MgO} \cdot X_{FeO} + a_{46} \\
\cdot X_{MgO} \cdot X_{Fe_2O_3} + a_{56} \cdot X_{FeO} \cdot X_{Fe_2O_3}
\end{aligned}
\tag{2-48}
$$

$V_{i,R}$ is the partial molar volume of component i at the reference temperature T_R, $\frac{\partial V_i}{\partial T}$ is the thermal expansion coefficient of component i, a_{ij} is the interaction factor between component i and j. Table 2-I and Table 2-II show the optimized parameters given by Xin et al. in [35].

Table 2-I: Optimized values for $V_{i,R}$ and $\frac{\partial V_i}{\partial T}$ [35]

Component	**$V_{i,R}$ (1773 K)** [cm^3/mol]	**$\frac{\partial V_i}{\partial T}$** [cm^3/mol·K]
SiO_2	26.312	$0.740 \cdot 10^{-3}$
Al_2O_3	27.700	$10.108 \cdot 10^{-3}$
CaO	18.031	$1.014 \cdot 10^{-3}$
MgO	12.076	$0.683 \cdot 10^{-3}$
FeO	16.274	$2.615 \cdot 10^{-3}$
Fe_2O_3	39.325	$2.599 \cdot 10^{-3}$

Table 2-II: Optimized values for a_{ij} [35]

Parameter	a_{ij} [cm^3/mol]	System
a_{12}	5.64	SiO_2-Al_2O_3
a_{13}	0.80	SiO_2-CaO
a_{14}	2.00	SiO_2-MgO
a_{15}	-5.21	SiO_2-FeO
a_{16}	-7.44	SiO_2-Fe_2O_3
a_{23}	18.45	Al_2O_3-CaO
a_{24}	6.53	Al_2O_3-MgO
a_{25}	-10.97	Al_2O_3-FeO
a_{26}	72.80	Al_2O_3-Fe_2O_3
a_{34}	-2.30	CaO-MgO
a_{35}	3.77	CaO-FeO
a_{36}	1.51	CaO-Fe_2O_3
a_{45}	-10.05	MgO-FeO
a_{46}	21.13	MgO-Fe_2O_3

In [35], no interaction parameter for the FeO-Fe_2O_3 system was given. However, methods for calculating the FeO or Fe_2O_3 content for slags containing iron oxide are given in their work.

2.4.2 Viscosity models

In this chapter, the viscosity models applied in the calculation model for the diffusion coefficients are described in detail. Different models for the viscosity calculation were considered to describe the viscosities of the different slags at the different experimental temperatures with the highest possible accuracy.

2.4.2.1 Watt-Fereday

The calculation of the viscosity with the Watt-Fereday model, described in the work of Vargas et al [36], is performed by equation 2-49.

$$\log\eta = \frac{m \cdot 10^7}{(T-423)^2} + c \qquad 2\text{-}49$$

η represents the viscosity in Pa·s and T the temperature in Kelvin. The two parameters m and c can be calculated as shown in equations 2-50 and 2-51.

$$m = 0.00835 \cdot w_{SiO_2} + 0.00601 \cdot w_{Al_2O_3} - 0.109 \qquad 2\text{-}50$$

$$c = 0.0415 \cdot w_{SiO_2} + 0.0192 \cdot w_{Al_2O_3} + 0.0276 \cdot w_{Fe_2O_3,Equiv.} + 0.016 \cdot w_{CaO} - 4.92 \qquad 2\text{-}51$$

w_i is the concentration of component i in weight percent. For the Fe_2O_3 content, the Fe_2O_3 equivalent $w_{Fe_2O_3,Equiv.}$ is calculated using equation 2-52.

$$w_{Fe_2O_3,Equiv.} = w_{Fe_2O_3} + 1.11 \cdot w_{FeO} + 1.43 \cdot w_{Fe} \qquad 2\text{-}52$$

For the Watt-Fereday Model, according to Vargas et al. in [36], the slag composition must be converted as shown below (equation 2-53).

$$w_{SiO_2} + w_{Fe_2O_3,Equiv.} + w_{CaO} + w_{MgO} = 100\% \qquad 2\text{-}53$$

2.4.2.2 BBHLW

Pummill describes in [37] that Browning, Bryant, Hurst, Lucas and Wall (BBHLW) made the assumption in their viscosity modeling that for a given slag viscosity, the slope of the viscosity-temperature curve is the same as that of all other curves with the same viscosity. Using this assumption, they were able to normalize all slag viscosity curves and fit a standard curve. Viscosity is calculated in the BBHLW model as shown in equation 2-54.

$$\log\left(\frac{\eta}{T-T_S}\right) = \frac{14788}{T-T_S} - 10.931 \qquad 2\text{-}54$$

η is again the viscosity in Pa·s, T the temperature in K and T_S the temperature shift which is needed for the normalization of the viscosity curves. T_S is described by formula 2-55.

$$T_S = 306.3 \cdot \ln(A) - 574.31 \qquad 2\text{-}55$$

The dependence of T_S is described by the term A, which is calculated as shown in equation 2-56. Only those species are shown here which are necessary for this work.

$$A = \frac{3.19 \cdot X_{Si} + 0.855 \cdot X_{Al}}{0.93 \cdot X_{Ca} + 1.50 \cdot X_{Fe} + 1.21 \cdot X_{Mg}} \qquad 2\text{-}56$$

X_i is again the molar fraction of component i.

2.4.2.3 Iida

The viscosity model according to Iida in [38] is based on the Arrhenius-type equation. In this model, the network structure of the slag is considered using the so-called modified basicity index B_i^*. The viscosity calculation is done using equation 2-57.

$$\eta = A \cdot \eta_0 \cdot e^{(E/B_i^*)} \qquad 2\text{-}57$$

η is the viscosity in Pa·s and η_0 the hypothetical viscosity of the slag. The two parameters A and E are calculated as shown in equation 2-58 and 2-59.

$$A = 1.029 - 2.078 \cdot 10^{-3} \cdot T + 1.050 \cdot 10^{-6} \cdot T^2 \qquad 2\text{-}58$$

$$E = 28.46 - 2.884 \cdot 10^{-2} \cdot T + 4.000 \cdot 10^{-6} \cdot T^2 \qquad 2\text{-}59$$

T is the temperature in K. η_0 is calculated from the hypothetical viscosities of the individual components η_{0i} and the molar fractions X_i (equation 2-60).

$$\eta_0 = \sum \eta_{0i} \cdot X_i \qquad 2\text{-}60$$

Forsbacka et al. in [39] gave relationships between η_{0i} and T. These are given in Table 2-III. B_i^* is described by equation 2-61. Only the species necessary for this work are considered in the equation.

$$B_i^* = \frac{\sum(\alpha_i \cdot w_i)_B}{\sum(\alpha_i \cdot w_i)_A + \alpha_{Al_2O_3}^* \cdot w_{Al_2O_3}} \qquad 2\text{-}61$$

α_i is a specific coefficient for each slag component i, the values necessary for this work are given in Table 2-III, and w_i represents the content of component i in mass percent. α_i^* is a modified specific coefficient describing the interaction between the amphoteric oxides with the other slag components.

Table 2-III: Values for α_i and functions for η_{0i} [39]

Oxid	α_i	η_{0i} [Pa·s]
SiO_2	1.48	$1.3170 \cdot 10^{-4} \cdot e^{5613.5/T}$
Al_2O_3	0.10	$1.4792 \cdot 10^{-4} \cdot e^{6679.5/T}$
CaO	1.53	$1.3651 \cdot 10^{-4} \cdot e^{8664.4/T}$
MgO	1.51	$1.4743 \cdot 10^{-4} \cdot e^{9393.1/T}$
FeO	0.96	$2.1163 \cdot 10^{-4} \cdot e^{4427.7/T}$

The indices B and A stand here for basic and acidic oxides. The classification into basic, acidic and amphoteric oxides is defined by Kekkonen in [40] as follows.

- Acidic oxides: SiO_2, ZrO_2, TiO_2
- Basic oxides: CaO, MgO, Na_2O, K_2O, Li_2O, FeO, MnO, CrO, CaF_2, etc.
- Amphoteric oxides: Al_2O_3, B_2O_3, Fe_2O_3, Cr_2O_3

The use of the following relationship for α_i^* allows the calculation of the viscosity of a slag without the need for experimental viscosity data. Iida et al. in [38] reported equation 2-62 for the calculation of the modified specific coefficient in the system SiO_2-Al_2O_3-CaO-MgO.

$$\alpha_{Al_2O_3}^* = a \cdot B_i + b \cdot w_{Al_2O_3} + c \tag{2-62}$$

B_i is the basicity index and is calculated as shown in equation 2-63.

$$B_i = \frac{\sum(\alpha_i \cdot w_i)_B}{\sum(\alpha_i \cdot w_i)_A} \tag{2-63}$$

For coefficients a, b and c, Iida et al. defined in [38] the following relationships (equations 2-64 to 2-66).

$$a = 1.20 \cdot 10^{-5} \cdot T^2 - 4.3552 \cdot 10^{-2} \cdot T + 41.16 \tag{2-64}$$

$$b = 1.40 \cdot 10^{-7} \cdot T^2 - 3.4944 \cdot 10^{-4} \cdot T + 0.2062 \tag{2-65}$$

$$c = -8.00 \cdot 10^{-6} \cdot T^2 + 2.5568 \cdot 10^{-2} \cdot T - 22.16 \tag{2-66}$$

The coefficients were determined by Forsbacka et al. in [39] for the same system from experimentally determined viscosity values and are shown in Table 2-IV. For the viscosity calculation, the temperature-dependent functions of a, b and c were taken from [39].

Table 2-IV: Data for the coefficients a, b and c from [39]

T [°C]	**a**	**b**	**c**
1580	1.057	0.0022	-1.019
1600	1.056	0.0058	-1.115
1650	1.038	0.0157	-1.379
1700	0.991	0.0243	-1.587
1750	0.863	0.0186	-1.249

2.4.2.4 Kalmanovitch-Frank

The original Urbain model serves as the basis for the viscosity model according to Kalmanovitch and Frank. The model was improved by the involvement of experimental data. According to Vargas et al. in [36], the viscosity is calculated using equation 2-67.

$$\eta = a \cdot T \cdot e^{b \cdot 10^3/T} \tag{2-67}$$

η is again the viscosity in Pa·s, the two parameters a with unit Pa·s/K and b with unit K are determined as shown in equations 2-68 to 2-73.

$$-\ln a = 0.281 \cdot b + 14.1305 \tag{2-68}$$

$$b = b_0 + b_1 \cdot X_{SiO_2} + b_2 \cdot X_{SiO_2}^2 + b_3 \cdot X_{SiO_2}^3 \tag{2-69}$$

$$b_0 = 13.8 + 39.9355 \cdot \alpha - 44.049 \cdot \alpha^2 \tag{2-70}$$

$$b_1 = 30.481 - 117.1505 \cdot \alpha + 129.9978 \cdot \alpha^2 \tag{2-71}$$

$$b_2 = -40.9429 + 234.0486 \cdot \alpha - 300.04 \cdot \alpha^2 \tag{2-72}$$

$$b_3 = 60.7619 - 153.9276 \cdot \alpha + 211.1616 \cdot \alpha^2 \tag{2-73}$$

For the calculation of the coefficient α, the different species in the slag have to be classified as glass modifier or amphoteric depending on their oxygen content (equation 2-74 to 2-76)

$$\alpha = \frac{x_m}{x_m + x_a} \tag{2-74}$$

$$x_m = X_{FeO} + X_{CaO} + X_{MgO} + X_{Na_2O} + X_{K_2O} + X_{MnO} + X_{NiO} + 2 \cdot \left(X_{TiO_2} + X_{ZrO_2}\right) + 3 \cdot X_{CaF_2} \tag{2-75}$$

$$x_a = X_{Al_2O_3} + X_{Fe_2O_3} + X_{B_2O_3} \tag{2-76}$$

The indices m and a serve as identification of the oxides as glass modifier and amphoteric, respectively. X_i is again the molar fraction of component i.

2.4.2.5 NPL

Mills and Sridhar described in [41] their developed NPL (National Physical Laboratory) model. The model correlates the viscosity of the slag with the structure using the optical basicity. The model is corrected for those cations which are used for charge balance of Al^{3+} in tetrahedral coordination. Furthermore, the model uses the Arrhenius equation to describe the temperature dependence of the slags. According to this model, the viscosity is calculated as shown in equation 2-77.

$$\eta = A \cdot e^{(B/T)} \tag{2-77}$$

η is the viscosity in Pa·s and the parameters A and B are calculated by equation 2-78 and 2-79.

$$\ln A = -232.69 \cdot (\Lambda^{corr})^2 + 357.32 \cdot \Lambda^{corr} - 144.17 \tag{2-78}$$

$$\ln\left(\frac{B}{1000}\right) = -1.77 + \frac{2.88}{\Lambda^{corr}} \tag{2-79}$$

Λ^{corr} is the corrected optical basicity. It is calculated similarly to the theoretical optical basicity Λ. As shown in equation 2-80.

$$\Lambda = \frac{\sum X_i \cdot n_i \cdot \Lambda_i}{\sum X_i \cdot n_i} \tag{2-80}$$

X_i is the molar fraction, n_i the number of oxygen atoms, and Λ_i the optical basicity of the respective species i. To consider the amphoteric AlO_4^{5-} anions, the mole fractions are balanced for Λ^{corr}. The balancing of the AlO_4^{5-} anions is done in terms of charge by cations of basic oxides with higher Λ_i values. The consumed cations thus no longer participate in the depolymerization of the melt. Table 2-V shows the values for Λ_i needed for this work.

Table 2-V: Values of Λ_i [41]

Oxid	SiO_2	CaO	Al_2O_3	MgO	FeO
$\boldsymbol{\Lambda_i}$	0.48	1.0	0.60	0.78	1.0

To illustrate the procedure, an example of this compensation is shown in Table 2-VI (taken from Kekkonen et al. in [40]):

Λ_{K_2O} = 1.4

Table 2-VI: Example balancing mole fractions for calculating viscosity using the NPL model [40]

	Composition [mol.-%]				
	SiO_2	**CaO**	**Al_2O_3**	**MgO**	**K_2O**
Without balancing	50	20	15	10	5
With balancing	50	10	15	10	0

The molar fractions with compensation have to be used for the calculation of Λ^{corr}.

2.5 Experimental methods for activity measurement

In the following chapters, the procedures as well as the background of the most common methods for the experimental determination of activities in slags are discussed in detail.

2.5.1 Slag-Metal equilibration

The equilibration technique is one of the most common methods for measuring the activity of components in liquid slags. It is based on knowing the activity of at least one component in the system to determine the activities of the others. Determination of activity by slag-metal equilibration is based on exchange reactions between the slag components and the liquid metal in equilibrium.

Using this method, Wen et al. in [42], for example, determined the activity of CaO in a CaO-SiO_2-Al_2O_3-MgO slag. Therefore, they equilibrated the slag sample together with tin by heating it to 1600 °C in a CO atmosphere and holding it for 24 hours. Afterwards, they quenched the sample, separated the metal and slag phases, and analyzed both phases. Using the Ca contents in the metal phase after the equilibrium experiments, they were able to calculate a_{CaO} of the slag. The detailed procedure is described in chapter 5.3.

In [43], Kang et al. used this method to determine the SiO_2 activity in the CaO-Al_2O_3-SiO_2-MgO system. However, they had a slightly different approach. They heated the slag together with copper to 1600 °C in a CO atmosphere with well-defined oxygen partial pressure and kept this temperature for 18 hours to reach equilibrium. They then quenched the samples, separated the slag and metal phases, and analyzed both phases. Using the equilibrium between SiO_2 in the slag, Si in the metal and O_2 in the gas phase they were able to subsequently calculate a_{SiO_2} of the slag. The equilibrium and calculations used by the researchers can be seen in equation 2-81 to 2-83.

$$(SiO_2) \rightleftharpoons [Si] + \{O_2\} \qquad \text{2-81}$$

$$\log K = \log \frac{a_{Si} \cdot p_{O_2}}{a_{SiO_2}} = -\frac{49799}{T} + 10.65 \qquad \text{2-82}$$

$$a_{Si} = \gamma_{Si} \cdot X_{Si} \qquad \text{2-83}$$

a_{Si} is the activity of silicon in the reference metal, which is calculated using the activity coefficient γ_{Si} of silicon in copper and the silicon content X_{Si} in copper. Kang et al. took γ_{Si} and the relationship for the equilibrium constant K from literature.

2.5.2 Electrochemical method

In the electrochemical method, a sensor consisting of two different electrodes (metal alloy/metal oxide) is immersed in the liquid slag. These two dissimilar electrodes react differently with a specific oxide in the slag, causing a difference in oxygen potential to form between the two electrodes and creating a galvanic cell. This difference in oxygen potentials causes the formation of an electromotive force (EMF) in the open circuit of the cell. The open circuit voltage E in mV of the galvanic cell formed by the two electrodes in contact with the molten slag can be expressed by the following thermodynamic relation (equation 2-84). [44]-[46]

$$E = \frac{10^{-3} \cdot R \cdot T}{2 \cdot F} \cdot \ln \left(\frac{{p_{O_2}}^{ref}}{{p_{O_2}}^{slag}} \right)^{1/2} \tag{2-84}$$

R and T are the universal gas constant and the temperature, respectively, and F is the Faraday constant. ${p_{O_2}}^{ref}$ and ${p_{O_2}}^{ox}$ represent the oxygen partial pressures at the oxygen reference electrode and slag electrode, respectively. The activity of an oxide a_i contained in the slag and reacting with the electrodes is defined according to equation 2-85. [44]–[46]

$$a_i = \left(\frac{{p_{O_2}}^{slag}}{{\overset{\circ}{p}_{O_2}}^{slag}} \right)^{1/2} \tag{2-85}$$

${\overset{\circ}{p}_{O_2}}^{slag}$ corresponds, for example when measuring FeO activity, to the equilibrium oxygen partial pressure of a mixture of "pure" FeO (l) + Fe (s). [44],[46]

The relationships for ${p_{O_2}}^{ref}$ as well as ${\overset{\circ}{p}_{O_2}}^{slag}$ are taken from the literature for this method. Since this method was used almost exclusively to determine a_{FeO} in slag systems and only theoretical sensors for measuring SiO_2 and CaO activity were described by Turkdogan in [45], this method is not described further. Since this work is concerned with the activity determination of basic slag formers. [17]

2.5.3 Knudsen effusion mass spectrometry (KEMS)

In the KEMS, a condensed sample is loaded into a uniformly heated Knudsen cell and kept at a temperature until equilibrium between the condensed and vapor phases is reached. The vapor phase is continuously sampled by effusion through a small orifice in the lid of the cell. The area of the orifice is in comparison to the surface area of the vaporizing substance so small that the thermodynamic equilibrium in the cell is not disturbed by the effusion of the vapor phase from the cell. Therefore, the composition of the forming molecular beam can be considered as the equilibrium composition of the vapor phase in the cell. The molecular beam is directed into a mass spectrometer. After ionization and separation processes, the ions reach detectors which express the number of impinging ions by means of an intensity value. The measured ion intensities of the respective species are used to determine vapor pressures. Using the vapor pressures, the activity of the respective species can be calculated using the ratio shown in equation 2-9. [47],[48]

Here, a_i again represents the activity of component i in a solution at a temperature T, p_i represents the partial pressure of component i in a solution at a temperature T, and p_i° represents the partial pressure of component i in its standard state (i.e., pure element or compound i at T).

From the measured ion intensities, the partial pressures of the respective species can be calculated as shown in equation 2-86. [48]–[51]

$$p_i = \frac{I_i \cdot T}{S_i} \tag{2-86}$$

I_i is the measured ion intensity of species i, T is the temperature and S_i summarizes several mass spectrometric constants. A detailed description of all quantities follows in the chapter Partial pressure. If the partial pressure of i is determined for a solution and for the pure substance under identical conditions, the relationship shown in equation 2-87 is obtained for the activity.

$$a_i = \frac{p_i}{p_i^{\circ}} = \frac{I_i \cdot T}{S_i} \cdot \frac{S_i}{I_i^{\circ} \cdot T} = \frac{I_i}{I_i^{\circ}} \tag{2-87}$$

I_i° represents the measured ion intensity of component i of the pure substance at temperature T.

Using KEMS, for example, Stolyarova et al. determined the CaO and SiO_2 activity in the binary CaO-SiO_2 system in [52] and the activity of CaO and Al_2O_3 in the binary CaO-Al_2O_3 system 1660 °C in [53].

2.5.4 Comparison of the different methods

A detailed comparison of experimental methods for the determination of thermodynamic activities of individual components in metallurgical slags was made by Abel in [17]. Based on an extensive literature review, KEMS was evaluated as the most suitable method, for the present objectives. This evaluation is because KEMS can be used as a stand-alone method for activity measurements, in contrast to the equilibration technique, which requires the use of either literature data or a second experimental method, and the electrochemical method, where the selection of suitable electrode materials for appropriate sensors is unclear.

In addition to activity determination, KEMS investigations can also be used to investigate the evaporation behavior of a wide variety of substances, as already mentioned, vapor pressures, equilibrium constants, reaction enthalpies and entropies, and Gibbs energy changes. Since this method has rarely been used for metallurgical research purposes, the following chapter will explain the background of KEMS.

3 Principle of Knudsen effusion mass spectrometry

The Knudsen effusion mass spectrometry (KEMS) is an experimental method which provides the highest accuracy equilibrium evaporation studies and gives direct information about thermodynamic properties. [54]–[56]

A Knudsen effusion mass spectrometer setup includes two separable vacuum chambers, a Knudsen cell, a pyrometer, an electron impact ion source, a single focusing magnetic type sector field mass spectrometer, and a collector arrangement for the secondary electron multiplier. A schematic arrangement is shown in Figure 3-1. To reduce ground signal from the ion source, a cryogenic pump filled with liquid nitrogen can be used. Ion getter pumps are used to create an ultra-high vacuum in the mass spectrometer. For the evacuation, for the Knudsen cell chamber a turbomolecular pump is used. This chamber can be separated from the mass analyzer by a shutter. With the shutter, the ion source is also shielded from the molecular beam exiting the Knudsen cell. A condensed sample is placed in the Knudsen cell and kept at constant temperature and ultra-high vacuum until chemical and thermal equilibrium is reached between the condensed and gas phases. The lid of the cell has a small orifice (diameter 0.3-0.5 mm). Via this a small quantity of the gas phase effuses and forms a molecular beam, representing the equilibrium gas phase in the cell. As mentioned above, the small number of molecules leaving the cell practically does not disturb the equilibrium in the cell. The molecular beam enters the ion source wherein the individual species in the gas phase are ionized by electron impact. This ionization process is shown schematically in Figure 3-2. The generated ions are focused by a set of collimating lenses, and an applied acceleration potential increases the kinetic energy of these ions on their way to the entrance slit of the mass analyzer. As a result of the acceleration, all ions with the same charge have almost the same kinetic energy. Different ions show velocities proportional to the reciprocal root of the mass of the respective species. Perpendicularly aligned electric and magnetic fields affect the path of the ions through the sector field analyzer due to their combined effect. Dynamic variation of the electric field strength separates the different ions according to their mass-to-charge ratio. Finally, the ions are reaching the detector, and the measured intensities are proportional to the number of atoms or molecules present in the gas phase. They hit the first dynode of the multiplier there, causing a secondary emission of electrons. Then, a cascade of plates with increasing potential difference amplifies the secondary electrons. Electron emission is enhanced on each plate multiple times, and the quantity of secondary electrons ultimately becomes a shower that is about 10^6 times the initial value. By this point, the number of electrons is high enough to be detected by ion counting. Then a potential drop converts the counted ions into an intensity signal. [55]–[59]

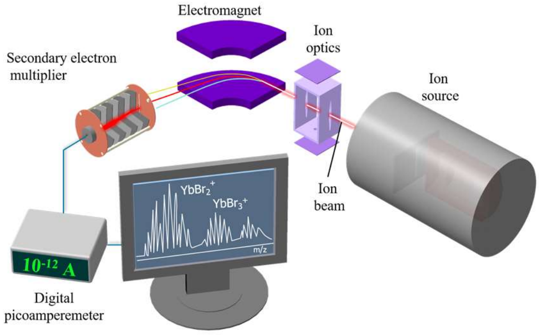

Figure 3-1: Schematic setup of a magnetic sector KEMS [60]

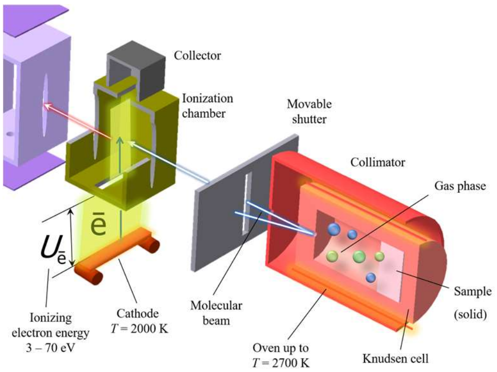

Figure 3-2: Electron ionization process [60]

3.1 Partial pressure

From the measured ion intensities using the KEMS, the partial pressure p_i of the individual species can be calculated using equation 3-1 [54],[55],[58],[59],[61]–[66]:

$$p_i = \frac{k I_i T f_i}{n_i \gamma_i \sigma_i} \qquad 3\text{-}1$$

k is the pressure calibration factor also called instrument sensitivity factor, I_i is the measured ion intensity of species i at the temperature T, T stands for the temperature in Kelvin at the measurement in the Knudsen cell and f_i is the fragmentation correction factor. f_i is the ratio of

M^+ to $\sum M^+$. n_i is the isotopic abundance, γ_i the multiplier factor and σ_i the ionization cross-section of species i. γ_i represents the value of secondary electron emission from the first dynode of a multiplier, depending on the mass and molecular structure, and is set to 1 for the species measured in this work, since an ion counting system was applied in the KEMS used. Consequently, the error of γ_i is assumed to be 0. k describes the transmission of the ions by the mass spectrometer and allows the calculation of absolute partial pressures. k is determined by vaporization experiments of substances with a well-known partial pressure (usually pure metals, e.g., Ag, Au, Ni, Pt [47]) in a defined temperature range (mostly around the melting point). The resulting partial pressure is subsequently compared with literature data in order to determine k. I_i corresponds to the frequency of a specific ion in the molecular beam effusing from the Knudsen cell. The measured intensity from the ion counter can be directly used in Equation 3-1. n_i is calculated as the isotopic abundance of the measured mass relative to the total mass and quantities. It should be noted here that the error of the isotopic abundances is negligible for our purposes. σ_i describes the probability that the initial molecule or atom of species i will be ionized by electron impact at a specific ionization energy. [47],[54],[55],[57],[58],[66]

3.2 Thermodynamic properties

Reactions studied with KEMS include, for example, dissociation and sublimation reactions, which are shown in equations 3-2 to 3-4. [57],[61]

$$AB(g) \rightleftharpoons A(g) + B(g) \qquad 3\text{-}2$$

$$AB(s) \rightleftharpoons A(g) + B(s) \qquad 3\text{-}3$$

$$A(s) \rightleftharpoons A(g) \qquad 3\text{-}4$$

Incongruent and congruent evaporation processes, such as reactions 3-3 and 3-4, are studied to determine thermodynamic properties of condensed phases. If the partial pressures of the individual species in the gas phase are known, the equilibrium constants K_P of these reactions can be determined with the aid of equation 3-5. [47],[54],[57],[61]

$$K_P = \Pi\left(\frac{p_i}{p^\circ}\right)^{\nu_i} \qquad 3\text{-}5$$

ν_i is the stoichiometric coefficient of components in the reaction equation. For standard conditions, the partial pressure according to the Clausius-Clapeyron equation is set to conditions at T = 298 K and p = 1 atm = 101325 Pa = p°. [47],[54],[57],[61]

The enthalpy change related to the reaction can be determined by either the second or third law method. The second law method is based on the van’t Hoff or Clausius-Clapeyron equation, shown in equation 3-6, and enables the calculation of the enthalpy change of the reaction $\Delta_r H_T^{\circ}$ at the mean temperature of the experiment. [47],[55],[57]–[59],[63],[67]–[71]

$$\frac{dlnK_p}{d(1/T)} = -\frac{\Delta_r H_T^{\circ}}{R} \qquad \text{3-6}$$

R is the universal gas constant (8.314 J/mol·K). As shown in equation 3-7, the change in standard Gibbs energy can be defined based on the equilibrium constant. [54],[55],[59],[69],[71],[72]

$$\Delta G_{(T)}^{\circ} = -RTlnK_p = \Delta_r H_T^{\circ} - T\Delta_r S_T^{\circ} \qquad \text{3-7}$$

The rearrangement of equation 3-7 allows a linear plot in an Arrhenius diagram (lnK_p versus $1/T$) and relates the equilibrium constant, enthalpy, and entropy of the reaction. This form is shown in equation 3-8. [47],[54],[55],[58]

$$lnK_p = -\frac{\Delta_r H_T^{\circ}}{R}\frac{1}{T} + \frac{\Delta_r S_T^{\circ}}{R} = -A\frac{1}{T} + B \qquad \text{3-8}$$

This linear representation is used for the determination of the regression coefficient A and the intercept B and therefore for the evaluation of the enthalpy and entropy of the reaction at the mean temperature of the measurement. To convert the enthalpy from the mean temperature of the measurement to the standard temperature (typically 298 K), enthalpy increments $H(T) - H(298)$ must be used. These are available in reference works, for example, in [16],[73] and [71]. [47],[55],[58],[66],[70],[71]

As already mentioned, the reaction enthalpy at standard temperature $\Delta_r H_{298}^{\circ}$ can also be determined using the third law method. The calculation according to the third law method is shown in equation 3-9. Its basis is the known absolute value of the equilibrium constant. According to equation 3-9, the enthalpy of reaction can be calculated for each data point if the change in the Gibbs energy function is known. [47],[57],[59],[68],[70]–[72]:

$$\Delta_r H_{298,3rd}^{\circ} = -T\left[RlnK_p + \Delta_r gef_T^{\circ}\right] \qquad \text{3-9}$$

$\Delta_r gef_T^\circ$ is the change of Gibbs energy function for the investigated reaction. As shown in equation 3-10 $\Delta_r gef_T^\circ$ has to be calculated from the Gibbs energy functions gef_T°, corresponding to the stoichiometry of each species at the measurement temperature. [66]

$$\Delta_r gef_T^\circ = \sum gef_T^\circ\,(products) - \sum gef_T^\circ\,(reactants) \qquad 3\text{-}10$$

gef_T° is calculated as shown below (equation 3-11). [66],[71]

$$gef_T^\circ = \frac{H_T^\circ - H_{298}^\circ}{T} - S_T^\circ \qquad 3\text{-}11$$

H_T° and S_T° are the enthalpy and entropy at standard state pressure (1 bar) and temperature T. H_{298}° is the enthalpy at standard state pressure and temperature (298 K).

Compared to the third law method, the second law method has the advantage that due to the proportionality of $I_i \cdot T$ and p_i, the representation of $\ln\,(I_i \cdot T)$ versus $1/T$ yields a linear plot where the slope equals $\frac{\Delta_r H_{Tm}^\circ}{R}$, eliminating the need to calculate the absolute values of the vapor pressures. [57],[59],[68]

The quality of data analysis by the third law method is generally considered higher than that of analysis by the second law method. [71],[72],[74]

As already described in the chapter Activity and shown in formula 2-9, in equilibrium and in the ideal gas state, the activity of each element can be defined as the ratio between its partial pressure in the system and the saturation vapor pressure when the element is in its pure form at the same temperature. [55]

For the determination of the activity of species i in a multicomponent system, KEMS measurements must be performed in a specific temperature range for the multicomponent system with species i present and the pure compound i. The observed intensities are proportional to the partial pressures p_i, as shown in equations 2-87 and 3-1. As already mentioned, partial pressures can be determined directly from the measured ion intensities of the corresponding species by means of equation 3-1, but for this purpose all quantities used in equation 3-1 should be known exactly. The activity of the components in the oxidic system whose partial pressures are determined by the KEMS method can be easily determined for a given temperature range (equation 2-87) if the partial pressure of the corresponding pure compound is also measured with the same experimental setup and under the same conditions.

4 Experimental

The following chapters describe the materials used, processing procedures, test setups as well as the test procedures and the obtained results.

4.1 Materials used

For the determination of the diffusion coefficients as well as activities of individual slag components, different slag types were prepared, the procedure is described in chapter Slags. The preparation of the CaO samples for the dissolution tests is explained in chapter 4.1.2. The MgO samples were obtained from the companies Tateho Ozark® and Aremco™. According to the manufacturers, these exhibited a purity of ≥99 wt.-%. The average densities were 3134.10 kg/m^3 for the samples from Tateho Ozark® and 2604.19 kg/m^3 for those from Aremco™. This corresponds to relative densities of 87 and 73%, respectively. The SiO_2 specimens were fused silica rods from GVB™, with a purity and density of ≥99.99 wt.-% and 2200 kg/m^3 (relative density 83%) as specified by the manufacturer. The Al_2O_3 specimens were made from Aliaxis® alumina rods. The manufacturer specified a purity of ≥99.5 wt.-% and a density of 3950 kg/m^3, which equals a relative density of 99%. The spinel specimens were provided by RHI MAGNESITA®. These had a density of 2854.54 kg/m^3 (relative density 80%). The chemical composition of the $MgAl_2O_4$ samples is given in Table 4-I.

Table 4-I: Chemical composition of the spinel samples [wt.-%]

SiO_2	CaO	Al_2O_3	MgO	Fe_2O_3	P_2O_5	MnO	ZrO_2
0.37	0.43	68.27	30.39	0.31	0.02	0.02	0.20

The quartz, alumina and $MgAl_2O_4$ specimens were machined using diamond tools. The desired geometries of the various specimens are shown in Figure 4-1 to Figure 4-4. The geometries of the CaO samples also corresponded to the dimensions shown in Figure 4-1 and Figure 4-2.

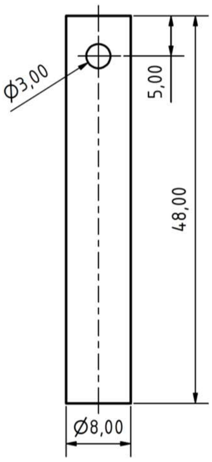

Figure 4-1: Standard sample geometry

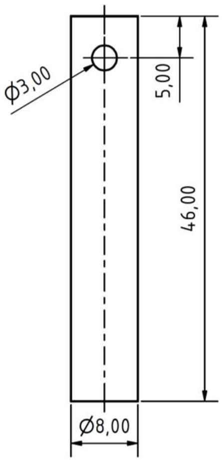

Figure 4-2: Sample geometry for dissolution tests in BOF slag

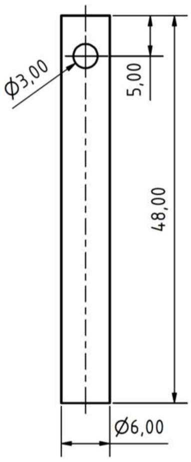

Figure 4-3: Geometry of Al_2O_3 samples

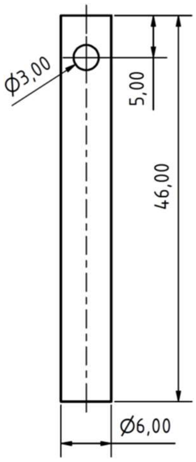

Figure 4-4: Geometry of MgO samples for dissolution tests in BOF slag at 1400 °C.

The graphite and iron crucibles used for the dissolution tests were manufactured by Henschke GmbH and Austrex GesmbH, respectively. The dimensions of the two crucibles were the same. A technical sketch can be seen in Figure 4-5.

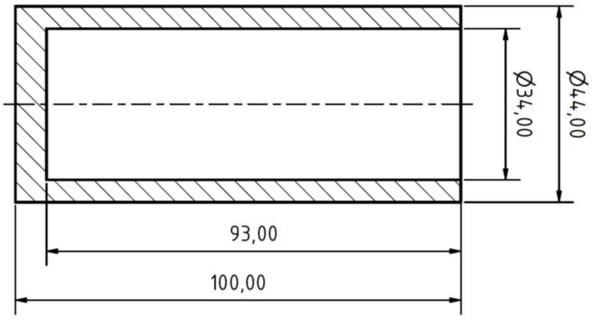

Figure 4-5: Crucible geometry

The pure substances for the KEMS measurements were CaO powder with a purity of 99.998% (Thermo Scientific™) and MgO powder with a purity of 99.999% (ROTI® METIC).

4.1.1 Slags

The slag compositions shown in Table 4-II were defined for the determination of diffusion coefficients as well as activities.

Table 4-II: Defined slag compositions [wt.-%]

Slag type	**Composition [wt.-%]**				
	SiO_2	**CaO**	**Al_2O_3**	**MgO**	**FeO**
BF	40	40	15	5	-
BOF	30	30	-	-	40
CA	5	50	45	-	-
Woll	45	40	15	-	-
LF*	50	45	5	-	-
DS**	15	50	30	5	-
DS sat.**	12.8	56.7	25.5	5	-
DS super sat.**	9.5	66.5	19	5	

*only diffusion coefficients determined

**only activities determined

The abbreviations BF, BOF, CA, Woll and LF stand for blast furnace, basic oxygen furnace, calcium aluminate, wollastonite and ladle furnace slag, respectively. DS denotes desulphurization slag, the addition sat. for the CaO saturation of the slag and super sat. for the CaO supersaturation of the slag.

In a first step of the slag production process, the respective oxides were mixed in powder form in the required quantities. The purities of the oxides used, and the suppliers are listed in Table 4-III. The FeO used to produce the BOF slag was produced in the laboratory of the Chair of Ferrous Metallurgy by an appropriate reduction of iron ore using a fluidized bed reactor. Ore from a Brazilian mine was used as raw material for the preparation of FeO. This ore is ideal to produce FeO due to its high iron content and the low amounts of associated elements. To convert the Fe_2O_3 present in the ore into FeO, a reduction degree of 33.3% has to be achieved.

By continuously monitoring the mass loss of the input material during the reduction, the process can be stopped when the desired reduction degree is reached. The reduction was carried out at ~900 °C and with H_2 as reducing agent.

Table 4-III: Purities and suppliers of the slag components [wt.-%]

Oxide	**Purity [wt.-%]**	**Supplier**
CaO	≥97	Sigma Aldrich®
SiO_2	≥99.5	Sigma Aldrich®
Al_2O_3	≥98.6	Thermo Fisher Scientific®
MgO	≥99	Sigma Aldrich®
FeO	89	In house

The individual slag mixtures were placed in a graphite crucible, suitable for the induction furnace of the MU900 model series of the company INDUTHERM®. The different slags were heated up to 1600 °C with an input power of 15 kW in this furnace. In the case of the FeO containing BOF slag, the individual components were weighed into an Al_2O_3 crucible, and this was then placed in the graphite crucible of the induction furnace. The power of the induction furnace was set to 3.5 kW at the beginning of the melting process, after reaching 300 °C the power was increased to 5 kW until 500 °C was reached. Subsequently, the furnace was heated up to 900 °C with 7 kW. The final heating up to 1600 °C was carried out with 9 kW. In the case of the BOF slag, the slower heating was to prevent thermal shock-induced failure of the Al_2O_3 crucible used. During the heating process, purging with nitrogen at a flow rate of 1000 Nl/min was done to counteract the oxidation of the graphite crucible with the atmospheric oxygen. After reaching the desired temperature, it was held for 5 minutes. The slag was stirred after the holding time using a graphite rod. The stirring on the one hand caused the slag components sticking to the crucible wall to be transferred to the liquid pool and on the other hand accelerated the dissolution of the components that were not yet dissolved. Stirring was followed by a further holding period of 10 minutes to ensure uniform heating of the liquid slag. Before pouring and the associated quenching of the slag into a steel mold, the slag was stirred again. To prevent excessive dissolution of the alumina crucible in the case of BOF slag and thus avoid deviation of the slag composition, the BOF slag was stirred after reaching 1600 °C and poured directly. The stirring was performed using an iron rod. The glassy solidified slags were removed from the steel mold after cooling and the chemical composition was analyzed by EDX. The analysis results are listed in Table 4-IV.

Table 4-IV: Measured slag compositions [wt.-%]

Slag type	**Composition [wt.-%]**				
	SiO_2	**CaO**	**Al_2O_3**	**MgO**	**FeO**
BF	40.2	39.6	15.1	5.2	-
BOF	31.1	31.7	1.8	-	35.4
CA	5.1	51.0	43.6	0.4	-
Woll	45.1	38.8	16.0	0.2	-
LF	46.7	48.3	5.0	-	-
DS	15.5	48.6	30.3	5.6	-
DS sat.	12.4	56.4	25.9	5.3	-
DS super sat.	10.0	65.7	20.8	3.5	-

4.1.2 CaO samples

CaO powder with a purity of 97.8 wt.-% and a grain size ≤63 µm was used to produce the CaO specimens. This was provided by the company Lhoist®. The powder was dried prior to pressing and sintering to eliminate possible crack formation due to evaporation of moisture within the specimens during the sintering process. Immediately after drying, approximately 20 g of the powder was weighed into the press die designed to produce the samples. The punch was then inserted into the die, and the powder was compacted with a force of 10 tons. The design drawings of all components and the assembly of the pressing device are shown in Figure 4-6 to Figure 4-9. The base plate is a grinded steel plate with the dimensions 200x80x10 mm.

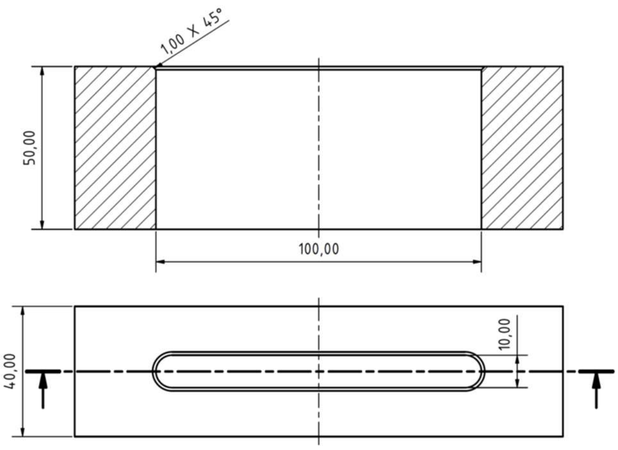

Figure 4-6: Press die

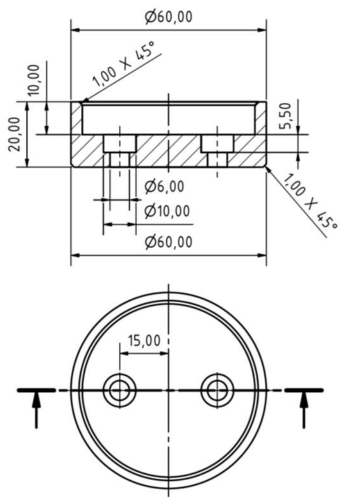

Figure 4-7: Punch attachment

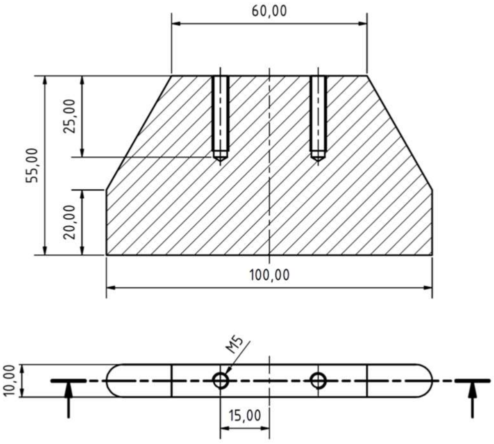

Figure 4-8: Press punch

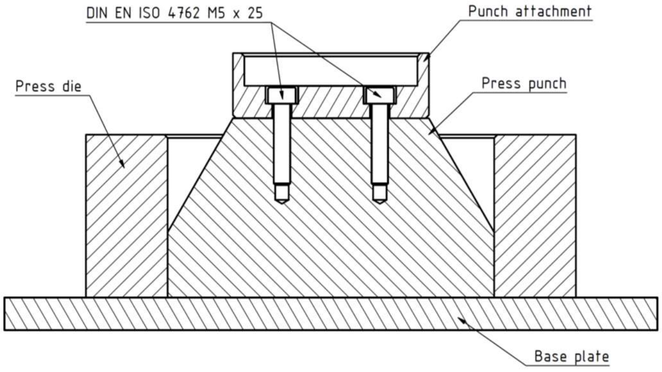

Figure 4-9: Assembly pressing device

To obtain a relatively homogeneous sample density, the press punch was removed from the die after the first compaction step, the die was turned over and the punch was reinserted on the other side. The second compaction of the specimen was again carried out with a force of 10 tons. Finally, the bottom plate was removed, and the double-pressed green body was removed from the die. After removal, a hole with a diameter of 3 mm was drilled into the green bodies. Finally, the pressings were placed on a zirconia firing base and loaded into the furnace. The furnace was a resistance-heated furnace from CARBOLITE GERO 30-3000°C® with the model number HTR-V100-250/17. The samples were heated to a temperature of 1700 °C with a heating rate of 350 °C/h. The sintering temperature was held for 60 minutes and then the specimens were cooled in the furnace with 350 °C/h. Prior to a dissolution test, the specimen was cut to the defined length using a diamond cutting disc and a dremel and ground to the required diameter using SiC grinding paper with a grit size of 80 in a lathe. To reduce the surface roughness, each specimen was finally grinded using a SiC grinding paper with a grit size of 1200.

4.2 Experimental setup dissolution experiments

For the determination of the diffusion coefficients, an experimental setup was designed which allows dissolution tests under reproducible conditions. The dissolution tests were carried out in a gas-tight high-temperature vertical tube furnace of the type HTRV 100-250/18 from CARBOLITE GERO 30-3000 °C®, which is shown schematically in Figure 4-10 and Figure 4-11. It is a resistance-heated furnace. The gas tight Al_2O_3 furnace tube is equipped with sealing rings at both ends, which are glued on. These sealing rings are inserted into water-cooled flanges. O-rings fitted in a notch inside the flanges are used for sealing. The rotating shaft shown in Figure 4-11 allows the setting of a defined slag flow. The upper part of the rotating shaft is a water-cooled steel shaft on which a graphite shaft is mounted using a sleeve. The shaft is connected to a linear unit with a spindle drive, which allows a continuous height change. A shaft attachment made of graphite was mounted to the graphite shaft by a split pin connection. The split pin is made of graphite. The pin connection was secured by a graphite ring. After an initial series of tests, the concept was modified, and a separate specimen holder was added to the test setup. This was also connected to the shaft attachment by a split pin connection, which was again secured by a graphite ring. The split pin is either made of graphite or, in the case of the dissolution tests in BOF slag, of Al_2O_3. This specimen holder covers the specimen in the sample/slag/atmosphere interface. This prevents increased dissolution, caused by the Marangoni effect in this area. The specimen holder is made of graphite except for those tests in BOF slag. For the dissolution tests in BOF slag, it is made of iron. To avoid carburization of the iron specimen holder, a resulting decrease in the melting temperature and finally melting of the specimen holder, an Al_2O_3 sleeve was placed between the graphite shaft attachment and the iron specimen holder. The respective specimens were in turn connected to the specimen holder by a split pin. The split pin was made of graphite or, in the case of the dissolution tests in BOF slag, of iron wire. For all dissolution tests in FeO-free slags, graphite crucibles were used. For the dissolution tests in FeO containing slag, iron crucibles were used. To prevent damage to the furnace in case of a possible crucible breakage, the graphite or iron crucibles were placed in a protective Al_2O_3 crucible. Detailed views of the different experimental setups are shown in Figure 4-12 and Figure 4-13. The temperature was measured, and the heating power controlled by means of two B-type thermocouples. One of the two thermocouples is located directly below the crucible, thus allowing precise adjustment of the slag temperature.

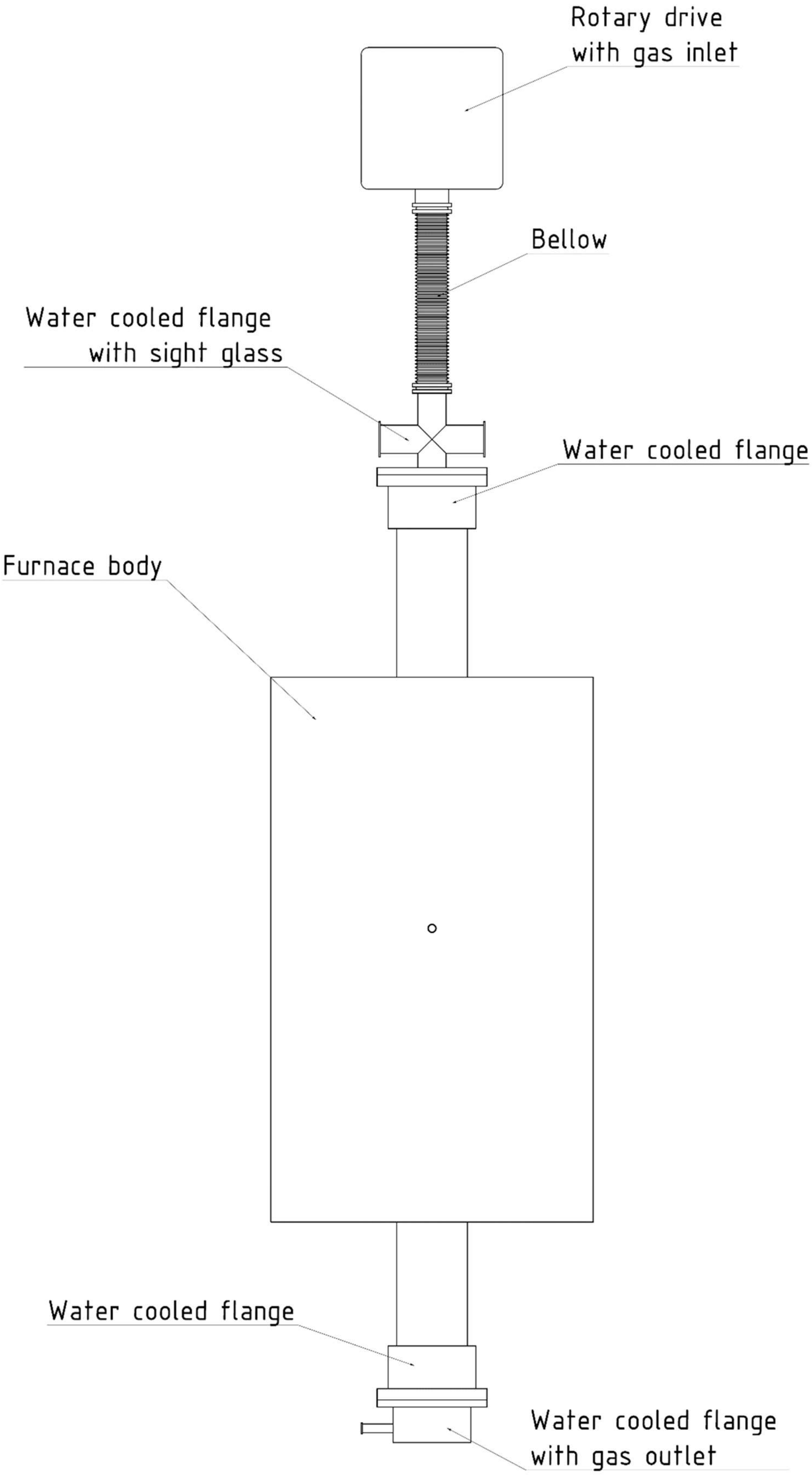

Figure 4-10: High temperature vertical tube furnace

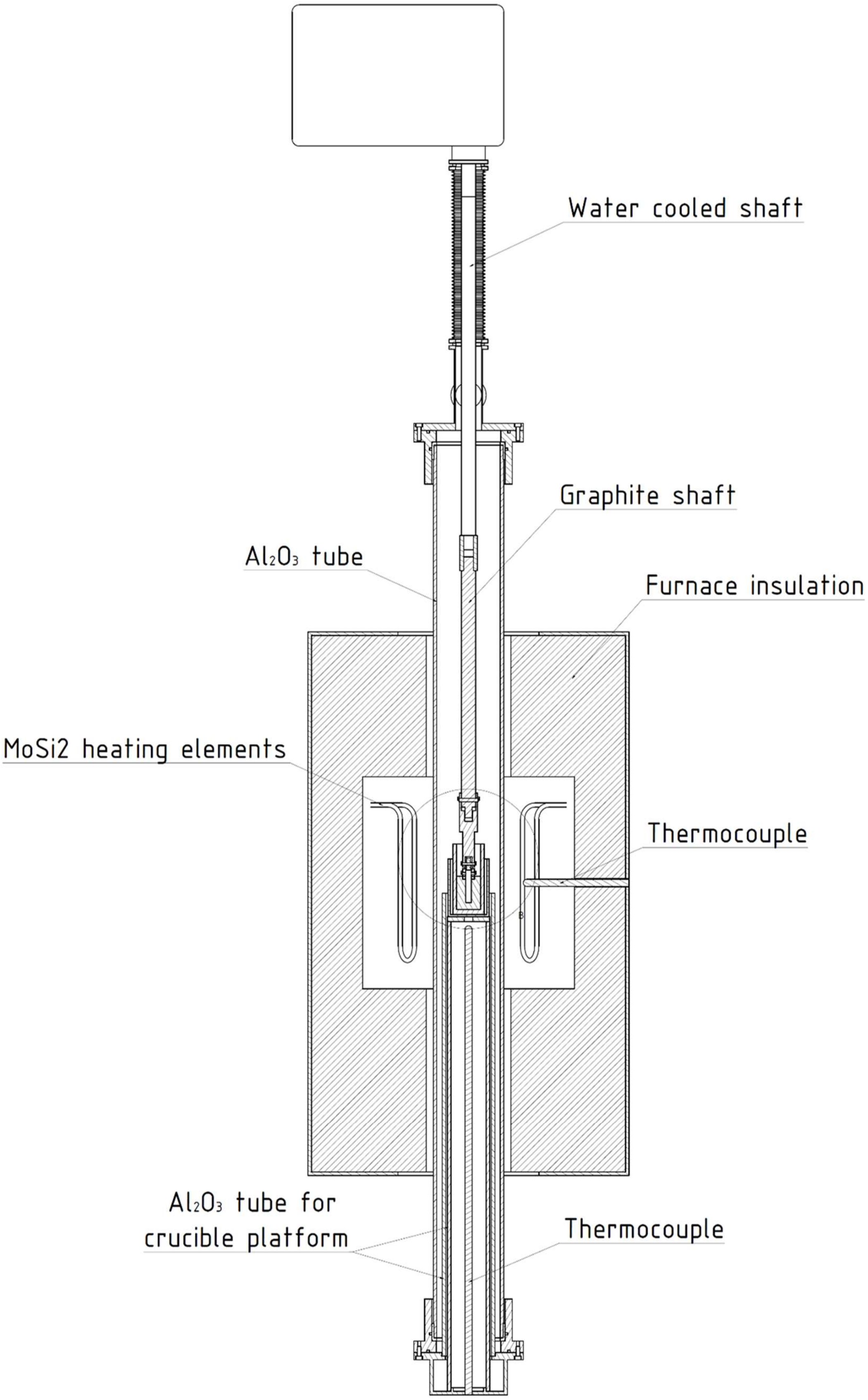

Figure 4-11: Section through high temperature vertical tube furnace

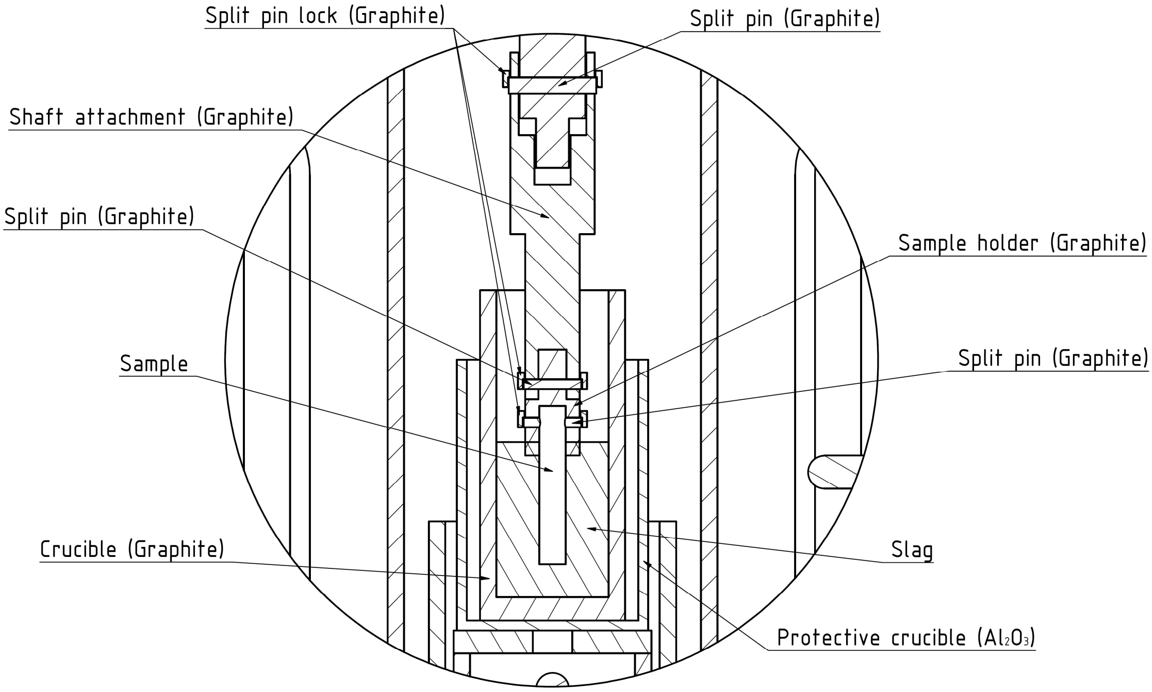

Figure 4-12: Experimental setup for dissolution tests in FeO-free slags

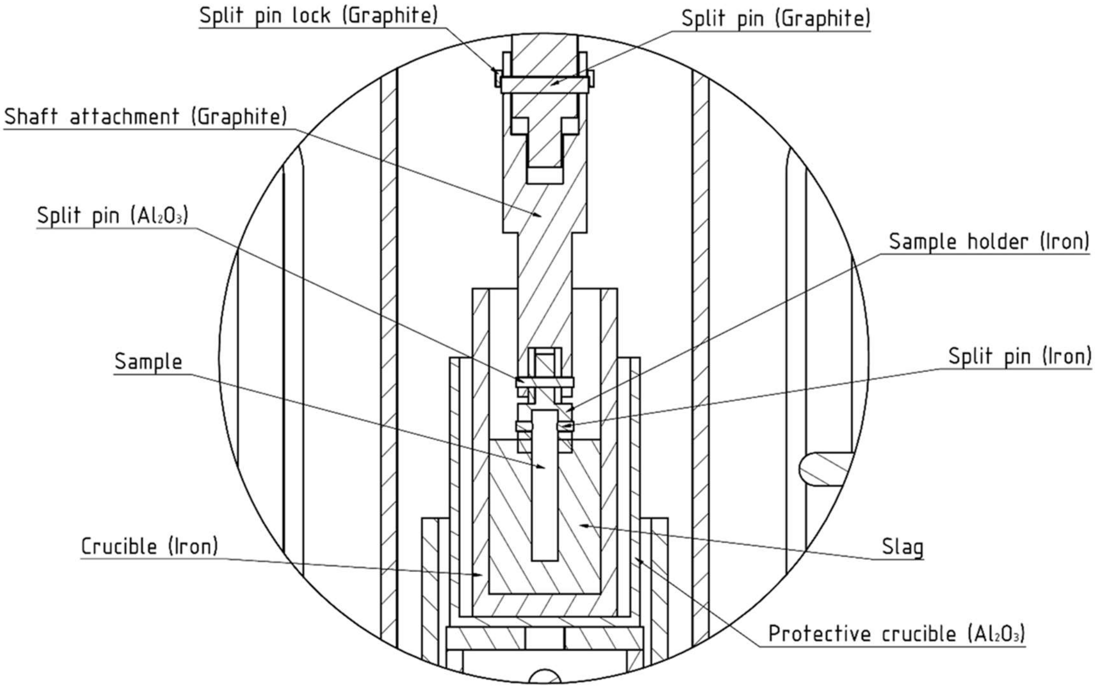

Figure 4-13: Experimental setup for dissolution tests in FeO-containing slag

4.3 Experimental procedure of dissolution experiments

The test temperatures were defined as 1500 and 1600 °C. Due to the use of iron components in the experimental setup for the experiments with BOF slag, the test temperatures were reduced to 1400 and 1500 °C. For the dissolution tests, either 80 g of the glassy BF, Woll or LF slag, 90 g of CA slag or 100 g of BOF slag were weighed into the graphite or iron crucible for each test. The different slag masses result from the different slag densities to ensure sufficient immersion depth.

After the glassy slags were weighed into the crucible, the crucible was placed in the protective crucible and both together on the crucible platform of the furnace. The crucible platform was then inserted into the furnace. The furnace was then closed at the bottom and the off-gas system was attached. Before the samples were installed, they were measured and weighed. The measurement scheme is shown schematically in Figure 4-14. The distance between the individual measuring points was 5 mm. The specimens were rotated by 45° between the individual measuring positions.

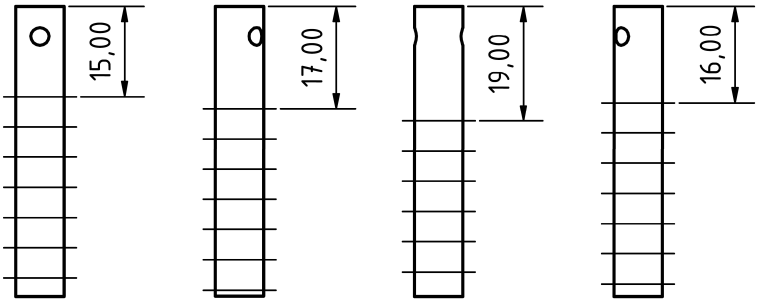

Figure 4-14: Measurement scheme of the samples

The next step was to connect the specimen to the shaft attachment, this to the specimen holder and the graphite shaft. After connecting all components and securing all split pin connections, the furnace was sealed gas tight at the top with the bellow. Subsequently, the sample was placed in the furnace just above the crucible using the linear unit. The position of the specimen directly above the crucible ensured that the temperature of the slag and the sample were the same. This, in turn, prevented the slag from "freezing" on a colder sample, resulting in a delayed dissolution. Delayed dissolution would result from the need to melt the solidified slag on the sample before the actual dissolution process. Another reason for this position of the test specimens is to avoid possible failure of the samples due to thermal shock. Since there would be an abrupt heating of the specimens if they were moved from the "cold" furnace area into the heating zone. Before the heating process, the furnace was purged with 400 Nl/h of inert gas for 10 minutes to displace the atmosphere in the furnace. Within these 10 minutes, the furnace volume has been exchanged ~7 times by the introduced inert gas volume. After the purging process, both gas inlet and outlet systems were switched from purging to heating operation. The two systems differ in an additional flow meter at the gas inlet and a 20 mbar pressure relief valve at the gas outlet. The inert gas flow rate was adjusted in heating mode to achieve an overpressure of at least 20 mbar. As soon as the overpressure was reached, the heating process was started. The heating rate was 300 °C/h for all experiments. All dissolution experiments were performed under nitrogen atmosphere to exclude possible reactions with atmospheric oxygen. These possible reactions refer to reactions between slag, sample as well as the graphite components with the atmospheric oxygen. After reaching the specified test temperature, it was kept for one hour to ensure a homogeneous temperature distribution within the slag and the sample as well as a uniform temperature of the slag and the sample as far as possible. After the holding time, the test specimens were set in rotation. The rotation speed for all dissolution tests was 100 rpm. As soon as the shaft reached the defined rotational speed, the test specimens were inserted into the slag and held there for the respective dissolution time. After the predefined dissolution time, the rotating samples were removed from the slag and moved to their original starting position above the crucible. There, the rotational movement was stopped. As soon as the rotation was finished, the specimens were moved into the "cold" furnace area with the linear unit. This caused a rapid cooling of the specimens and thus prevented an excessive reaction of the specimens with the partly adhering slag. Excessive reaction would have corrupted the results of the measurement by ongoing dissolution. The furnace then cooled with 300 °C/h under nitrogen atmosphere. Once the furnace had cooled down, it was opened, and the slag-containing crucible and the partly dissolved samples were removed. The specimens were measured according to the same scheme as before the experiments.

4.4 Calculation model

The diffusion coefficient from the dissolution tests was calculated using a calculation model based on the experimental setup. The parameters required for the calculation are:

- Slag composition
- Slag mass
- Saturation concentration of the slag for the investigated oxide w_s
- Sample density ρ_{sample}
- Dimensions of the sample (radius; immersion length in the slag) R_1, l
- Inner radius of the crucible in which the sample rotates during the experiment R_2

- Immersion time of the specimen into the slag
- Test temperature T
- Rotation speed of the specimen u
- Diameter of the specimen after the dissolution test

The slag mass was determined by weighing with an accuracy of 2 decimal places. The saturation concentrations of the various slags for CaO and MgO at the respective temperatures were calculated using FactSage™ 7.3 and the FToxid database. These are given in Table 4-V.

Table 4-V: $w_{s,CaO}$ and $w_{s,MgO}$ as a function of temperature and slag composition

Slag	T [°C]	$w_{s,CaO}$ [wt.-%]	$w_{s,MgO}$ [wt.-%]
BF	1500	60.73	18.73
	1600	61.20	19.74
BOF	1400	53.51	14.38
	1500	54.36	15.95
CA	1500	58.47	7.47
	1600	59.08	9.25
Woll	1500	64.12	21.04
	1600	64.46	21.94

The saturation concentrations of the ladle furnace slag at 1550 °C for Al_2O_3, SiO_2 and $MgAl_2O_4$ are given in Table 4-VI. The spinel saturation concentration is calculated from the sum of the MgO and Al_2O_3 content of the slag at 1550 °C, as soon as pure $MgAl_2O_4$ precipitates.

Table 4-VI: w_{s,Al_2O_3}, w_{s,SiO_2} and theoretical $w_{s,MgAl_2O_4}$ of LF slag at 1550 °C

w_{s,Al_2O_3} [wt.-%]	w_{s,SiO_2} [wt.-%]	$w_{s,MgAl_2O_4}$ [wt.-%]
48.47	68.76	45.10

In the following ternary systems (Figure 4-15 to Figure 4-22), the different slag types are shown with the theoretical compositional evolution during the dissolution of CaO samples at the different experimental temperatures. All calculations were performed with FactSage™ 7.3 using the FToxide and, in the case of the BOF slag, also the FactPS database. In the case of the quaternary system of the BF slag, the change in composition is an approximation, since the MgO content is assumed to be constant in this figure.

● Initial slag composition
● CaO saturation concentration
— Theoretical change of composition

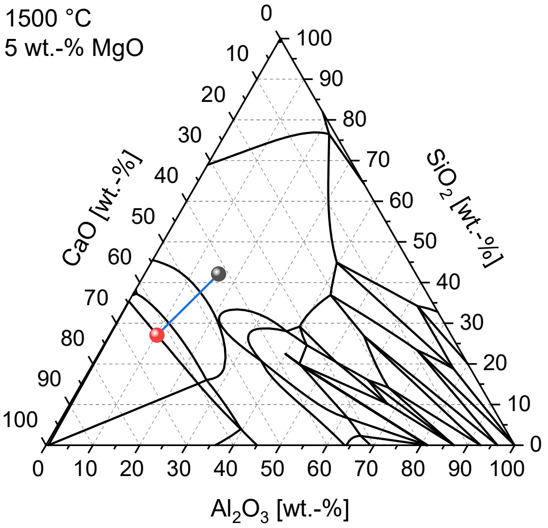

Figure 4-15: Composition change during CaO dissolution; 1500 °C; BF slag

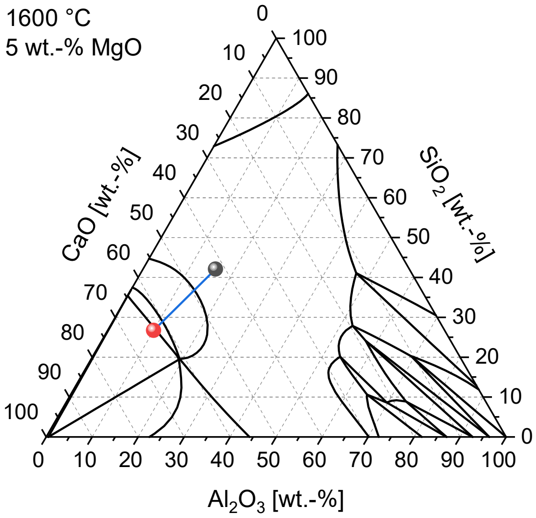

Figure 4-16: Composition change during CaO dissolution; 1600 °C; BF slag.

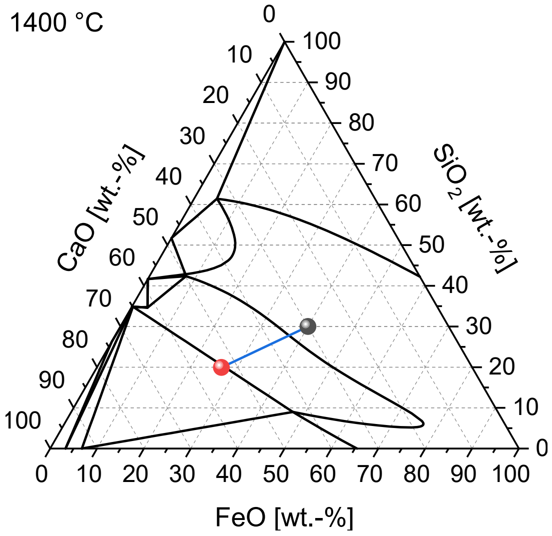

Figure 4-17: Composition change during CaO dissolution; 1400 °C; BOF slag

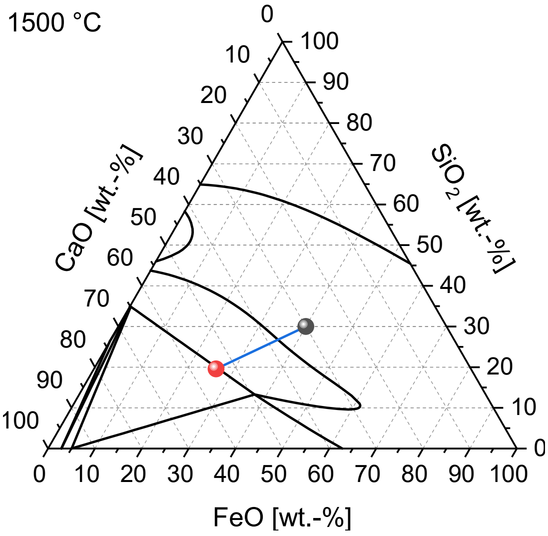

Figure 4-18: Composition change during CaO dissolution; 1500 °C; BOF slag

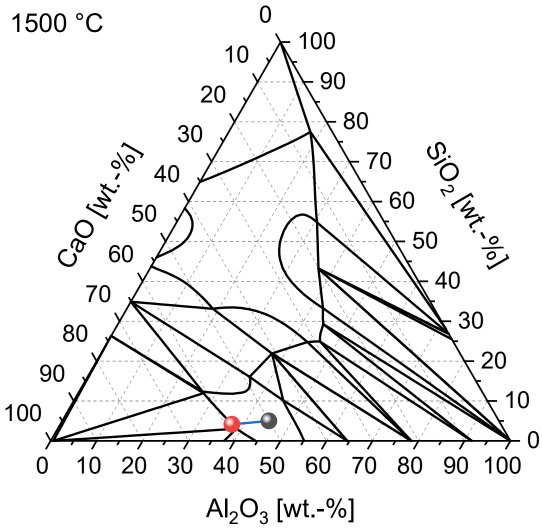

Figure 4-19: Composition change during CaO dissolution; 1500 °C; CA slag

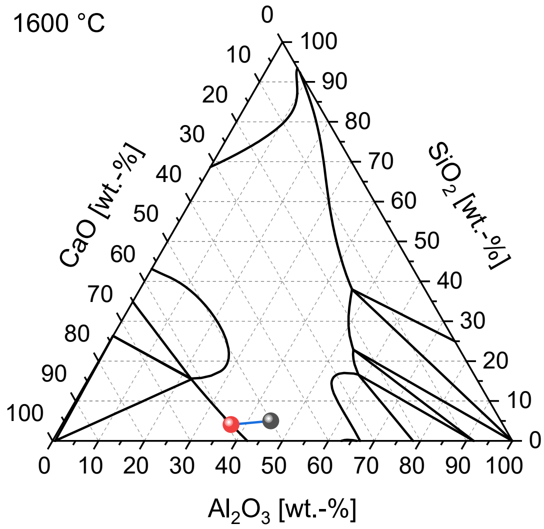

Figure 4-20: Composition change during CaO dissolution; 1600 °C; CA slag

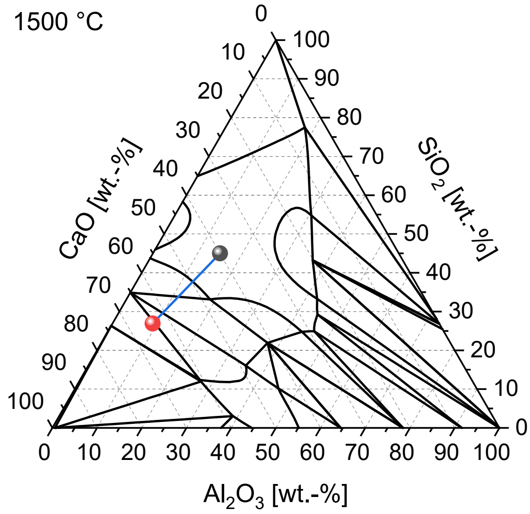

Figure 4-21: Composition change during CaO dissolution; 1500 °C; Woll slag

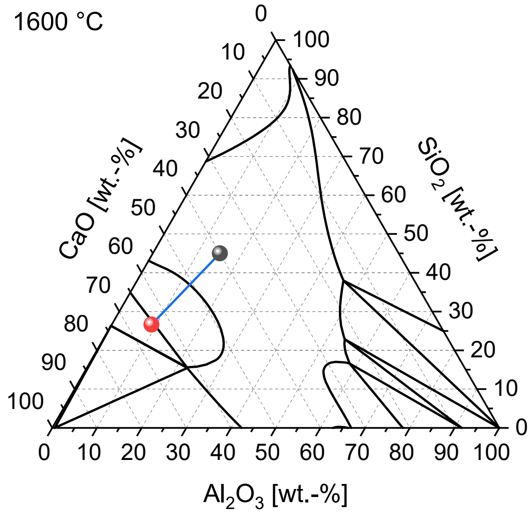

Figure 4-22: Composition change during CaO dissolution; 1600 °C; Woll slag

For a better illustration of the theoretical change in slag composition during MgO dissolution, only the phase boundaries of the liquid slag were shown in Figure 4-23 to Figure 4-30 as a function of the MgO content. These are three-dimensional representations of the quaternary systems CaO-Al_2O_3-SiO_2-MgO and CaO-FeO-SiO_2-MgO.

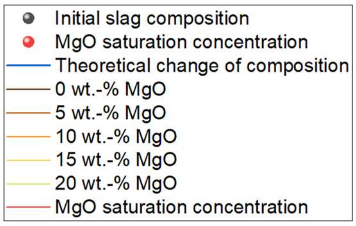

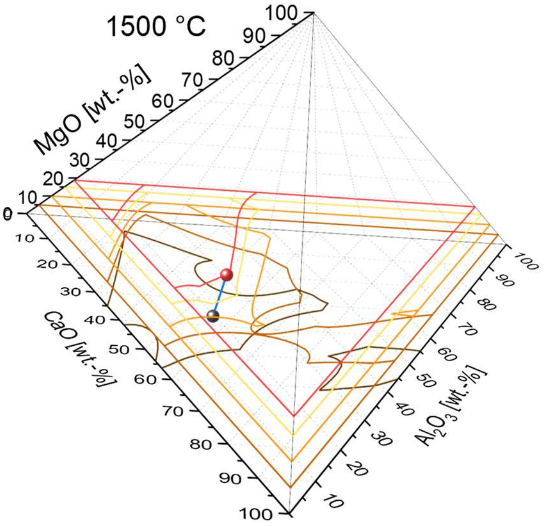

Figure 4-23: Composition change during MgO dissolution; 1500 °C; BF slag

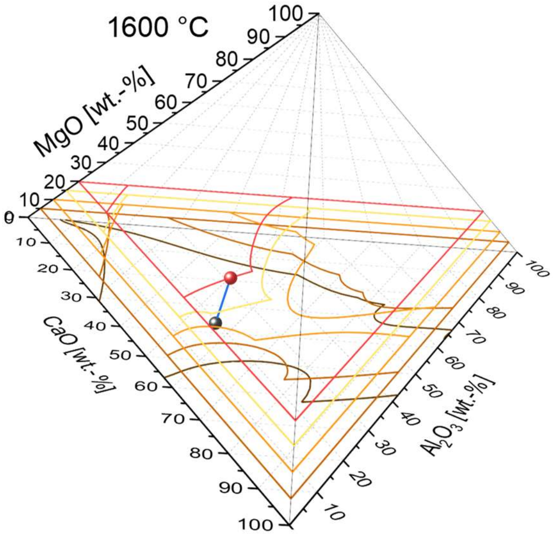

Figure 4-24: Composition change during MgO dissolution; 1600 °C; BF slag

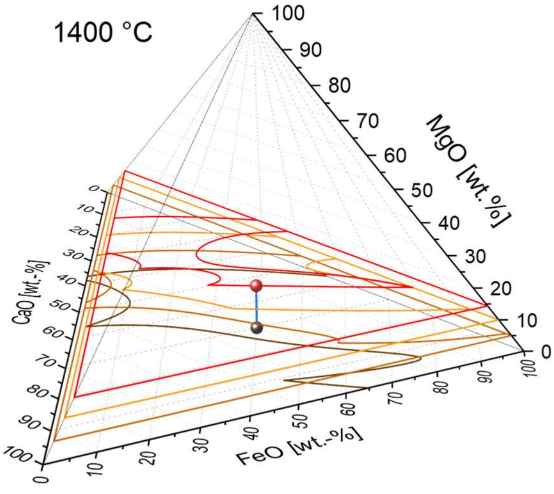

Figure 4-25: Composition change during MgO dissolution; 1400 °C; BOF slag

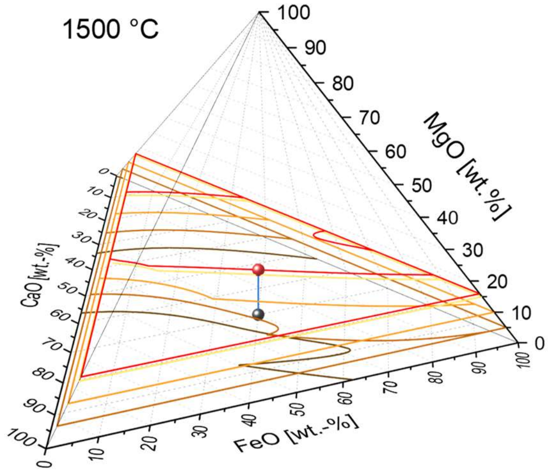

Figure 4-26: Composition change during MgO dissolution; 1500 °C; BOF slag

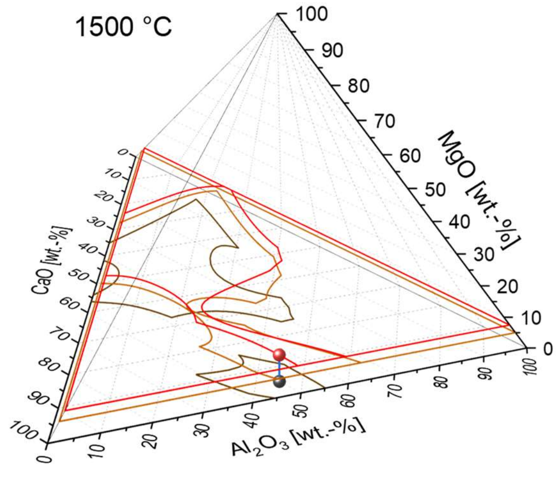

Figure 4-27: Composition change during MgO dissolution; 1500 °C; CA slag

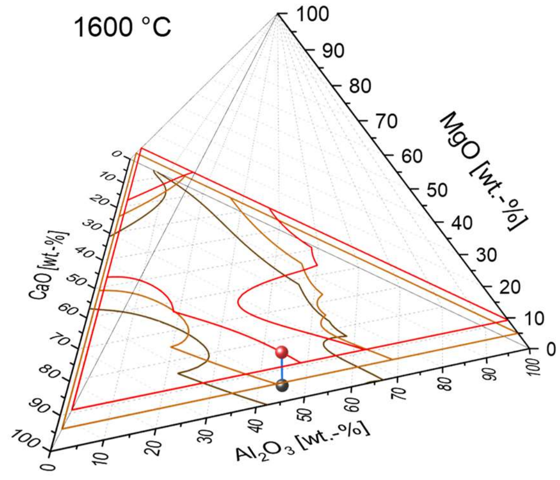

Figure 4-28: Composition change during MgO dissolution; 1600 °C; CA slag

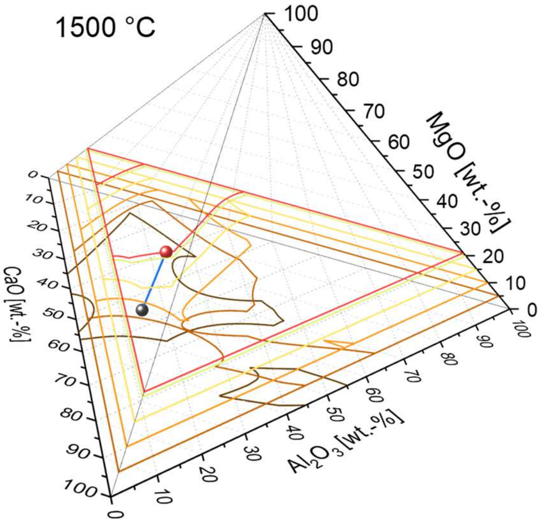

Figure 4-29: Composition change during MgO dissolution; 1500 °C; Woll slag

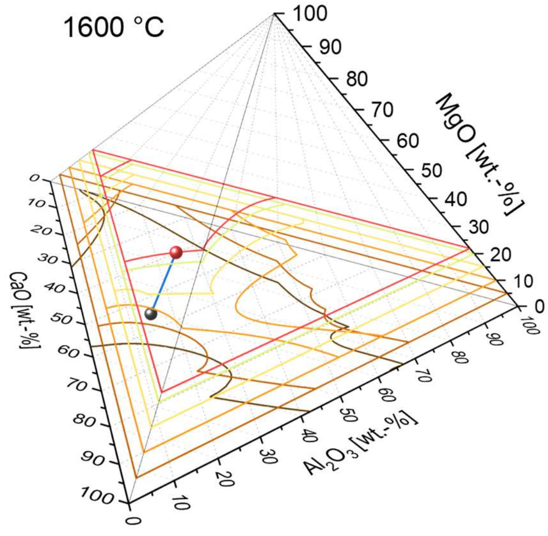

Figure 4-30: Composition change during MgO dissolution; 1600 °C; Woll slag

To further simplify the plot, the CaO, SiO_2, Al_2O_3 and FeO contents of the individual slags were scaled to 100 wt.-% and plotted in two-dimensional form. These representations are shown below (Figure 4-31 to Figure 4-38). Due to the normalization, it seems that the initial slag composition in these figures is equal to the MgO saturation concentration.

● Initial slag composition / MgO saturation concentration
— 0 wt.-% MgO
— 5 wt.-% MgO
— 10 wt.-% MgO
— 15 wt.-% MgO
— 20 wt.-% MgO
— MgO saturation concentration

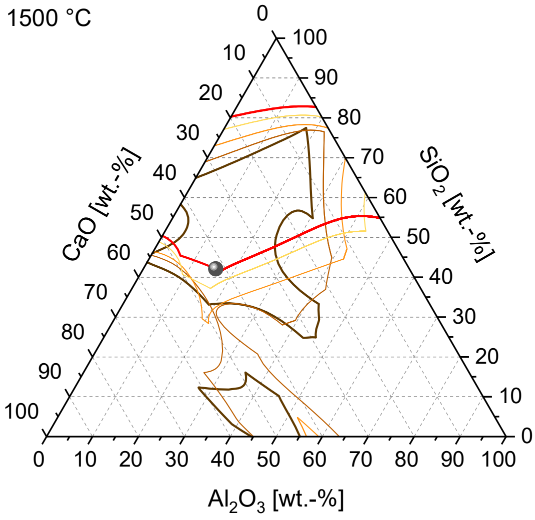

Figure 4-31: Change of phase boundaries as a function of MgO content; 1500 °C; BF slag

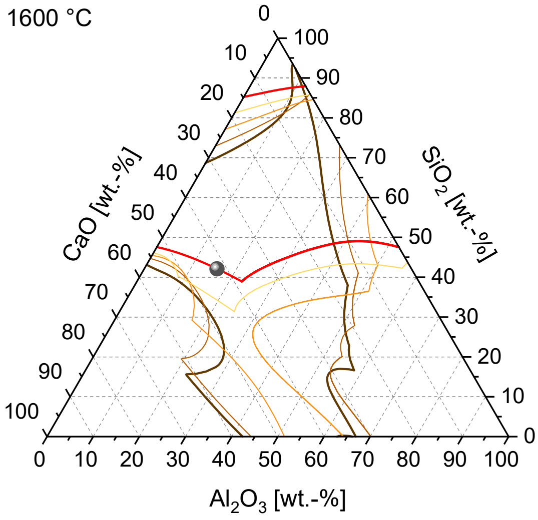

Figure 4-32: Change of phase boundaries as a function of MgO content; 1600 °C; BF slag

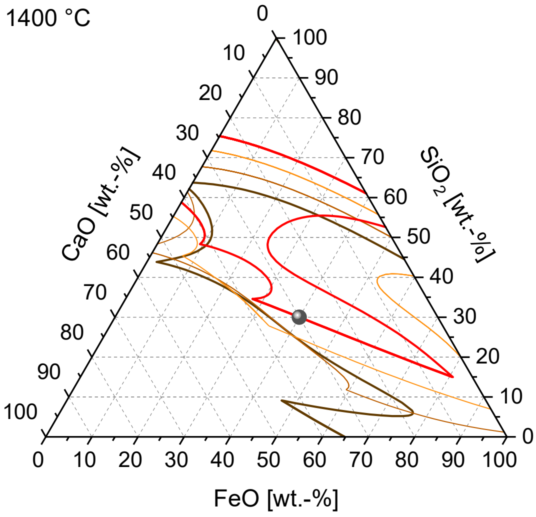

Figure 4-33: Change of phase boundaries as a function of MgO content; 1400 °C; BOF slag

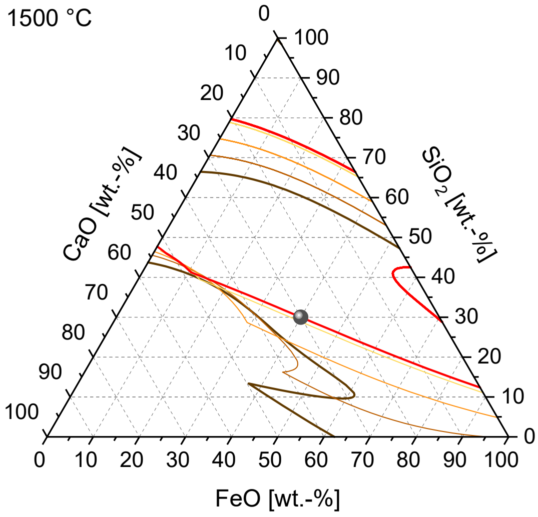

Figure 4-34: Change of phase boundaries as a function of MgO content; 1500 °C; BOF slag

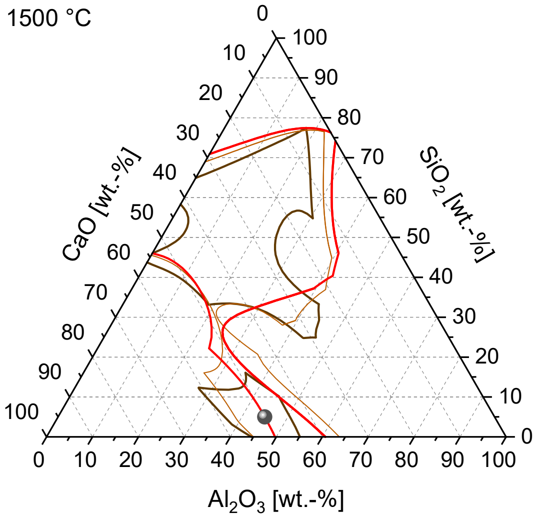

Figure 4-35: Change of phase boundaries as a function of MgO content; 1500 °C; CA slag

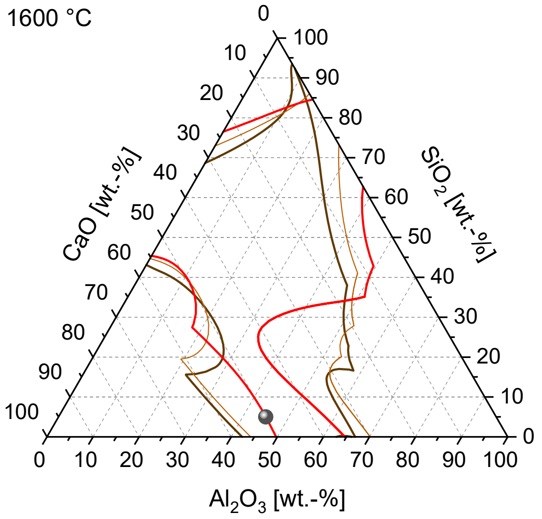

Figure 4-36: Change of phase boundaries as a function of MgO content; 1600 °C; CA slag

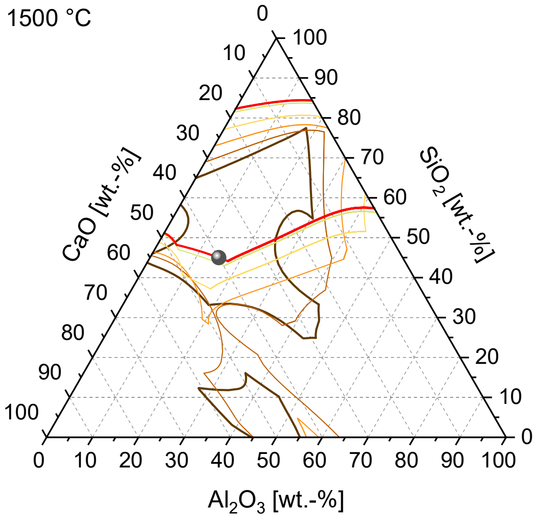

Figure 4-37: Change of phase boundaries as a function of MgO content; 1500 °C; Woll slag

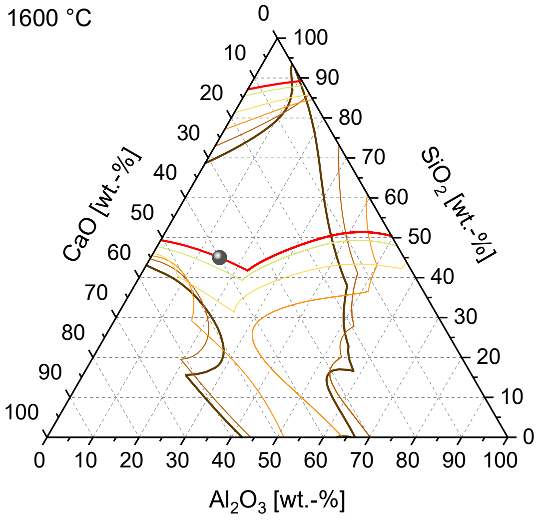

Figure 4-38: Change of phase boundaries as a function of MgO content; 1600 °C; Woll slag

Figure 4-39 shows the theoretical composition changes of the LF slag during the dissolution of Al_2O_3 and SiO_2 at 1550 °C.

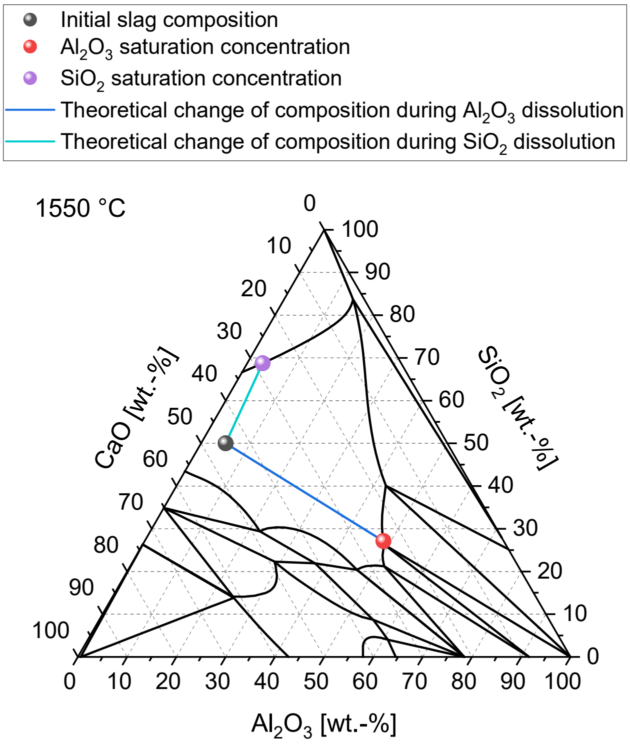

Figure 4-39: Composition change during Al_2O_3 or SiO_2 dissolution; 1550 °C; LF slag

To represent the saturation composition during the dissolution of spinel in LF slag, the quaternary system $CaO\text{-}Al_2O_3\text{-}SiO_2\text{-}MgO$ has to be shown again. In Figure 4-40 and Figure 4-41, respectively, the slag system is shown in three dimensions again and for easier visualization in two dimensions. In the two-dimensional representation, only the shift of the slag composition in the direction of Al_2O_3 can be seen.

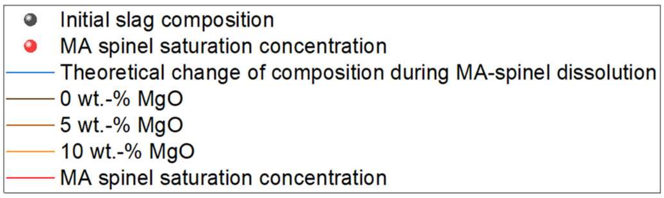

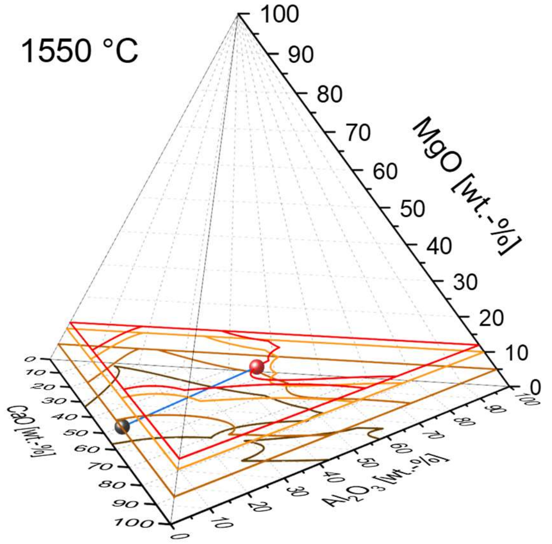

Figure 4-40: Composition change during MgAl$_2$O$_4$ dissolution; 1550 °C; LF slag; 3D plot

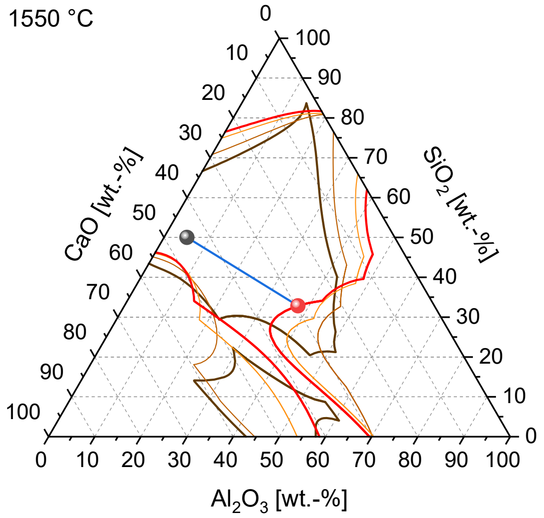

Figure 4-41: Composition change during MgAl$_2$O$_4$ dissolution; 1550 °C; LF slag; 2D plot

The sample density was determined by weighing and measuring the virgin samples. Using the dimensions, a 3D model of the specimens was created to obtain an accurate volume. The diameter of the samples as well as the immersion length were determined in the same way as for the density determination by measuring the corroded specimens. The inner diameter of the crucibles was taken from the manufacturer's specifications but was controlled before each experiment. The immersion time was monitored, starting when the linear unit was at the lower end point. The experimental temperature was measured by a type-B thermocouple positioned directly below the crucible. The rotation speed was taken from the integrated process monitoring system of the high temperature vertical tube furnace. The diameter after the dissolution tests was measured in the same way as for the initial samples.

Based on the input data, the calculation of the following parameters is performed:

- Average total mass flow $\bar{j}_{tot}$
- Mass transfer parameter B
- Slag density ρ_S
- Dynamic slag viscosity η
- Kinematic slag viscosity ν
- Effective diffusion coefficient D_{eff}

As described in the previous chapter, various models are used to calculate slag viscosity. To identify the most suitable model for each slag, the model results are compared with experimentally determined viscosities of slags with comparable test temperature and composition. The values of the viscosity measurements used were collected by Duchnese in [75].

The densities and viscosities calculated for the respective slags as a function of composition and temperature are listed in Table 4-VII together with the viscosity model used.

Table 4-VII: Calculated slag density and viscosity as a function of temperature and composition

Slag	T [°C]	ρ_S [kg/m^3]	η [Pa·s]	ν [m^2/s]	**Viscosity model**
BF	1500	2639.45	0.52	$1.95 \cdot 10^{-4}$	BBHLW
	1600	2620.17	0.24	$9.29 \cdot 10^{-5}$	BBHLW
BOF	1400	3170.77	0.09	$2.99 \cdot 10^{-5}$	NPL
	1500	3147.14	0.07	$2.31 \cdot 10^{-5}$	NPL
CA	1500	2758.69	0.54	$1.97 \cdot 10^{-4}$	Kalmanovitch-Frank
	1600	2718.00	0.30	$1.11 \cdot 10^{-4}$	Kalmanovitch-Frank
Woll	1500	2587.61	1.09	$4.22 \cdot 10^{-4}$	BBHLW
	1600	2569.23	0.48	$1.86 \cdot 10^{-4}$	BBHLW
LF	1550	2580.32	0.34	$1.33 \cdot 10^{-4}$	Iida

4.5 Results of dissolution tests

Figure 4-42 to Figure 4-45 show the radius decreases of the different oxide samples in the different slags at the respective experimental temperatures as a function of the immersion time.

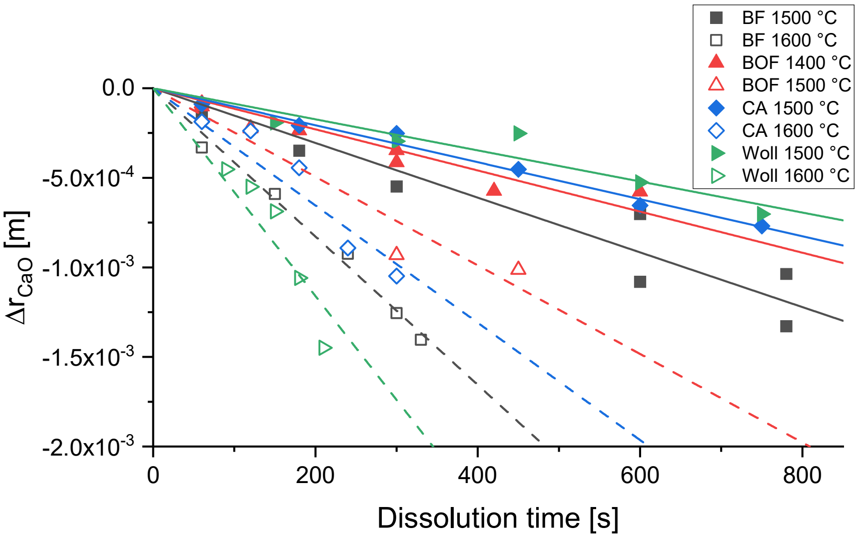

Figure 4-42: Radius decrease of CaO samples as a function of immersion time

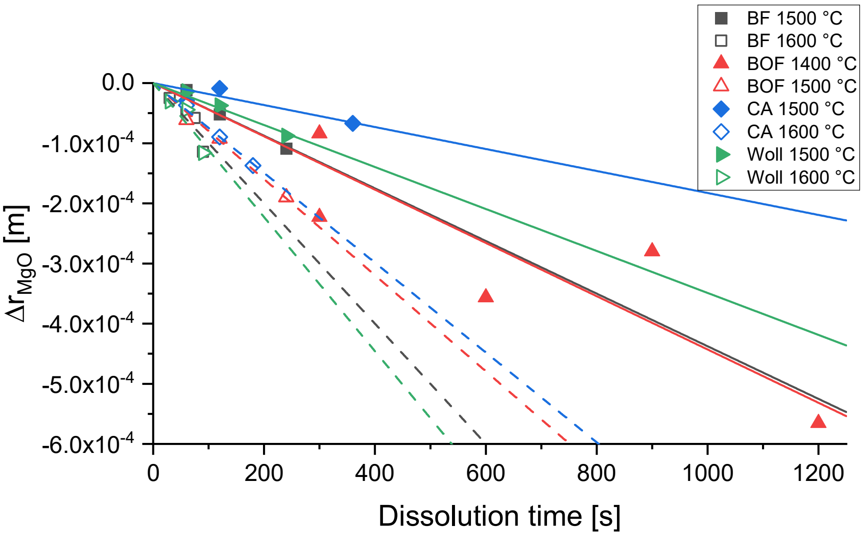

Figure 4-43: Radius decrease of MgO samples as a function of immersion time

All MgO dissolution tests, except those at 1400 °C in BOF slag, were carried out with Aremco™ test specimens. Those at 1400 °C in BOF slag with samples from Tateho Ozark®. As can be seen from Figure 4-43, significantly longer dissolution times were achieved with these specimens, compared to the Aremco™ specimens for BOF slag at 1500°C. This can be explained by the higher density and higher strength of the Tateho Ozark® specimens compared to those of Aremco™. Since the sample density is considered in the calculation of the diffusion coefficients, this will not affect the results. For a better illustration of the results, Figure 4-44 shows an illustration with lower radius decrease and dissolution time.

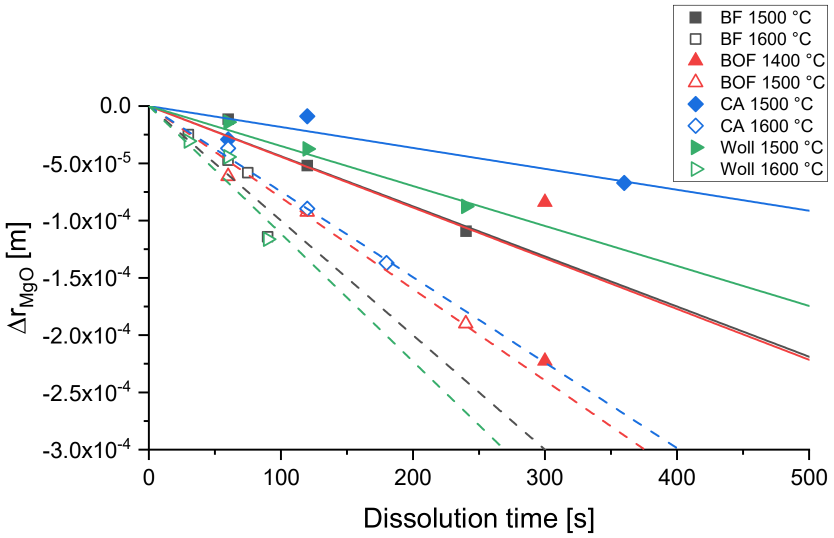

Figure 4-44: Extract from radius decrease of MgO samples as a function of immersion time

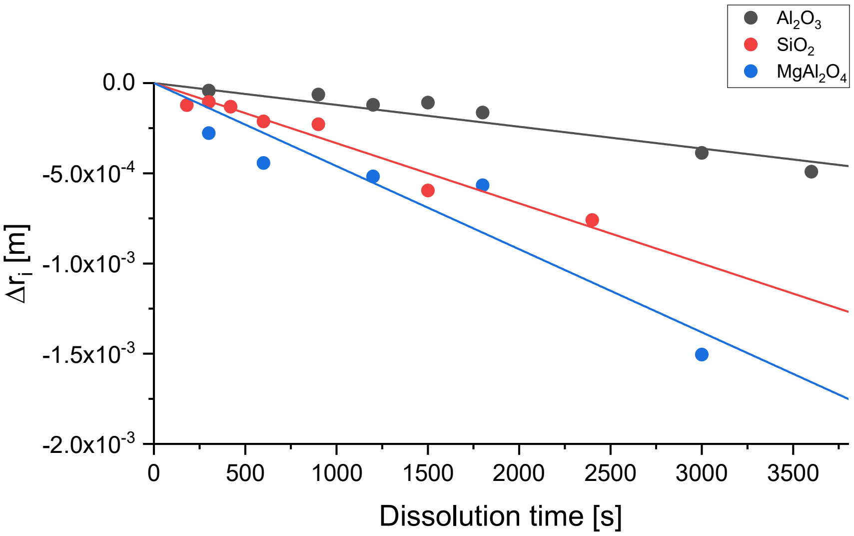

Figure 4-45: Radius decrease of samples in LF slag at 1550 °C as a function of immersion time

Figure 4-42 to Figure 4-44 show that the dissolution rate of CaO and MgO in a slag is higher at increased temperatures. This can be explained on the one hand by the decrease in slag viscosity and on the other hand by the increase in the saturation concentration of the slag, both leading to an increase in the driving force for dissolution. The decrease in viscosity and thus the increase in diffusivity in the slag is likely to be the main factor since the saturation concentration increases only minimally. The relationship between the diffusion coefficient D and the slag viscosity η is described by the Stokes-Einstein relationship, shown in equation 4-1. [76]–[78]

$$D = \frac{k_b \cdot T}{6 \cdot \pi \cdot r \cdot \eta} \qquad 4\text{-}1$$

k_b is the Boltzmann constant, T stands for the temperature in K and r is the radius of the diffusing species. However, in [78], [77] and [79] it is noted that the calculation of D using equation 4-1 deviates from experimentally determined values. From Figure 4-45 it can be seen that the dissolution rate of spinel is faster than that of SiO_2 and this faster than that of Al_2O_3 in the used LF slag at 1550 °C. The higher dissolution rate of SiO_2 compared to Al_2O_3 can be attributed to the much higher saturation concentration of the slag for SiO_2 and the size of the diffusing species if one assumes the diffusion of Si^{4+} ions as Yu et al. did in [80]. If one assumes the diffusion of silicate ions (SiO_4^{4-}, $Si_2O_7^{6-}$, $Si_3O_{10}^{8-}$, etc.) as Maroufi et al. did in [81], this is not the case, as they can be quite large. Comparing the dissolution rate of $MgAl_2O_4$ and Al_2O_3, the higher dissolution rate of the spinel samples could be explained by a higher diffusion coefficient of the Mg^{2+} ions compared to the Al-O ion complexes, as already reported by Valdez et al. in [79].

Taking the radius decreases as well as sample densities and immersion lengths into account, the mass loss could be calculated and consequently the mass loss rate determined. From the mass loss rate, the mass flow density was calculated by including the immersed area. Finally, the diffusion coefficients of the respective oxides in the different slags at the various temperatures were obtained from the determined values. The mass loss rates, average mass flow densities and diffusion coefficients are shown in Table 4-VIII to Table 4-X.

Table 4-VIII: Results of CaO dissolution tests

Slag	T [°C]	dm/dt [kg/s]	$\bar{j}_{tot}$ [kg/m²·s]	$D_{eff,CaO}$ [m²/s]
BF	1500	$-3.05 \cdot 10^{-6}$	$3.55 \cdot 10^{-3}$	$4.14 \cdot 10^{-9}$
	1600	$-8.27 \cdot 10^{-6}$	$9.58 \cdot 10^{-3}$	$1.26 \cdot 10^{-8}$
BOF	1400	$-2.61 \cdot 10^{-6}$	$3.10 \cdot 10^{-3}$	$1.55 \cdot 10^{-9}$
	1500	$-5.46 \cdot 10^{-6}$	$6.19 \cdot 10^{-3}$	$3.68 \cdot 10^{-9}$
CA	1500	$-2.36 \cdot 10^{-6}$	$2.63 \cdot 10^{-3}$	$7.83 \cdot 10^{-9}$
	1600	$-7.17 \cdot 10^{-6}$	$8.03 \cdot 10^{-3}$	$2.85 \cdot 10^{-8}$
Woll	1500	$-1.90 \cdot 10^{-6}$	$2.25 \cdot 10^{-3}$	$2.19 \cdot 10^{-9}$
	1600	$-1.26 \cdot 10^{-5}$	$1.39 \cdot 10^{-2}$	$2.09 \cdot 10^{-8}$

Table 4-IX: Results of MgO dissolution tests

Slag	T [°C]	dm/dt [kg/s]	$\bar{j}_{tot}$ [kg/m²·s]	$D_{eff,MgO}$ [m²/s]
BF	1500	$-9.18\cdot10^{-7}$	$1.08\cdot10^{-3}$	$3.10\cdot10^{-9}$
	1600	$-2.09\cdot10^{-6}$	$2.42\cdot10^{-3}$	$6.89\cdot10^{-9}$
BOF	1400	$-7.88\cdot10^{-7}$	$1.17\cdot10^{-3}$	$2.21\cdot10^{-9}$
	1500	$-1.65\cdot10^{-6}$	$1.93\cdot10^{-3}$	$3.05\cdot10^{-9}$
CA	1500	$-3.79\cdot10^{-7}$	$4.42\cdot10^{-4}$	$2.21\cdot10^{-9}$
	1600	$-1.55\cdot10^{-6}$	$1.81\cdot10^{-3}$	$9.86\cdot10^{-9}$
Woll	1500	$-7.28\cdot10^{-7}$	$8.51\cdot10^{-4}$	$1.65\cdot10^{-9}$
	1600	$-2.32\cdot10^{-6}$	$2.70\cdot10^{-3}$	$6.07\cdot10^{-9}$

Table 4-X: Results of dissolution tests in LF slag at 1550 °C

Oxide	dm/dt [kg/s]	$\bar{j}_{tot}$ [kg/m²·s]	$D_{eff,i}$ [m²/s]
Al_2O_3	$-2.60\cdot10^{-7}$	$3.90\cdot10^{-4}$	$1.43\cdot10^{-10}$
SiO_2	$-5.42\cdot10^{-7}$	$6.22\cdot10^{-4}$	$2.93\cdot10^{-10}$
$MgAl_2O_4$	$-7.61\cdot10^{-7}$	$1.01\cdot10^{-3}$	$4.12\cdot10^{-10}$

The diffusion coefficient for $MgAl_2O_4$ is a hypothetical value because it is not possible to predict exactly which phase will be dissolved and whether the dissolution of a phase will lead to erosion. Therefore, the mass loss or dissolution rate dr/dt should be used for interpretation in this case. The dissolution rate of the spinel samples is $-4.60\cdot10^{-7}$ m/s.

Table 4-XI and Table 4-XII show a correlation matrix between $D_{eff,CaO}$ and $D_{eff,MgO}$ with the parameters $\bar{j}_{tot}$, B, $1/\nu$ and ν.

Table 4-XI: Correlation matrix of $D_{eff,CaO}$

	$\boldsymbol{T}$	$\boldsymbol{\nu}$	$\boldsymbol{1/\nu}$	$\boldsymbol{B}$	$\boldsymbol{\bar{j}_{tot}}$	$\boldsymbol{D_{eff,CaO}}$
$\boldsymbol{T}$	1.00					
$\boldsymbol{\nu}$	0.07	1.00				
$\boldsymbol{1/\nu}$	-0.49	-0.73	1.00			
$\boldsymbol{B}$	-0.03	0.28	0.06	1.00		
$\boldsymbol{\bar{j}_{tot}}$	0.79	-0.26	-0.10	0.26	1.00	
$\boldsymbol{D_{eff,CaO}}$	0.82	-0.13	-0.36	-0.32	0.73	1.00

Table 4-XII: Correlation matrix of $D_{eff,MgO}$

	$\boldsymbol{T}$	$\boldsymbol{\nu}$	$\boldsymbol{1/\nu}$	$\boldsymbol{B}$	$\boldsymbol{\bar{j}_{tot}}$	$\boldsymbol{D_{eff,MgO}}$
$\boldsymbol{T}$	1.00					
$\boldsymbol{\nu}$	0.07	1.00				
$\boldsymbol{1/\nu}$	-0.49	-0.73	1.00			
$\boldsymbol{B}$	0.11	0.40	-0.06	1.00		
$\boldsymbol{\bar{j}_{tot}}$	0.68	-0.40	0.14	0.42	1.00	
$\boldsymbol{D_{eff,MgO}}$	0.82	-0.29	-0.22	-0.17	0.77	1.00

Considering the relationships between the parameters, the signs of the correlation matrix should be as shown in Table 4-XIII.

Table 4-XIII: Positive or negative correlation of the parameters

	$\boldsymbol{T}$	$\boldsymbol{\nu}$	$\boldsymbol{1/\nu}$	$\boldsymbol{B}$	$\boldsymbol{D_{eff,i}}$
$\boldsymbol{T}$	1.00				
$\boldsymbol{\nu}$	-	1.00			
$\boldsymbol{1/\nu}$	+	-	1.00		
$\boldsymbol{B}$	+	-	+	1.00	
$\boldsymbol{D_{eff,i}}$	+	-	+	+	1.00

If we now compare the actual relationship between the parameters (Table 4-XIII) with the correlation matrices, an error order of 6 out of a maximum of 10 results for Table 4-XI and Table 4-XII. This suggests that such an analysis is only of limited benefit. Due to the highly diverse slags, the properties are not as interrelated globally as they are supposed to be, so the correlations must be considered separately for each slag. Figure 4-46 and Figure 4-47 show the relationship between the determined diffusion coefficient of CaO and MgO with ν, B and $\bar{j}_{tot}$. Considering only the effects of ν and B on $\bar{j}_{tot}$, the general trend is that as B increases and slag viscosities decrease, $\bar{j}_{tot}$ increases. Contrary to this trend are the results of the dissolution tests in BOF slag. In this case, despite low slag viscosity and average value for B, only a low value for $\bar{j}_{tot}$ is obtained. However, only the consideration of all three parameters allows the interpretation of the resulting diffusion coefficients. For example, if low values for B and high slag viscosities result in a high value for $\bar{j}_{tot}$, high diffusion coefficients will be obtained. Accordingly, the CA slag at 1600 °C exhibits the highest diffusion coefficient due to the combination of far below average values for B, compared to the other slags as well as temperatures, only slightly below average value for v and above average values for $\bar{j}_{tot}$ for both CaO and MgO. Another example would be the Woll slag at 1500 °C. Here, only a low value for $\bar{j}_{tot}$ is observed despite the high value of B, most likely due to the high slag viscosity, resulting in a low value for the diffusion coefficients.

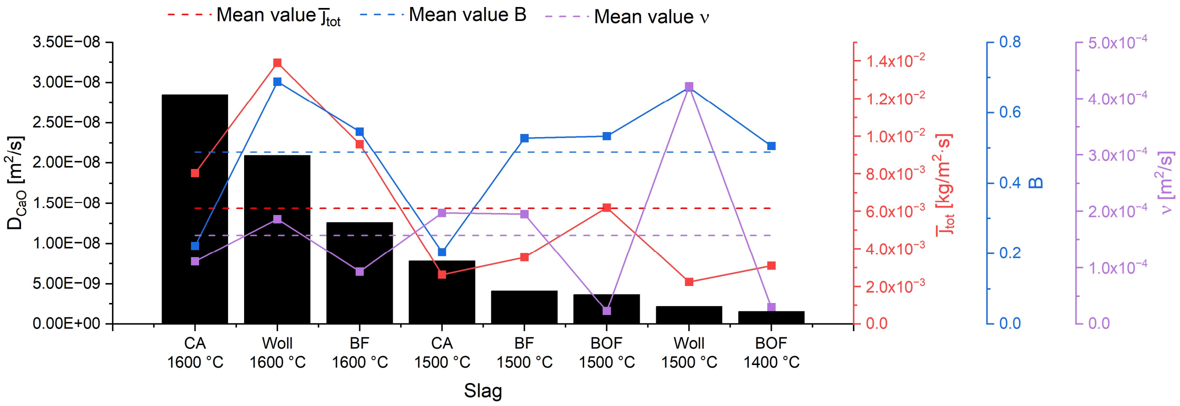

Figure 4-46: Relationship between $D_{eff,CaO}$, $\bar{j}_{tot}$, B and ν

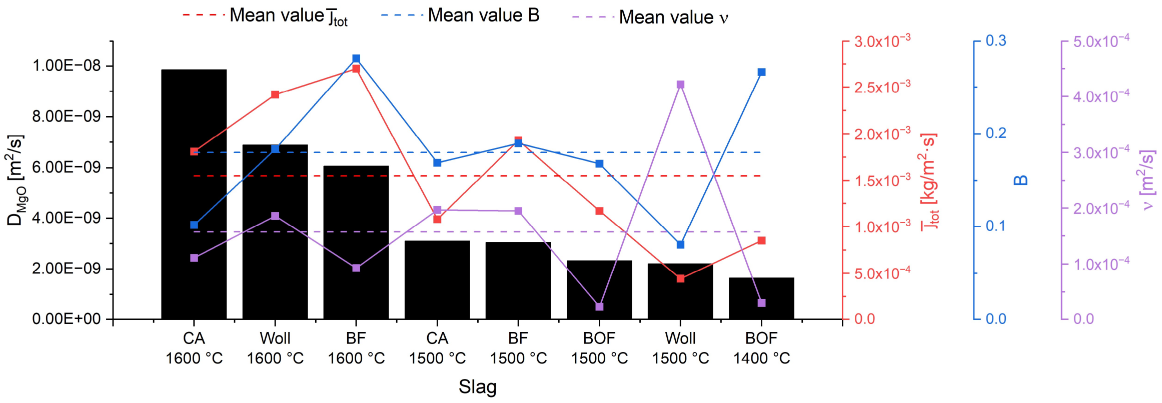

Figure 4-47: Relationship between $D_{eff,MgO}$, $\bar{j}_{tot}$, B and ν

4.6 Experimental procedure KEMS measurements

The vaporization studies using KEMS were carried out at the Forschungszentrum Jülich GmbH using a Finnigan MAT 271 (Finnigan MAT, Bremen, Germany) 90 ° magnetic sector-field mass spectrometer. An iridium cell was used to prevent any reaction between the cell and the sample. The selection of the cell material is of great importance. Because any reaction of the sample material with the cell material would lower the activity of the starting oxide and thus would reduce the partial pressures of the gaseous products. The orifice in the lid of the cell had a diameter of 0.3 mm. The cell was inserted into a molybdenum container which had an opening at the bottom for temperature measurement with an optical pyrometer. The geometry of this cavity has such properties that the emitted light approximates the behavior of a black body. During the measurements, to avoid high radiation losses, the Knudsen cell was thermally isolated by radiation shields made of tantalum. The cell was heated by radiation and electron bombardment from a hot tungsten wire. Temperature was controlled with a type K thermocouple and measured with an Impac IGA 12 optical pyrometer. A sight hole aimed at the black body hole in the molybdenum container is used to measure the temperature. Eventual discrepancies between the measured temperature by the pyrometer in the cavity and the actual temperature in the cell are corrected by measurement standards with well-known melting points. Because only one Knudsen cell can be loaded at a time, the orientation may change when samples are exchanged. Therefore, there may be slight variations in thermal conditions depending on the placement of the Knudsen cell, the mounting of the heat shield, or the positioning of the Knudsen cell, which would have a small but significant effect on the derived thermodynamic quantities. Thus, a systematic error of ±5 K is estimated. Ions were detected by a continuous dynode multiplier in combination with an ion counter. The ionization of the species in the vapor phase was obtained by applying an electron energy of 16 or 70 eV and an emission current of 0.2 mA. Accelerating voltage of the ions was 8 kV. A pure nickel standard was used for evaporation experiments to validate an existing calibration of the optical pyrometer and to determine the sensitivity factor k of the instrument. This involved recording the change in vapor pressure of Ni over a temperature range of approximately 1650 to 1800 K. For the calibration measurements, an electron energy of 16 eV was used. The obtained values perfectly matched the existing calibration. [82]

4.6.1 Pure CaO and MgO

Approximately 50 mg of the pure oxide powders was loaded into the iridium Knudsen cell for the measurements. The initial weights and the masses of the samples determined by differential weighing after the experiments are shown in Table 4-XIV.

Table 4-XIV: Initial sample masses and sample masses after the experiment

Oxide	**Electron energy [eV]**	**Initial mass [mg]**	**After experiment [mg]**
CaO	70	54.13	51.82
	16/70	49.51	46.83
	16	53.93	52.62
MgO	70	53.67	49.67
	16/70	51.58	45.04
	16	50.01	47.86

After weighing the powdered samples into the cell, it was closed and placed in the Knudsen cell chamber. Then the chamber was sealed and evacuated. Heating was started as soon as the pressure decreased below 10^{-5} mbar. The cell was heated to approximately 500 °C by radiation. By reaching this temperature, the heating system automatically switched to electron bombardment heating. Mass scans from mass 10 to 100 at various increasing temperatures were performed to check the presence of possible species in the vapor phase. To optimize the observed signal, the cell position was adjusted as soon as a sufficiently high signal of $^{40}Ca^+$ or $^{24}Mg^+$ ions was detected. These mass scans detected $^{40}Ca^+$, $^{16}O^+$ and $^{16}O_2^+$ as the main ions for CaO and $^{24}Mg^+$, $^{16}O^+$ and $^{16}O_2^+$ for MgO. To determine the necessary duration required to reach equilibrium and to verify the stability of the vapor pressures isothermal measurements were performed. Therefore, the CaO sample was kept at an average temperature of 1804±5 °C for 19 hours and the intensities of $^{40}Ca^+$, $^{16}O^+$ and $^{16}O_2^+$ were measured every hour. The MgO sample was kept at an average temperature of 1653±5 °C for 15 hours and the intensities $^{24}Mg^+$, $^{16}O^+$ and $^{16}O_2^+$ were measured hourly. For the isothermal measurements an electron energy of 70 eV was used. The polythermal measurements were done according to a predefined temperature program and with an electron energy of 16 and 70 eV.

According to the state of knowledge in KEMS studies, the ionization efficiency curves at 70 eV are almost constant for all elements. Therefore, measurements of the pure substances with an energy of 70 eV were carried out first. Due to a possible overlapping of the measured intensity signal of the $^{40}Ca^+$ ions and the $^{40}Ar^+$ ions, measurements were also performed at 16 eV. At an energy of 16 eV, based on the consideration of the energy-dependent ionization cross section, there should be no ionization of argon and thus no overlapping of the measured signal. The curves of the ionization cross sections of argon and calcium are shown in Figure 4-48. These were calculated with the program SIGMA [83]. SIGMA is a Fortran code for the calculation of ionization cross sections of atoms from data in the fitting formalism of Bell et al. [84]. Detailed tables of the calculated cross sections were taken by Mann from [85]. The fit is based on linear regression techniques and graphical comparison of the data. [55]

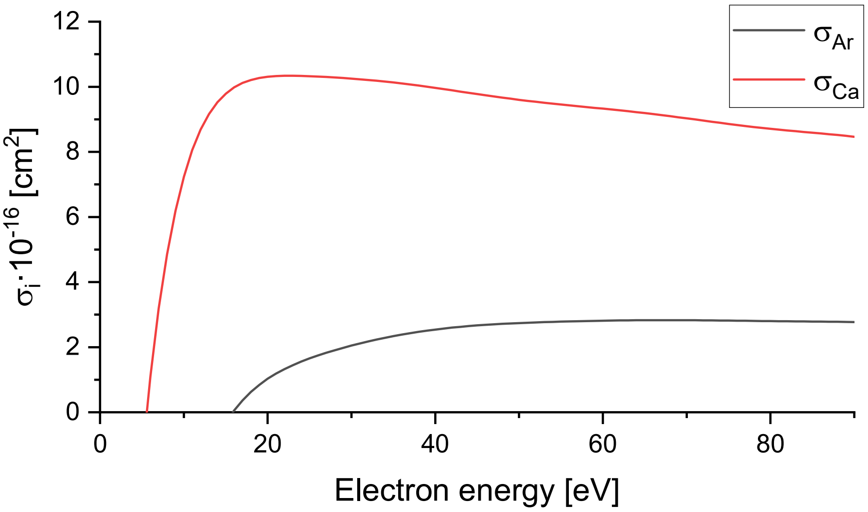

Figure 4-48: Plots of the energy-dependent ionization cross-sections

Each temperature was held for 250 seconds before measuring ion intensity to ensure that equilibrium in the cell had been established. Measurements at each temperature step were taken first with an open and then with a closed shutter. This is necessary to be able to remove the background signal from the actual intensity of the species. The temperature steps between measurements were 10 °C, and the heating and colling rate was 10 °C/min. The temperature range of those measurements were from ~1505 to ~1865 °C for CaO and ~1410 to ~1820 °C for MgO. The polythermal measurements were performed twice to verify the results reproducibility.

4.6.2 Slags

The procedure for the investigations of the different slag types by KEMS was identical to that used for the measurements of the pure substances, except for the stabilization time at the respective measurement temperature. In the first series of tests, an increased Ca and Mg partial pressure was found in the measurements of the cooling period compared to the measurements during the heating period. In combination with the observed high SiO partial pressure, a high evaporation rate of SiO_2 in the form of SiO and thus a rapid change of the slag composition was assumed. To perform polythermal measurements with approximately constant slag composition, the stabilization time at the respective temperatures was therefore reduced to 60 seconds.

4.7 Results KEMS measurements

The following chapters describe the results of the KEMS measurements. These are divided into the calibration measurement, the iso- and polythermal measurement of the pure substances and the polythermal measurement of the slags.

4.7.1 Calibration

The calibration measurements around the melting point of pure Nickel and the comparison of the recorded ion intensity of $^{58}Ni^+$ and the partial pressure of Ni at the melting point (FactPS database), resulted in a pressure calibration factor of $7.6414 \cdot 10^{-9}$. Using the second law method the enthalpy of sublimation ΔH_{sub} of Ni at the mean temperature of the measurements was determined. At a temperature of 1727 K ΔH_{sub} was 422±4 kJ/mol. In Table 4-XV the comparison with data from literature as well as the calculation by FactSage^{TM} 7.3 using the FactPS database is shown. The determined value of ΔH_{sub} is within the ±5 kJ/mol range with literature values, which is commonly acceptable. [55]

Table 4-XV: ΔH_{sub} of pure Ni

Source	$\Delta \boldsymbol{H_{sub}}$ **[kJ/mol]**
This study	422±4
NIST JANAF tables [71]	418±8.4
Alcock et al. [86]	421±5
FactSage^{TM}	417

4.7.2 Measurement of pure CaO and MgO

The investigations of pure CaO as well as MgO are divided into isothermal measurements, to determine the necessary duration for the adjustment of the thermodynamic equilibrium, and polythermal measurements, for the determination of the formation enthalpies of the oxides and subsequently for the determination of the activities of the oxides in the slag systems.

4.7.2.1 Isothermal measurement of pure CaO and MgO

The measured intensities of the respective species were converted into their partial pressures using equation 3-1. σ_i at an electron ionization energy of 70 eV as well as n_i of the different species were taken from [85] and [87], respectively. For the calculation of the cross-section of O_2 equation 4-2 was used, which is valid for the calculation of the cross-section of molecules. Table 4-XVI shows all used values. Because of different calculation approaches, shown in [88]–[90], and experimental determination, as for example in [91], the ionization cross-sections could be a possible source of error. [66],[92]

$$\sigma_{mol} = 0.75 \sum_i \sigma_{at}(i) \tag{4-2}$$

Table 4-XVI: Ionization cross sections and isotopic distribution

Species/Isotope	$\boldsymbol{\sigma_i}$ **[10^{-16} cm^2]**	$\boldsymbol{n_i}$
^{40}Ca	9.0534	0.96941
^{16}O	1.2677	0.99757
$^{16}O_2$	1.9016	0.99515
^{24}Mg	4.6574	0.78990

A rapid setting of the equilibrium state was observed during the isothermal measurements of both CaO and MgO. After only one hour (ignoring the runaways at nine hours) the equilibrium state in the case of CaO. During the measurement of MgO the Mg vapor pressure drops slightly over the first four hours, but stabilizes afterwards, which indicates the reach of the equilibrium state. The results are shown in Figure 4-49. In addition to the experimentally determined partial pressures the calculated ones using FactSage™ 7.3 and the FactPS database are also plotted in the diagram. All possible reaction products were considered in the calculations of the equilibrium partial pressures of all species in the gas phase using FactSage™. The average ratio of $\frac{p_{Ca}}{p_{Ca\,FactSage}}$ is approximately 2, $\frac{p_O}{p_{O\,FactSage}}$ almost 3, and

$\frac{p_{O_2}}{p_{O_2}\ FactSage}$ about 2.5. Values from the first measurement and those from the outliers after nine hours were excluded. These results suggest that the thermodynamic properties of CaO stored in the database used differ from reality. $\frac{p_{Mg}}{p_{Mg}\ FactSage}$, $\frac{p_O}{p_O\ FactSage}$ and $\frac{p_{O_2}}{p_{O_2}\ FactSage}$ show average values of 1, 2.2 and 1.5, respectively, after reaching the equilibrium state. This indicates that the thermodynamic functions for MgO in the databases correspond to the actual measured values.

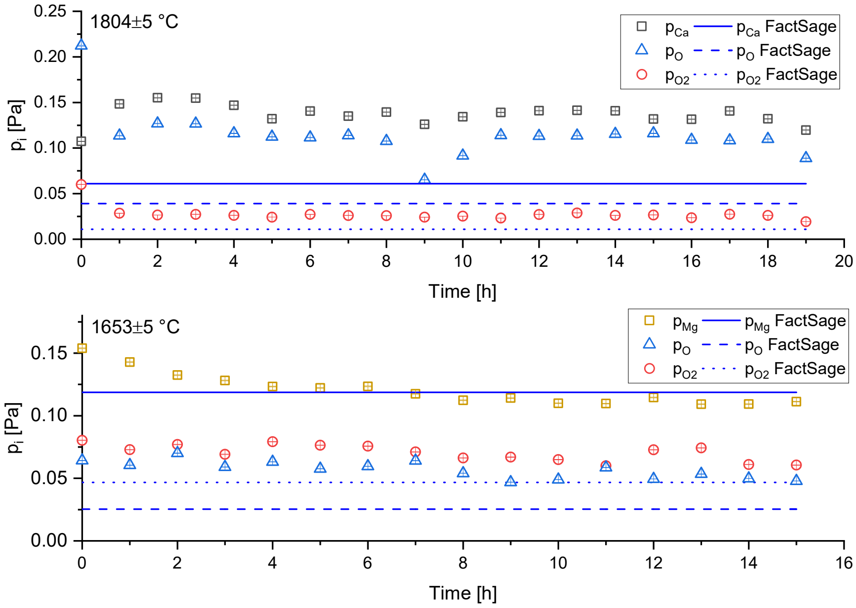

Figure 4-49: Isothermal measurement of CaO and MgO; 70 eV

The presence of oxygen in the residual gas within the KEMS system is a possible source of error in the measurements. Due to the presence of oxygen the measured signal for $^{16}O^+$ and $^{16}O_2^+$ may be affected by errors. In addition, no condensation of oxygen in the molecular beam takes place at the shutter surface. Consequently, this leads to an inaccurate signal for $^{16}O^+$ and $^{16}O_2^+$. Besides the possible inaccuracy of the measurement results due to the presence of residual gas in the system, fragmentation of O_2 may also cause the formation of $^{16}O^+$, which may lead to a deviation of the measured ion intensity. [65]

4.7.2.2 Polythermal measurement of pure CaO and MgO

For the polythermal measurement the measured intensities of $^{40}Ca^+$ and $^{24}Mg^+$ were also converted into partial pressures using equation 3-1 and the parameters from Table 4-XVI. The calculated partial pressures of the respective species are shown as an Arrhenius plot in Figure 4-50 and Figure 4-51. Additionally, partial pressures calculated with FactSage^{TM} 7.3

using the FactPS database are also plotted in the diagrams. Again, all possible gaseous reaction products were taken into account in these calculations.

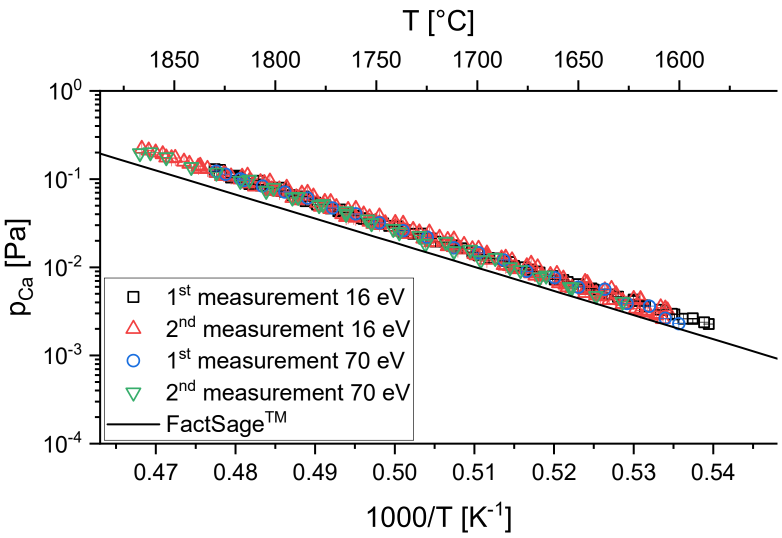

Figure 4-50: Temperature dependence of Ca vapor pressure above pure CaO

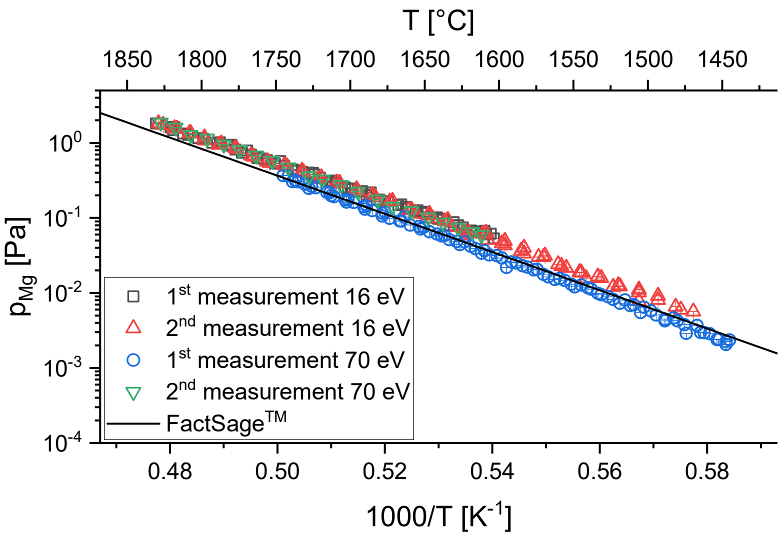

Figure 4-51: Temperature dependence of Mg vapor pressure above pure MgO

As mentioned above, errors in the measurement of $^{16}O^+$ and $^{16}O_2^+$ can occur. To eliminate the influence of these possible errors on further calculations, the partial pressures of O and O_2 are calculated from the Ca and Mg partial pressures, respectively. The required equilibrium constants were determined using FactSage™ and the FactPS database.

Assuming congruent dissociative evaporation of CaO and MgO (equations 4-3 and 4-4) and recombination of atomic oxygen (equation 4-5), reaction equations 4-6 and 4-7 result. Equations 4-8 and 4-9 describe the equilibrium constants for the reactions shown in equation 4-6 and 4-7, respectively. Since these are pure substances, a_{CaO} and a_{MgO} were set to 1. For better comparability with literature data, sublimation enthalpies of Ca and Mg were additionally considered, which results in equations 4-10 and 4-11.

$$CaO(s) \rightleftharpoons Ca(g) + O(g) \tag{4-3}$$

$$MgO(s) \rightleftharpoons Mg(g) + O(g) \tag{4-4}$$

$$2\,O(g) \rightleftharpoons O_2(g) \tag{4-5}$$

$$CaO(s) \rightleftharpoons Ca(g) + 0.5\,O_2(g) \tag{4-6}$$

$$MgO(s) \rightleftharpoons Mg(g) + 0.5\,O_2(g) \tag{4-7}$$

$$K_{CaO} = \frac{1}{p_{Ca} * \sqrt{p_{O_2}}} \tag{4-8}$$

$$K_{MgO} = \frac{1}{p_{Mg} * \sqrt{p_{O_2}}} \tag{4-9}$$

$$CaO(s) \rightleftharpoons Ca(s) + 0.5\,O_2(g) \tag{4-10}$$

$$MgO(s) \rightleftharpoons Mg(s) + 0.5\,O_2(g) \tag{4-11}$$

4.7.2.3 Enthalpy of formation

The standard enthalpies of formation $\Delta_f H^{\circ}_{298}$ were determined by the third law method, the Gibbs energy functions of all species involved were taken from the FactPS database. Table 4-XVII shows a comparison of $\Delta_f H^{\circ}_{298}$ determined in this work with those found in literature.

Table 4-XVII: $\Delta_f H^\circ_{298}$ obtained by 3rd law method in comparison with literature

$\Delta_f H^\circ_{298}$ [kJ/mol]	Source	$\Delta_f H^\circ_{298}$ [kJ/mol]	Source
$Ca(s) + 0.5\ O_2(g) \rightleftharpoons CaO(s)$		$Mg(s) + 0.5\ O_2(g) \rightleftharpoons MgO(s)$	
-624±3	1st measurement 70 eV	-603±4	1st measurement 70 eV
-625±3	2nd measurement 70 eV	-592±4	2nd measurement 70 eV
-624±4	1st measurement 16 eV	-591±4	1st measurement 16 eV
-624±3	2nd measurement 16 eV	-592±4	2nd measurement 16 eV
-624.5±4.0	**mean**	**-597.5±9.6**	**mean**
-602	[74]	-635	[74]
-610	[93]	-572±17	[94]
-634	[95]	-601±1	[71]
-635±1	[71]	-601±1	[96]
-635±1	[97]	-602	[98]
-636	[99]	-602	[95]
-635	FactPS	-601	FactPS

Considering the statistical scatter of the experimental results, standard deviations of the determined values for $\Delta_f H^\circ_{298}$ result. In the comparison of the standard enthalpies of formation of CaO and MgO determined usig KEMS with available literature values (Table 4-XVII), clear deviations can be observed.

The results of the evaporation experiments were used to modify the FactSage™ 7.3 calculations, considering Ca, O, and O_2 as gaseous products for the evaporation process of CaO. In the calculation of MgO evaporation, Mg, O and O_2 were selected as possible products.

Figure 4-52 and Figure 4-53 show the results of the calculation, using the FactPS database compared with calculations using the determined $\Delta_f H^\circ_{298,CaO}$ and $\Delta_f H^\circ_{298,MgO}$. The pressure ranges result from the deviations of the enthalpies of formation. These calculations were also carried out using FactSage™ 7.3.

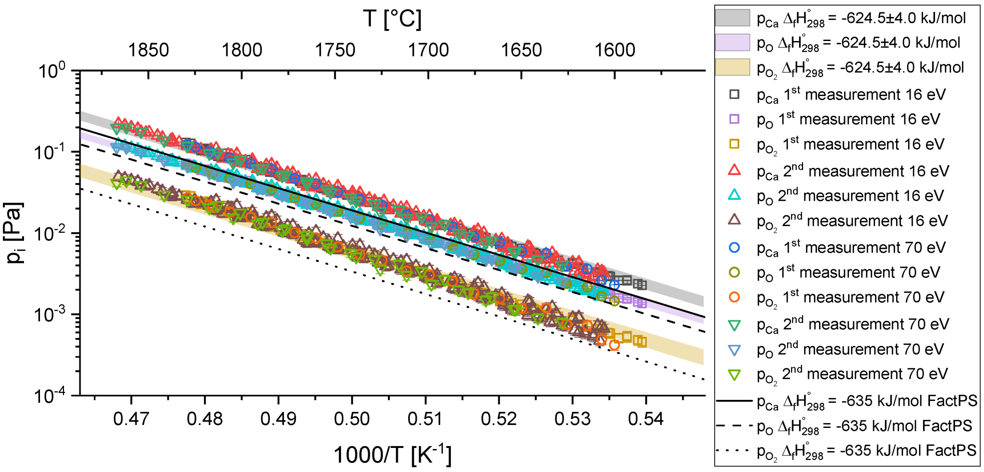

Figure 4-52: Vapor pressures of gaseous species calculated with determined $\Delta_f H^\circ_{298,CaO}$

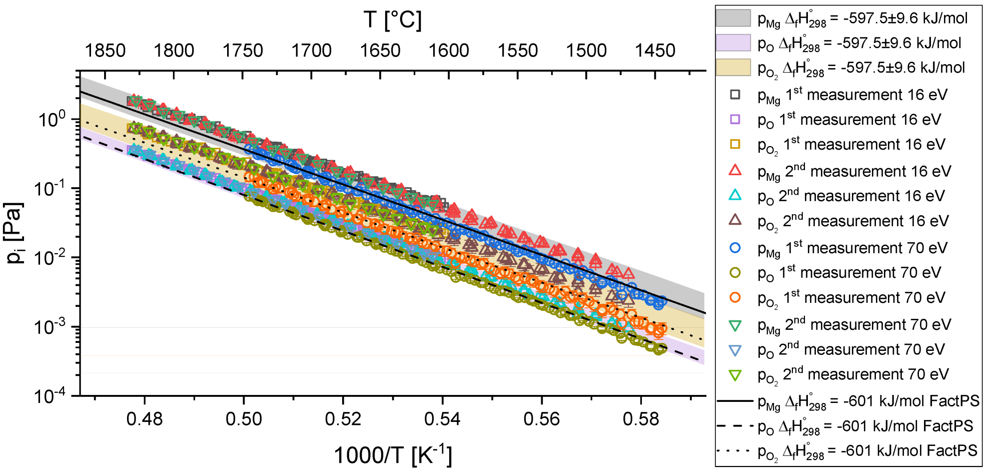

Figure 4-53: Vapor pressures of gaseous species calculated with determined $\Delta_f H^\circ_{298,MgO}$

4.7.3 Polythermal measurement of slags

Similar to the polythermal measurements of the pure substances, the measured ion intensities of calcium, magnesium and, in most cases, oxygen were converted into partial pressures using equation 3-1 and the parameters from Table 4-XVI. The maximum intensity of the oxygen ions was on average 4.5 times higher in the measurements of the different slag systems than in the measurements of pure CaO. Therefore, it can be assumed that, except for the CA slag and the BOF slag, the calculated oxygen partial pressures could be calculated from the ion intensities without significant error. Nevertheless, it should be said here that this value may be affected by error. The determined pressures of the respective species from the measurements with 16 eV are shown as an Arrhenius plot in Figure 4-54 to Figure 4-60. In addition, pressures calculated with FactSage^{TM} 7.3 using the FToxid and FactPS database are plotted. In these calculations, all possible gaseous reaction products were again considered.

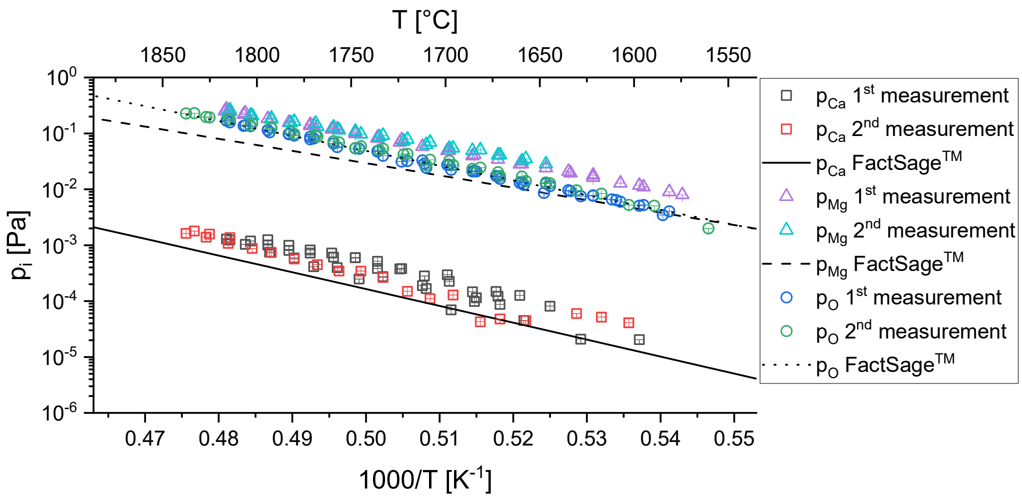

Figure 4-54: Vapor pressures of gaseous species above BF slag

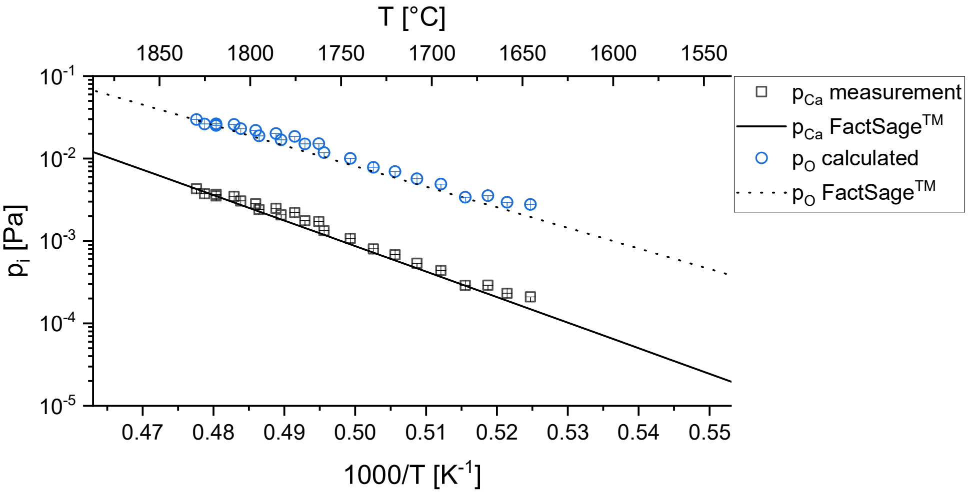

Figure 4-55: Vapor pressures of gaseous species above BOF slag

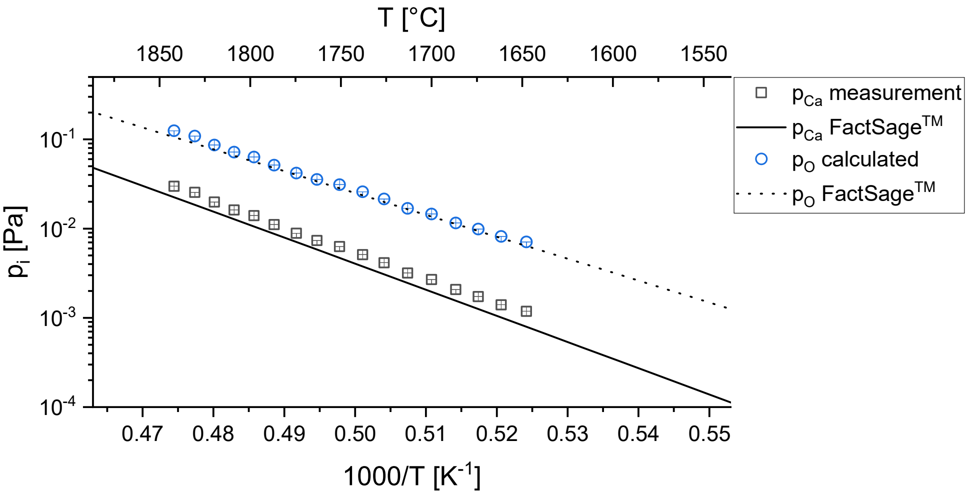

Figure 4-56: Vapor pressures of gaseous species above CA slag

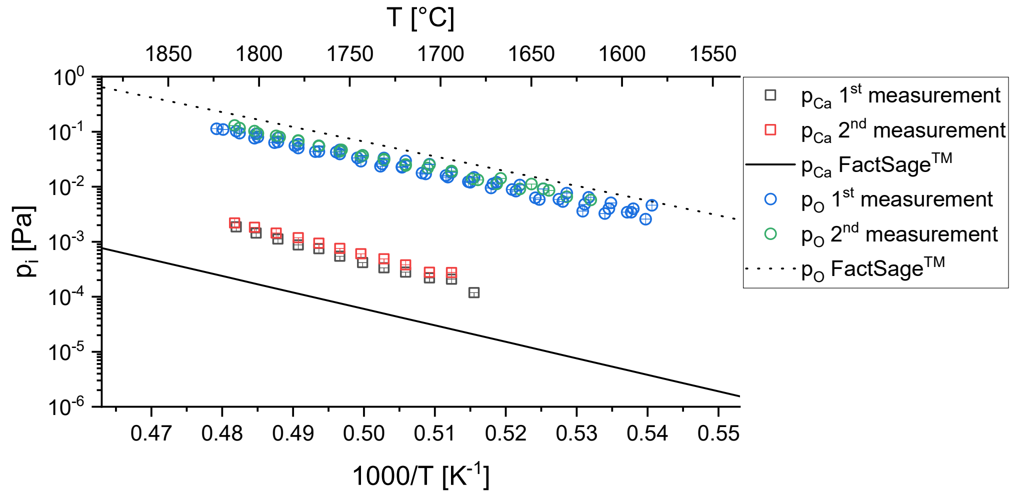

Figure 4-57: Vapor pressures of gaseous species above Woll slag

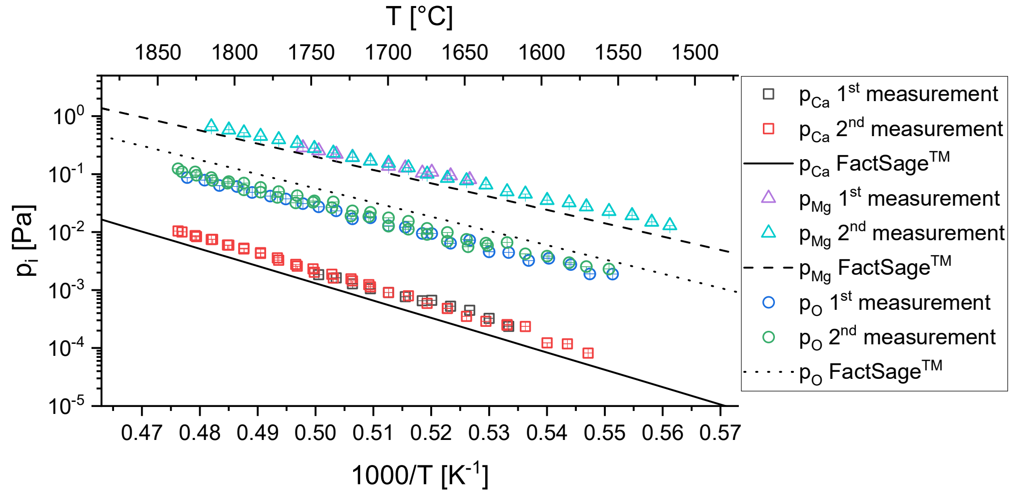

Figure 4-58: Vapor pressures of gaseous species above DS slag

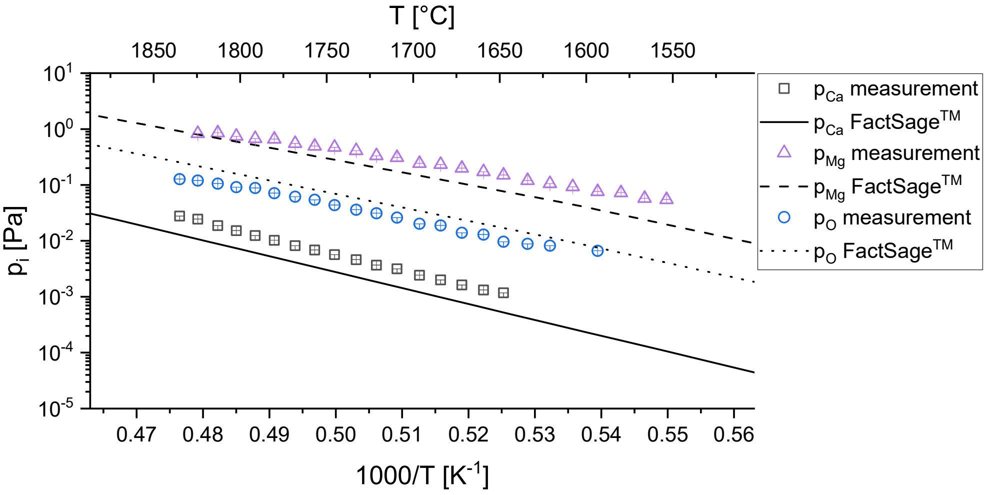

Figure 4-59: Vapor pressures of gaseous species above DS sat. slag

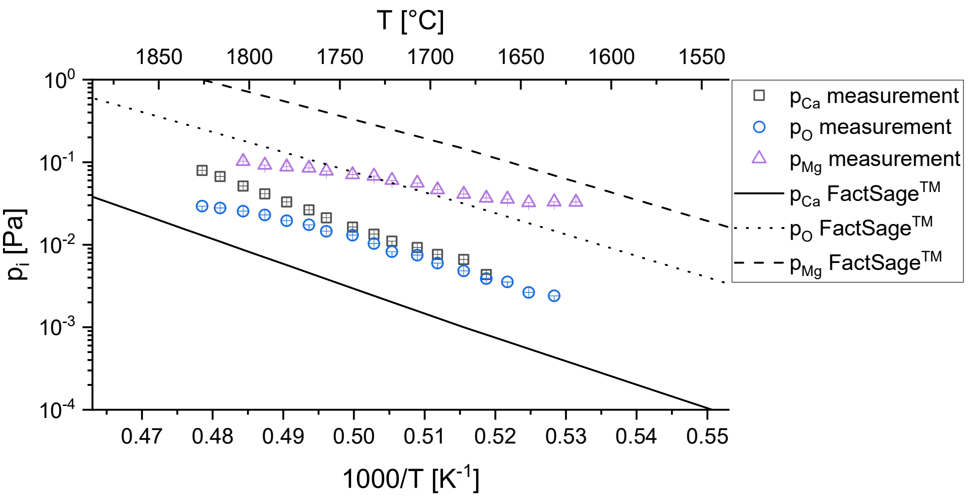

Figure 4-60: Vapor pressures of gaseous species above DS super sat. slag

4.7.4 Activities

As shown in equation 2-9, the activity in the solution is equal to the ratio of the partial pressure of the individual species above the solution and that above the pure substance. Thus, the activities of calcium and magnesium could be determined. The measured activities represent the activity of pure solid CaO or MgO in the respective slag. The partial pressures used for the calculation of the activity were determined for the respective temperature with a fit function. The experimentally determined Ca and Mg activities are shown in Figure 4-61 to Figure 4-63 as a function of temperature and are also compared with the activities calculated by FactSage™ 7.3 using the FToxid and FactPS databases. For the calculation of the activities, the ratio of the CaO partial pressure over the solution and the pure substance was used in the same way as for the experimental determination. Since the Ca activities of the different slags vary significantly in some cases, they have been presented in two diagrams. For the calculation of CaO and MgO activities, the partial pressures of Ca and Mg, respectively, were multiplied with that of O. This procedure is based on the equilibrium between gaseous CaO or MgO and gaseous Ca or Mg and O. The temperature-dependent activities calculated in this way are compared in Figure 4-64 to Figure 4-66 with the activities calculated by FactSage™ 7.3 using the FToxid and FactPS databases. Due to the significant deviations of the measured partial pressures of the individual species during the measurement of the DS super sat. slag from the ideal calculated values, these were not taken into account in the further calculations.

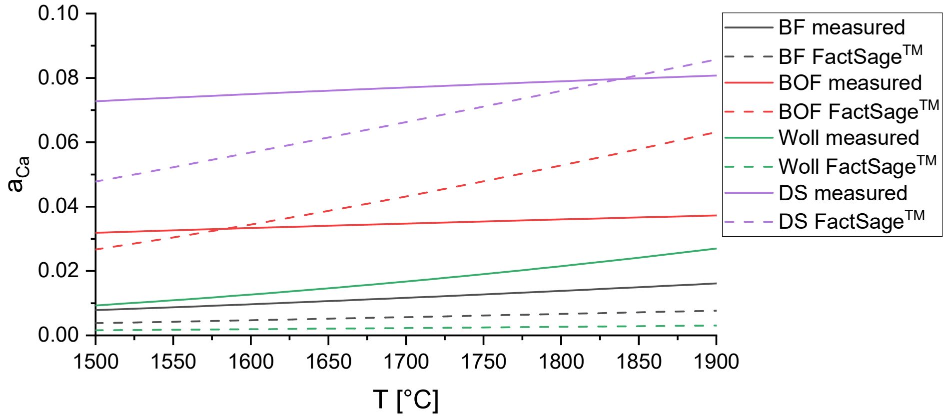

Figure 4-61: a_{Ca} as a function of temperature_1

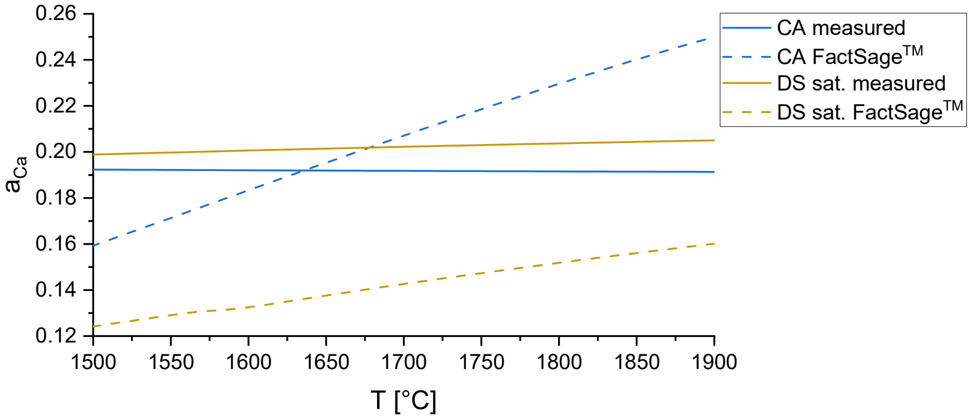

Figure 4-62: a_{Ca} as a function of temperature_2

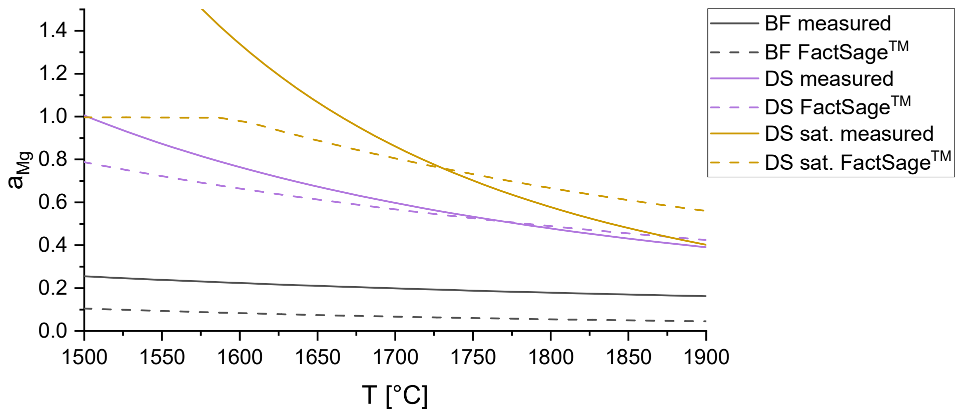

Figure 4-63: a_{Mg} as a function of temperature

Due to the high differences in CaO activity in the different slags, the plot of a_{CaO} as a function of temperature was split into two plots (Figure 4-64 and Figure 4-65), in the same way as for a_{Ca}.

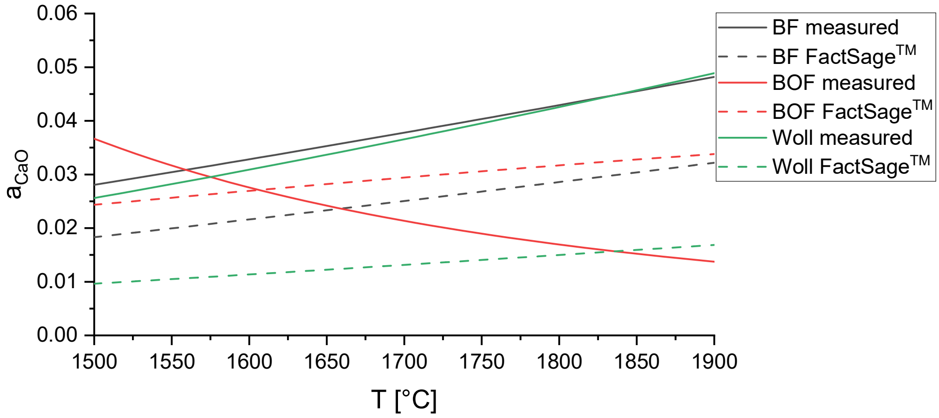

Figure 4-64: a_{CaO} as a function of temperature_1

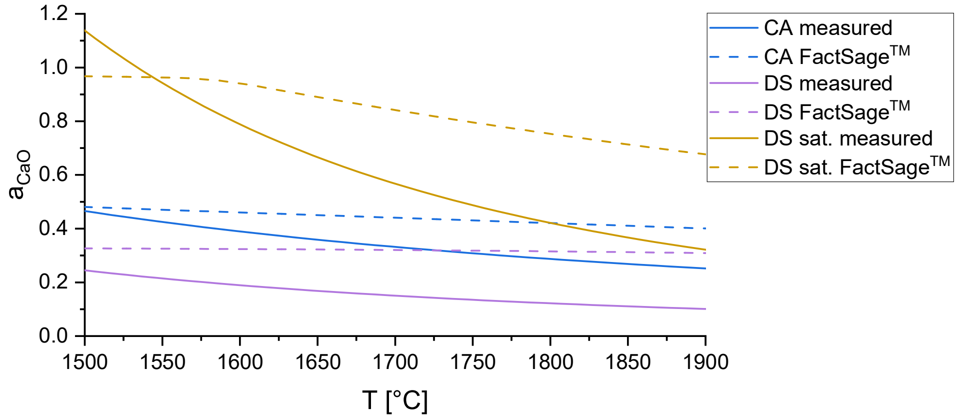

Figure 4-65: a_{CaO} as a function of temperature_2

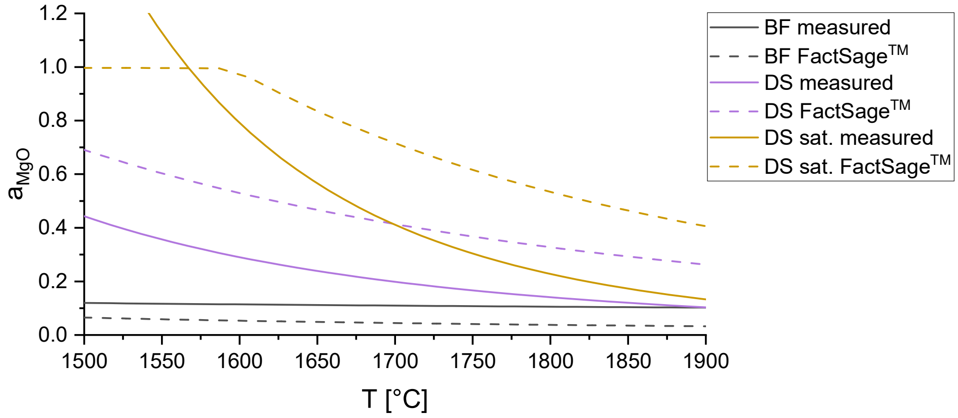

Figure 4-66: a_{MgO} as a function of temperature

To better illustrate the differences between the theoretical activities of CaO and MgO calculated with FactSage™ 7.3 using the FToxid database and those determined experimentally, both values have been plotted in Figure 4-67 to Figure 4-75 in the form of isoactivity lines in the ternary and quaternary systems, respectively, at different temperatures.

The isoactivity lines were calculated using FactSage™ 7.3 by fixing the activities of the respective species to the specific value.

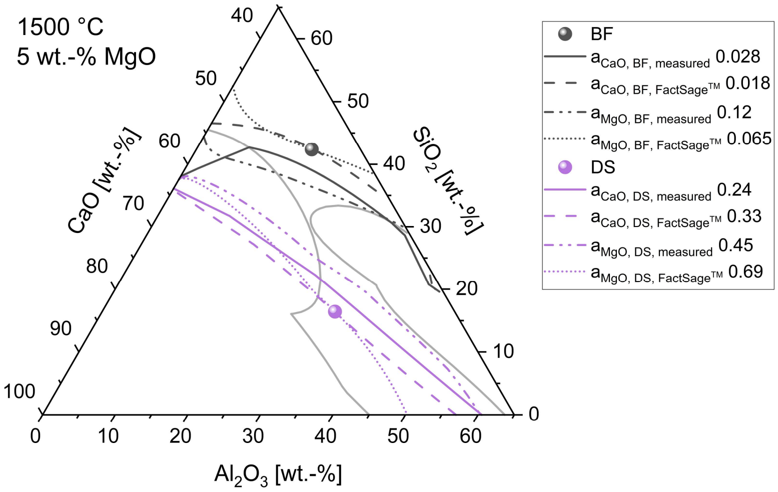

Figure 4-67: CaO and MgO isoactivities in the system CaO-Al_2O_3-SiO_2-MgO; 1500 °C

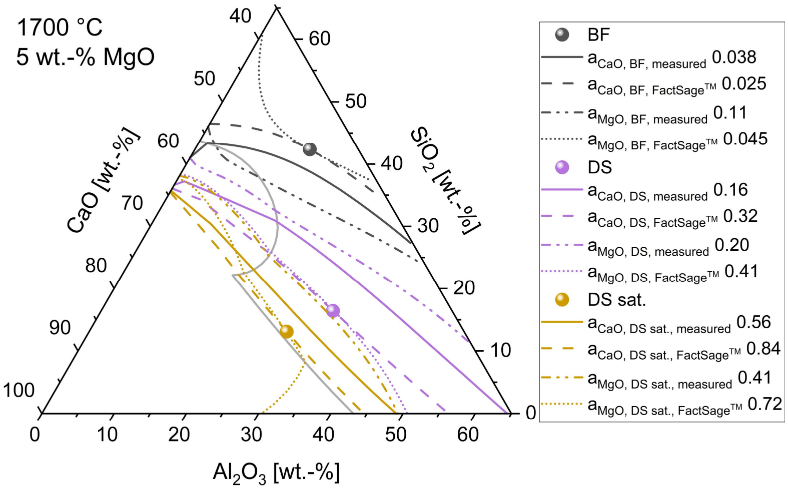

Figure 4-68: CaO and MgO isoactivities in the system CaO-Al_2O_3-SiO_2-MgO; 1700 °C

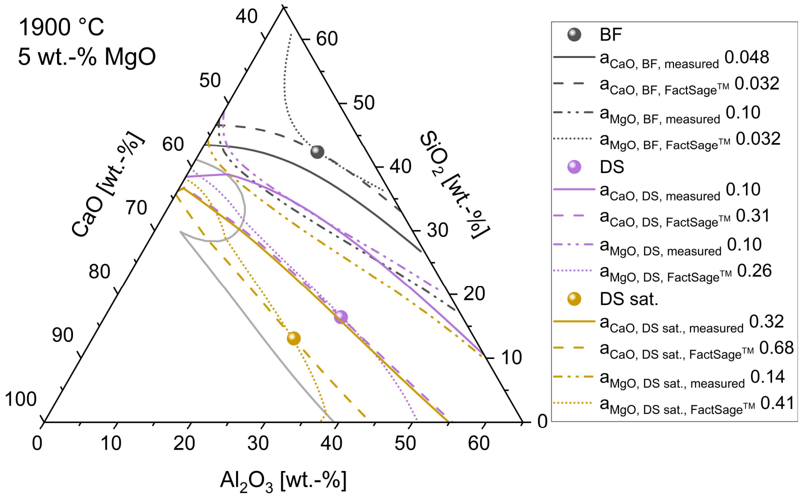

Figure 4-69: CaO and MgO isoactivities in the system CaO-Al_2O_3-SiO_2-MgO; 1900 °C

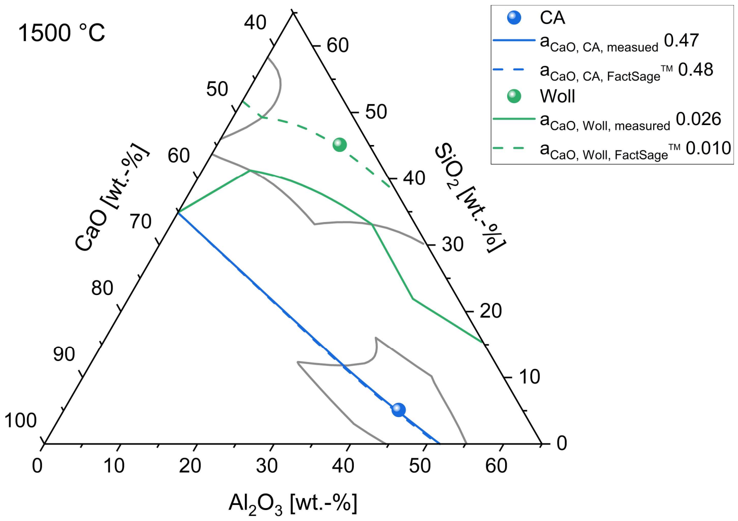

Figure 4-70: CaO isoactivities in the system CaO-Al_2O_3-SiO_2; 1500 °C

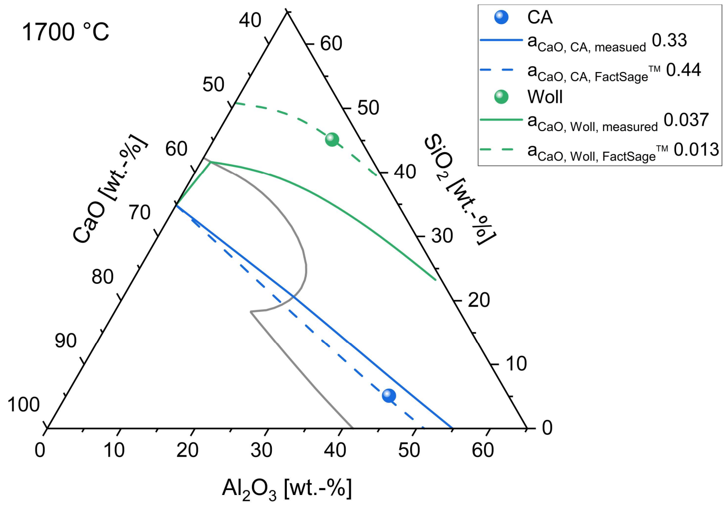

Figure 4-71: CaO isoactivities in the system CaO-Al_2O_3-SiO_2; 1700 °C

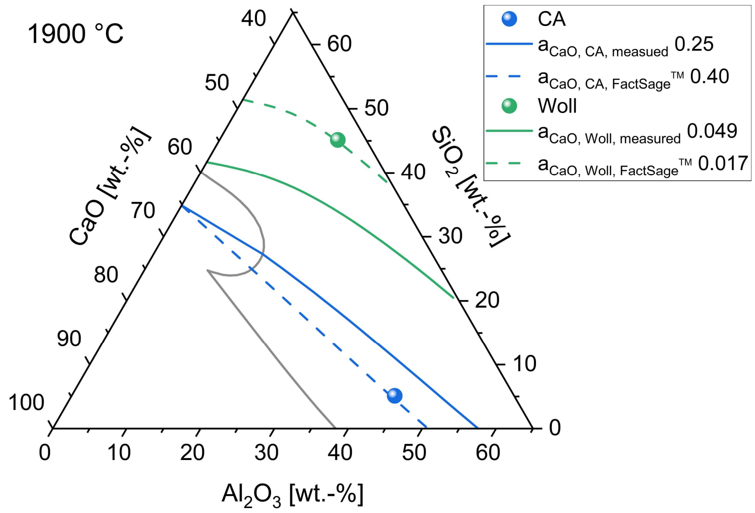

Figure 4-72: CaO isoactivities in the system CaO-Al_2O_3-SiO_2; 1900 °C

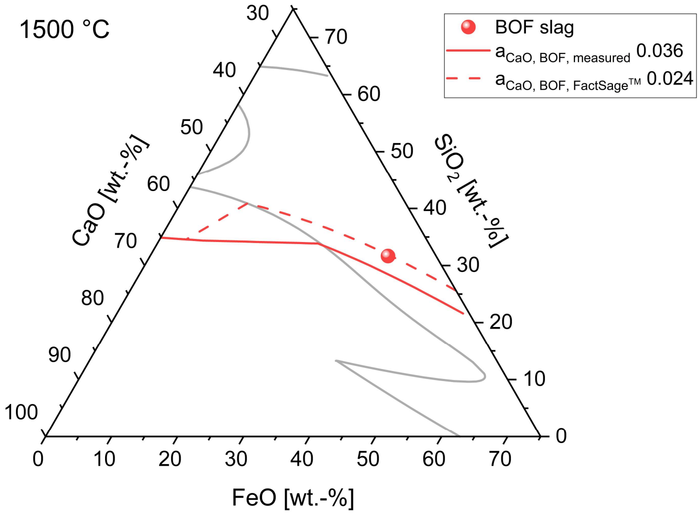

Figure 4-73: CaO isoactivities in the system CaO-FeO-SiO$_2$; 1500 °C

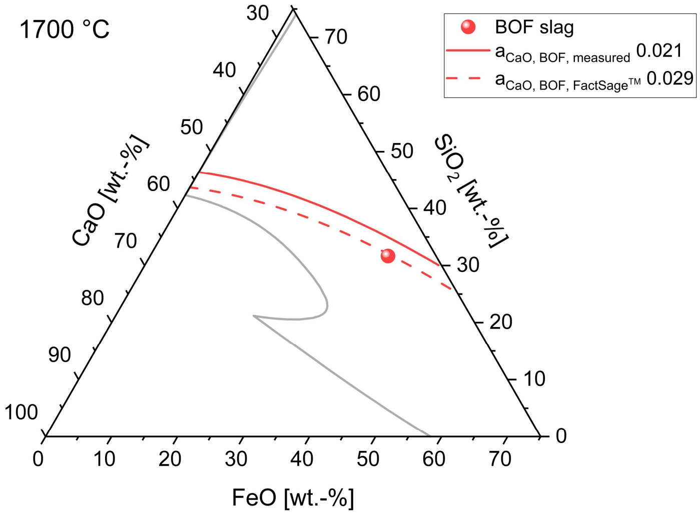

Figure 4-74: CaO isoactivities in the system CaO-FeO-SiO$_2$; 1700 °C

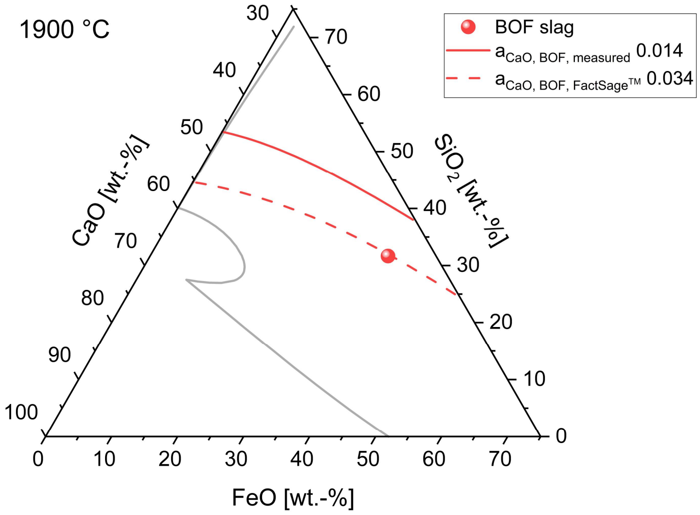

Figure 4-75: CaO isoactivities in the system CaO-FeO-SiO$_2$; 1900 °C

5 Discussion

In the following chapters, the experimental procedure as well as the results of different researchers are described. Those findings, which allow a comparison with the data obtained in this thesis, will be compared in the following.

5.1 Diffusion coefficient

Deng et al. investigated in [100] the dissolution behavior of lime samples which had been prepared in different ways in FeO-SiO_2 and CaO-FeO-SiO_2 slag under static conditions. For this purpose, they immersed lime samples with a square base and an edge length of 10 mm in the slag under argon atmosphere and withdrew them again after a predefined time. The specimens were then quenched in air. In the experiments, they loaded 30 g of pre-melted slag into molybdenum crucibles. The temperature in all their dissolution experiments was 1600 °C. They reported that the dissolution of the CaO specimens in the CaO-FeO-SiO_2 slag was much slower than in the FeO-SiO_2 slag. Deng et al. concluded in [100] that, on the one hand, the higher CaO bulk content in the CaO-FeO-SiO_2 slag results in slower lime dissolution compared with the dissolution experiments in FeO-SiO_2 slag, and, on the other hand, the formation of a dense $2CaO \cdot SiO_2$ layer on the surface of the specimens significantly decreases the dissolution rate. The reason for this is that the dissolution of CaO can then only occur by diffusion through this solid reaction layer. Due to the static conditions in these experiments, a comparison with the results of this work is not possible in this case.

In [101], Deng et al. studied the dissolution behavior of different lime samples under forced convection in CaO-FeO-SiO_2 slag. Therefore, cubes with an edge length of 9 mm were made of the different lime types. These cube-shaped samples were loaded together with 15 g of pre-melted slag into a Mo crucible and heated to 1600 °C under Ar atmosphere. After 10 seconds at test temperature (assumed in the work for complete re-melting of the slag), the slag, together with the lime cube was stirred by a Mo stirrer. After the defined dissolution time, the slag with the lime sample contained was quenched by moving the Mo crucible into the "cooling chamber" of the furnace. During the experiments, they varied the dissolution time as well as the rotation speed of the stirrer. They concluded that the structure of the $2CaO{\cdot}SiO_2$ layer forming on the surface of the test specimens and the associated shear strength of this product layer is crucial for the dissolution rate of CaO in slags. This conclusion is based on the higher dissolution rate of those lime samples with higher porosity and the resulting lower shear strength of the product layer. Thus, the product layer dissolves more easily from the sample surface and the dissolution of CaO into the slag can again take place unhindered. Due to the friction between the crucible and the test specimen, there could have been a corruption of the dissolution rate, therefore these results are not included in a comparison with the data determined in this study.

Amini et al. in [25] and [26] evaluated the influence of slag additives, temperature as well as rotation speed on the dissolution behavior of CaO and MgO in an Al_2O_3-CaO-SiO_2 and CaO-Al_2O_3 slag, respectively, using the rotating cylinder method. Therefore, they immersed cylindrical samples in 60 g of slag at different temperatures and with different rotation speeds. The experiments were performed under atmosphere and the slag was placed in a platinum crucible. After a holding time of one hour at experimental temperature, the specimens were immersed in the slag and rotated. Using a platinum rod, they sampled the slag at periodic intervals and analyzed its composition. From the concentration changes of CaO or MgO in the slag, they calculated the dissolution rates and finally the diffusion coefficients. For the calculation of the diffusivity, they used the equations for mass transfer at the face of the cylindrical samples by Levich from [30] and for the mantle surface by Kosaka and Minowa from [102]. In their investigations of CaO dissolution, they noticed that a solid product layer on the sample surface could be observed only at static tests and a test temperature of 1430 °C. Such a layer could not be observed at higher test temperatures. Neither was it observed in the tests under dynamic conditions. In the MgO dissolution experiments, they could not detect a product layer on the sample surface even in the static experiments at 1450 °C. Amini et al. reported in [25] and [26] that with increasing rotation speed and temperature, respectively, the dissolution rate of both CaO and MgO also increased. Furthermore, they determined that the addition of additives that lower the activation energy of diffusion (e.g., CaF_2, FeO, MnO, TiO_2) increases the diffusivity of CaO and MgO, while the addition of SiO_2 leads to an increase in the activation energy and thus lowers the diffusivity of CaO at least.

In [81], Maroufi et al. investigated the dissolution behavior of CaO in a $CaO-Al_2O_3-SiO_2$ slag in dependence on slag composition, rotation speed and temperature by the rotating cylinder method. For this purpose, they used 60 g of the slag in a platinum crucible and melted it under Ar atmosphere, the lime samples were heated to experimental temperature simultaneously. After holding at test temperature for two hours, the samples were immersed in the slag and then rotated. During the dissolution tests, the slag was sampled at certain intervals using a platinum rod. From the change in chemical composition of the slag as a function of dissolution time, Maroufi et al. in [81] calculated the dissolution rate and diffusion coefficient of CaO using the mass transfer equations of Levich [30] and Kosaka and Minowa [102]. They found that the dissolution rate increases with increasing temperature and rotation speed as well. Furthermore, they reported an increase in the dissolution rate as well as diffusivity of CaO by adding MnO and TiO_2 to the slag, while there was a decrease in the diffusion coefficient with an addition of SiO_2. This was explained by an increase in the M-O bond strength due to the increase in the SiO_2 content of the slag. Since the slower movement of atoms in the environment with stronger M-O bonds leads to lower diffusivity.

Using the rotating cylinder method, Umakoshi et al. investigated the influence of temperature and slag composition on the dissolution behavior of MgO in $CaO-FeO-SiO_2$ slags in [103]. They determined the dissolution rate by measuring the cylindrical samples after the dissolution tests. In the experiments, they used 500 g of pre-melted slag in an iron crucible. The slag as well as the MgO cylinders were heated to the respective experimental temperature under Ar atmosphere. After reaching the temperature, the specimen was rotated and immersed in the slag. After the specified dissolution time, the test specimens were removed from the slag and rotated directly above the crucible at 400 rpm for 1 min to remove adhering slag. The samples were then withdrawn from the furnace and cooled in air. They found that the dissolution rate increases with increasing temperature and rotation speed as well. Furthermore, an increase in dissolution rate was observed with increasing FeO content of the slag. Umakoshi et al. concluded in [103] that MgO dissolution depends on the formation and dissolution of a magnesiowüstite (Mg,Fe)O layer on the sample surface. In this work, the diffusion coefficient of MgO was not calculated, so no comparison is possible.

In [104], Matsushima et al. determined the dissolution rates as well as mass transfer coefficients of CaO in $CaO-SiO_2-Al_2O_3$ and $CaO-FeO-SiO_2$ slags as a function of slag composition, temperature and rotation speed using the rotating cylinder method. For the dissolution experiments, they placed 400 g of pre-melted slag in graphite or iron crucibles. The slag as well as the cylindrical test specimens were heated to the experimental temperature in each case under argon atmosphere. After reaching the temperature, the lime samples were rotated and immersed in the slag. After the specified dissolution time the samples were removed from the slag and rotated above the crucible to remove adhering slag. During this process, the lime samples were slowly cooled in the furnace. The dissolution rate was then determined by measuring the specimens. To calculate the mass transfer coefficient, Matsushima et al. in [104] used diffusion coefficients for calcium from the literature. They concluded that the dissolution rate increases with increasing temperature and rotation speed as well. Furthermore, they concluded from their studies that the formation of a $2CaO \cdot SiO_2$ layer on the sample surface occurs in both CaO-SiO_2-Al_2O_3 and CaO-FeO-SiO_2 slags, and the dissolution of CaO in slags is controlled by the diffusion of Ca through this product layer. However, this product layer could also be an artifact, which means that it may have formed during the cooling of the sample due to the adhering slag. However, they also reported that in the forced convection experiments, the detachment of this product layer occurs and the dissolution of CaO proceeds by the re-formation of such product layer. Diffusion coefficients were not determined in this work, but were used to calculate the mass transfer coefficient, so a comparison is not meaningful.

Hamano et al. in [105] used the rotating cylinder method to investigate the influence of slag composition and rotation speed on the dissolution behavior of CaO in CaO-FeO-SiO_2 slags. They weighed 20 g of the slag into an iron crucible and heated it together with a cylindrical CaO sample to 1300 °C under Ar atmosphere. After complete melting of the slag, they lowered the samples into the heating zone of the furnace and kept them there for at least 5 min. Subsequently, the lime samples were rotated and immersed in the slag for a defined time. After the time had elapsed, the samples were removed from the slag and quenched using argon purging. They determined the dissolution rate by measuring the specimens after the experiments. Hamano et al. found in [105] that the dissolution increases with increasing rotation speed and increasing FeO content of the slag as well. Furthermore, they observed an increase in the dissolution rate with the addition of CaF_2, $CaCl_2$, Al_2O_3 and B_2O_3. The increase in dissolution rate with the addition of Al_2O_3 was only minimal. In this work, the diffusion coefficient of CaO was not calculated, therefore no comparison with data obtained in this work is possible.

Maruoka et al. reported the diffusion coefficients of CaO in two different slags in [106]. In this work, they investigated the dissolution behavior of differently prepared lime samples in FeO-CaO-SiO_2, FeO-CaO-Al_2O_3 and FeO-CaO-B_2O_3 slag at 1400 °C. This was done by melting 100 g of the synthetic slag in iron crucibles under Ar-H_2 atmosphere. After the slag was melted, they introduced an iron tube into the slag to inject Ar and thus obtain a stirring effect. To investigate the influence of the stirring effect, they varied the gas purging rate. The lime samples were preheated for two minutes before being added to slag above the crucible. During the dissolution tests, they took slag samples using Mo wire and analyzed the change in slag composition as a function of time. Using the change in slag composition, they subsequently calculated the dissolution rate. Maruoka et al. observed an increase in dissolution rate with increasing Ar flow rate. Furthermore, they noted the formation of a $2CaO\text{-}SiO_2$ product layer on the surface of the lime specimens in contact with $FeO\text{-}CaO\text{-}SiO_2$ slag and a $3CaO\text{-}Al_2O_3$ layer in contact with $FeO\text{-}CaO\text{-}Al_2O_3$ slag. No product layer was formed in contact with $FeO\text{-}CaO\text{-}B_2O_3$ slag.

In [107], Choi et al. investigated the dissolution behavior of Al_2O_3 in $CaO\text{-}SiO_2\text{-}Al_2O_3$ slags as a function of slag composition, rotation speed and temperature using the rotating cylinder method. They melted 180 g of the synthetic slag in a graphite crucible under argon atmosphere for this purpose. After complete melting of the slag, they immersed an Al_2O_3 rod in the melt and rotated it at a specified rotational speed. After a defined dissolution time, the Al_2O_3 specimen was removed from the slag, cooled in the furnace, and measured. In [107], Choi et al. reported an increase in the dissolution rate with increasing rotation speed or temperature. Furthermore, they noted an increase in dissolution rate with increasing CaO content and with decreasing Al_2O_3 content for a fixed CaO/SiO_2 ratio. They also observed the formation of a $CaO{\cdot}2Al_2O_3$ or $CaO{\cdot}6Al_2O_3$ product layer on the surface of the specimens depending on the slag composition. Choi et al. did not calculate the diffusion coefficient of Al_2O_3, therefore no comparison is possible.

Burhanuddin et al. in [108] and [6] performed dissolution experiments of MgO and Al_2O_3 in $CaO\text{-}Al_2O_3\text{-}SiO_2\text{-}MgO$ slags using the rotating cylinder method. The experiments were carried out with 200 rpm and at 1450, 1500 and 1550 °C, respectively. Therefore, they melted 580 g of the slag in a platinum crucible. During the heating phase and the holding time of one hour at experimental temperature, the samples were placed directly above the crucible. Afterwards, they were rotated and immersed in the slag. The MgO samples were withdrawn from the slag at 1450, 1500, and 1550 °C every 30, 25, and 20 min, respectively, and a laser was used to scan the surface. For the Al_2O_3 samples, the individual time steps were defined as 135, 105, and 90 min, respectively. Using the dissolution profiles and Sherwood relations of Tachibana and Fukui from [32], Guarco et al. from [27], and Levich from [30], they calculated the diffusion coefficients of MgO and Al_2O_3 as a function of dissolution time as well as temperature. They reported that the diffusion coefficient of MgO and Al_2O_3 increases with increasing temperature. At constant temperature, they reported a moderate increase in the MgO diffusion coefficient with dissolution time. Their explanation for this is the decrease in slag viscosity due to the increase in the MgO content of the slag.

In [109], Monaghan and Chen studied the dissolution behavior of Al_2O_3 in CaO-SiO_2-Al_2O_3 slags using LSCM. In their experiments, they varied the slag composition as well as the temperature. From the results, they calculated the diffusion coefficient of Al_2O_3 as a function of slag composition and temperature. They reported an increase in the diffusion coefficient with increasing temperature and decreasing slag viscosity. Furthermore, they pointed out a possible influence of Marangoni flow, which increases the dissolution rate.

The dependence of Al_2O_3 dissolution on slag composition was investigated by Michelic et al. in [15] using HT-LSCM. They used slags in the CaO-Al_2O_3-SiO_2-MgO system at 1600 °C. They determined a decrease in the dissolution rate with increasing slag viscosity. From the results, they were able to calculate the diffusion coefficients of Al_2O_3 in the different slags.

Taira et al. performed experiments on the dissolution behavior of Al_2O_3 in CaO-SiO_2-Al_2O_3 slags by the rotating cylinder method in [110]. In the experiments, they varied the temperature, rotation speed, and slag composition. In the experiments, the amount of slag to achieve a bath height of about 70 mm was placed in a graphite crucible. The slag was melted under argon atmosphere. After reaching the test temperature, the samples were preheated for 5 min above the crucible before being immersed in the slag and set in rotation. After the defined dissolution time, the specimens were removed from the slag and rotated above the crucible for 30 sec to remove the adhering slag. The samples were removed from the furnace afterwards. To remove the remaining slag adhering to the specimens, it was dissolved in dilute hydrochloric acid. Afterwards, the specimens were measured. They reported an increase in the dissolution rate with increasing rotation speed or temperature, also. Furthermore, they noted an increase in dissolution rate with increasing CaO/SiO_2 ratio and by the addition of NaF and CaF_2. They also reported an abrupt increase in dissolution rate in the $CaO/SiO_2 \geq 1$ range, which they attributed to the formation and mechanical separation of $CaO \cdot 6Al_2O_3$ particles. Since the diffusion coefficient was not calculated in the work of Taira et al. no comparison can be made.

Lin et al. investigated the dissolution behavior of SiO_2 in CaO-SiO_2-Fe_2O_3-MgO-MnO slags by the rotating cylinder method in [111]. For the experiments, 140 g of slag was melted in a molybdenum crucible under argon atmosphere, the SiO_2 sample was immersed in the slag after 30 min holding time and rotated. After the dissolution time, the specimens were removed from the furnace and cooled in air. Subsequently, the samples were measured. During the experiments, they varied the rotation speed, slag composition, and experimental temperature. Their results showed an increase in dissolution rate with increasing rotation speed or increasing temperature as well. Furthermore, they observed a decrease in dissolution rate with decreasing basicity of the slag. Their investigations of the sample/slag interface showed no formation of a product layer. The diffusion coefficient of SiO_2 was not calculated in the work of Lin et al. and therefore cannot be compared with the results obtained in this work.

Yu et al. reported in [80] about their dissolution experiments of SiO_2 by the rotating cylinder method in CaO-Fe_2O_3-SiO_2 slags. In the experiments, they melted 300 g of slag under argon atmosphere in an Al_2O_3 crucible. They executed the experiments at different temperatures and different slag compositions. From their results, they concluded that the dissolution rate increases with increasing temperature as well as rotation speed. With increasing SiO_2 content and Fe_2O_3/CaO ratio, they observed a decrease in the dissolution rate. Furthermore, they could not detect any product layer on the sample surface in their investigations. Using the description of the dissolution rate of SiO_2 in slags by Yu et al. from [112] and that of the concentration boundary layer thickness by Levich-Cochran from [30], Yu et al. were able to calculate the diffusion coefficient of SiO_2 in the slags.

Maroufi et al in [81] performed dissolution experiments of SiO_2 in CaO-Al_2O_3-SiO_2-MgO-MnO-K_2O slags under argon atmosphere using the rotating cylinder method. They carried out the experiments at different temperatures, with different rotation speeds and with different slag compositions. In the experiments, they melted 130 g of slag in a molybdenum crucible and placed the SiO_2 sample directly above the crucible during the heating process. They reported an increase in dissolution rate with increasing temperature. At constant temperature, an increase in dissolution rate with increasing rotation speed could be observed from their results. Furthermore, they registered an enhancement in dissolution rate with the addition of CaO and MnO, while a decrease by the addition of SiO_2 and Al_2O_3 was detected. By using the mass transfer relationship of Kosaka et al. from [102] and that of Levich from [30], they were also able to calculate the diffusion coefficient of SiO_2.

In [113], Wang and Sichen analyzed the dissolution behavior of $MgAl_2O_4$ in a CaO-Al_2O_3-MgO-SiO_2 slag using the rotating cylinder method at 1600 °C. They melted 100 g of the slag in a graphite crucible under Ar atmosphere. After sufficient preheating of the specimens, they were immersed in the slag and rotated. After the defined dissolution time the specimens were pulled out of the slag and quenched by argon gas flow. After the furnace had cooled, the ceramic samples were removed from the furnace and their dimensions were measured. In the experiments, they varied the rotation speed. They noted an increase in the dissolution rate with increasing rotation speed. In their experiments, they compared the spinel dissolution results with those of MgO dissolution and observed a higher dissolution rate for the spinel specimens compared to the MgO samples. The researchers attributed this to a greater driving force due to a higher saturation concentration of the slag for $MgAl_2O_4$ compared to MgO.

Monaghan and Chen performed dissolution experiments of spinel particles in $CaO-Al_2O_3-SiO_2$ slag at 1504 °C using LSCM in [114]. They studied the influence of slag composition on the dissolution rate of spherical particles. It was reported that the dissolution rate increased with increasing slag basicity. From the dissolution experiments, they were also able to determine a pseudo-diffusion coefficient, this behaved inversely proportional to the viscosity of the slags. Furthermore, they observed a rotation of the spinel particles in the slag, which affects the dissolution rate.

Hagemann et al. analyzed the dissolution behavior of $MgAl_2O_4$ particles in $CaO-Al_2O_3-SiO_2$ slag at 1550 °C using LSCM in [115]. They used two different slags to investigate the effect of slag composition on dissolution rate. They reported that the increase of Al_2O_3 content of the slag decreased the dissolution rate. Furthermore, they could not detect any reactions at the particle/slag phase boundary.

In [79], Valdez et al. investigated the influence of temperature on the dissolution rate of $MgAl_2O_4$ particles in a $CaO-Al_2O_3-SiO_2$ slag using LSCM. It was concluded that the dissolution rate increased with increasing temperature. Furthermore, they could not observe any product layer on the surface of the spinel particles.

Table 5-I to Table 5-V list the recalculated slag densities and viscosities, together with the viscosity models and diffusion coefficients or dissolution rates used in the case of $MgAl_2O_4$ and the source. It should be mentioned here that the slag viscosities as well as the slag densities of all publications have been recalculated. The reason for this is that in some publications the viscosity and/or slag density was not specified. In the tables, the abbreviations KF and WF stand for the Kalmanovitch-Frank viscosity model and the Watt-Fereday model, respectively.

Table 5-I: Recalculated slag density, viscosity, B and $D_{eff,CaO}$ from literature

T [°C]	ρ_S [kg/m³]	η [Pa·s]	ν [m²/s]	Viscosity model	B	$D_{eff,CaO}$ [m²/s]	Source
1600	2708.69	0.05	$1.96\cdot10^{-5}$	BBHLW	0.24	$3.09\cdot10^{-9}$	[25]
1550	2727.78	0.07	$2.61\cdot10^{-5}$	BBHLW	0.23	$1.93\cdot10^{-9}$	
1500	2747.14	0.10	$3.52\cdot10^{-5}$	BBHLW	0.23	$1.32\cdot10^{-9}$	
1600	2690.37	0.08	$3.00\cdot10^{-5}$	BBHLW	0.34	$2.03\cdot10^{-9}$	
1550	2708.49	0.11	$4.07\cdot10^{-5}$	BBHLW	0.33	$1.51\cdot10^{-9}$	
1500	2726.86	0.15	$5.61\cdot10^{-5}$	BBHLW	0.32	$8.81\cdot10^{-10}$	
1600	2786.43	0.01	$3.46\cdot10^{-6}$	NPL	0.28	$4.63\cdot10^{-9}$	
1550	2806.43	0.01	$4.01\cdot10^{-6}$	NPL	0.27	$4.01\cdot10^{-9}$	
1500	2826.73	0.01	$4.73\cdot10^{-6}$	NPL	0.26	$3.81\cdot10^{-9}$	
1430	2855.65	0.02	$6.16\cdot10^{-6}$	NPL	0.25	$3.81\cdot10^{-9}$	
1600	2724.34	0.01	$3.96\cdot10^{-6}$	WF	0.21	$6.70\cdot10^{-9}$	
1550	2743.68	0.01	$4.66\cdot10^{-6}$	WF	0.20	$4.87\cdot10^{-9}$	
1500	2763.28	0.02	$5.59\cdot10^{-6}$	WF	0.19	$4.22\cdot10^{-9}$	
1430	2791.21	0.02	$7.47\cdot10^{-6}$	WF	0.18	$3.47\cdot10^{-9}$	
1430	2775.02	0.16	$5.69\cdot10^{-5}$	BBHLW	0.23	$9.20\cdot10^{-10}$	[81]
1500	2747.14	0.10	$3.64\cdot10^{-5}$	BBHLW	0.24	$1.32\cdot10^{-9}$	
1550	2727.57	0.07	$2.70\cdot10^{-5}$	BBHLW	0.25	$1.90\cdot10^{-9}$	
1600	2708.28	0.05	$2.03\cdot10^{-5}$	BBHLW	0.26	$3.07\cdot10^{-9}$	
1430	2794.30	0.02	$7.52\cdot10^{-6}$	WF	0.18	$3.54\cdot10^{-9}$	
1500	2766.02	0.02	$5.61\cdot10^{-6}$	WF	0.20	$4.28\cdot10^{-9}$	
1550	2746.17	0.01	$4.67\cdot10^{-6}$	WF	0.20	$5.01\cdot10^{-9}$	
1600	2726.61	0.01	$3.97\cdot10^{-6}$	WF	0.21	$6.82\cdot10^{-9}$	
1500	2725.82	0.16	$5.91\cdot10^{-5}$	BBHLW	0.33	$8.77\cdot10^{-10}$	

1550	2707.34	0.12	$4.28\cdot10^{-5}$	BBHLW	0.34	$1.51\cdot10^{-9}$	
1600	2689.11	0.08	$3.15\cdot10^{-5}$	BBHLW	0.35	$2.02\cdot10^{-9}$	
1400	3110.5	0.17	$5.34\cdot10^{-5}$	NPL	0.80	$2.70\cdot10^{-9}$	[106]
1400	3072.95	0.12	$7.25\cdot10^{-6}$	NPL	0.19	$7.25\cdot10^{-10}$	

Table 5-II: Recalculated slag density, viscosity, B and $D_{eff,MgO}$ from literature

T [°C]	ρ_S [kg/m³]	η [Pa·s]	ν [m²/s]	Viscosity model	B	$D_{eff,MgO}$ [m²/s]	Source
1450	2809.77	0.11	$3.92\cdot10^{-5}$	BBHLW	0.09	$1.92\cdot10^{-8}$	[26]
1500	2785.25	0.08	$2.89\cdot10^{-5}$	BBHLW	0.10	$3.41\cdot10^{-8}$	
1550	2761.15	0.06	$2.17\cdot10^{-5}$	BBHLW	0.12	$3.47\cdot10^{-8}$	
1600	2737.47	0.04	$1.64\cdot10^{-5}$	BBHLW	0.13	$3.85\cdot10^{-8}$	
1450	2906.56	0.08	$2.78\cdot10^{-5}$	BBHLW	0.09	$4.29\cdot10^{-8}$	
1500	2881.03	0.06	$2.08\cdot10^{-5}$	BBHLW	0.10	$4.34\cdot10^{-8}$	
1550	2855.94	0.05	$1.58\cdot10^{-5}$	BBHLW	0.11	$4.74\cdot10^{-8}$	
1600	2831.29	0.03	$1.21\cdot10^{-5}$	BBHLW	0.13	$4.97\cdot10^{-8}$	
1450	2985.09	0.07	$2.20\cdot10^{-5}$	BBHLW	0.09	$4.60\cdot10^{-8}$	
1500	2958.63	0.05	$1.66\cdot10^{-5}$	BBHLW	0.10	$4.57\cdot10^{-8}$	
1550	2932.64	0.04	$1.27\cdot10^{-5}$	BBHLW	0.11	$4.83\cdot10^{-8}$	
1600	2907.10	0.03	$9.84\cdot10^{-6}$	BBHLW	0.13	$5.35\cdot10^{-8}$	
1450	2595.24	1.58	$6.07\cdot10^{-4}$	BBHLW	0.26	$6.24\cdot10^{-11}$	[108]
1450	2595.24	1.58	$6.07\cdot10^{-4}$	BBHLW	0.26	$1.01\cdot10^{-10}$	
1450	2595.24	1.58	$6.07\cdot10^{-4}$	BBHLW	0.26	$1.42\cdot10^{-10}$	
1450	2595.24	1.58	$6.07\cdot10^{-4}$	BBHLW	0.26	$1.00\cdot10^{-10}$	
1450	2595.24	1.58	$6.07\cdot10^{-4}$	BBHLW	0.26	$6.66\cdot10^{-11}$	
1450	2595.24	1.58	$6.07\cdot10^{-4}$	BBHLW	0.26	$1.23\cdot10^{-10}$	
1450	2595.24	1.58	$6.07\cdot10^{-4}$	BBHLW	0.26	$1.08\cdot10^{-10}$	

1450	2595.24	1.58	$6.07 \cdot 10^{-4}$	BBHLW	0.26	$9.65 \cdot 10^{-11}$
1500	2587.12	1.01	$3.92 \cdot 10^{-4}$	BBHLW	0.27	$2.37 \cdot 10^{-10}$
1500	2587.12	1.01	$3.92 \cdot 10^{-4}$	BBHLW	0.27	$2.59 \cdot 10^{-10}$
1500	2587.12	1.01	$3.92 \cdot 10^{-4}$	BBHLW	0.27	$3.74 \cdot 10^{-10}$
1500	2587.12	1.01	$3.92 \cdot 10^{-4}$	BBHLW	0.27	$2.27 \cdot 10^{-10}$
1500	2587.12	1.01	$3.92 \cdot 10^{-4}$	BBHLW	0.27	$2.65 \cdot 10^{-10}$
1500	2587.12	1.01	$3.92 \cdot 10^{-4}$	BBHLW	0.27	$2.46 \cdot 10^{-10}$
1500	2587.12	1.01	$3.92 \cdot 10^{-4}$	BBHLW	0.27	$2.48 \cdot 10^{-10}$
1550	2579.05	0.67	$2.58 \cdot 10^{-4}$	BBHLW	0.27	$4.29 \cdot 10^{-10}$
1550	2579.05	0.67	$2.58 \cdot 10^{-4}$	BBHLW	0.27	$4.69 \cdot 10^{-10}$
1550	2579.05	0.67	$2.58 \cdot 10^{-4}$	BBHLW	0.27	$4.80 \cdot 10^{-10}$
1550	2579.05	0.67	$2.58 \cdot 10^{-4}$	BBHLW	0.27	$4.73 \cdot 10^{-10}$

Table 5-III: Recalculated slag density, viscosity, B and D_{eff,Al_2O_3} from literature

T [°C]	ρ_S [kg/m^3]	η [Pa·s]	ν [m^2/s]	**Viscosity model**	B	D_{eff,Al_2O_3} [m^2/s]	**Source**
1504	2472.75	22.63	$9.15 \cdot 10^{-3}$	WF	0.25	$1.90 \cdot 10^{-11}$	[109]
1550	2464.33	14.54	$5.90 \cdot 10^{-3}$	WF	0.32	$1.46 \cdot 10^{-11}$	
1577	2459.42	11.44	$4.65 \cdot 10^{-3}$	WF	0.38	$1.10 \cdot 10^{-10}$	
1477	2561.66	2.93	$1.14 \cdot 10^{-3}$	WF	0.26	$9.98 \cdot 10^{-11}$	
1477	2561.66	2.93	$1.14 \cdot 10^{-3}$	WF	0.26	$1.50 \cdot 10^{-10}$	
1504	2555.56	2.34	$9.16 \cdot 10^{-4}$	WF	0.30	$1.62 \cdot 10^{-10}$	
1504	2555.56	2.34	$9.16 \cdot 10^{-4}$	WF	0.30	$3.09 \cdot 10^{-10}$	
1550	2545.24	1.64	$6.45 \cdot 10^{-4}$	WF	0.37	$1.60 \cdot 10^{-10}$	
1550	2545.24	1.64	$6.45 \cdot 10^{-4}$	WF	0.37	$1.87 \cdot 10^{-10}$	
1450	2595.24	1.58	$6.07 \cdot 10^{-4}$	BBHLW	0.43	$2.80 \cdot 10^{-11}$	[6]
1500	2587.12	1.01	$3.92 \cdot 10^{-4}$	BBHLW	0.51	$4.56 \cdot 10^{-11}$	

1550	2579.05	0.67	$2.58 \cdot 10^{-4}$	BBHLW	0.61	$7.56 \cdot 10^{-11}$	
1600	2619.70	0.22	$8.40 \cdot 10^{-5}$	Iida	0.43	$1.45 \cdot 10^{-10}$	[15]
1600	2659.08	0.36	$1.34 \cdot 10^{-4}$	Iida	0.93	$4.11 \cdot 10^{-12}$	
1600	2673.78	0.22	$8.32 \cdot 10^{-5}$	Iida	1.06	$1.45 \cdot 10^{-9}$	
1600	2713.99	0.12	$4.32 \cdot 10^{-5}$	Iida	1.12	$1.94 \cdot 10^{-9}$	
1600	2585.56	0.18	$7.07 \cdot 10^{-5}$	Iida	0.56	$3.38 \cdot 10^{-9}$	

Table 5-IV: Recalculated slag density, viscosity, B and D_{eff,SiO_2} from literature

T [°C]	ρ_S [kg/m^3]	η [Pa·s]	ν [m^2/s]	**Viscosity model**	B	D_{eff,SiO_2} [m^2/s]	**Source**
1450	2566.89	1.11	$4.32 \cdot 10^{-4}$	BBHLW	0.56	$8.20 \cdot 10^{-11}$	[81]
1500	2557.99	0.73	$2.85 \cdot 10^{-4}$	BBHLW	0.64	$8.40 \cdot 10^{-11}$	
1550	2549.16	0.49	$1.92 \cdot 10^{-4}$	BBHLW	0.74	$1.20 \cdot 10^{-10}$	
1450	2615.32	3.30	$1.26 \cdot 10^{-3}$	WF	0.81	$9.40 \cdot 10^{-12}$	
1500	2602.77	2.12	$8.15 \cdot 10^{-4}$	WF	0.92	$1.90 \cdot 10^{-11}$	
1550	2590.34	1.43	$5.52 \cdot 10^{-4}$	WF	1.06	$4.90 \cdot 10^{-11}$	
1450	2621.12	0.56	$2.13 \cdot 10^{-4}$	BBHLW	0.75	$8.40 \cdot 10^{-11}$	
1500	2612.28	0.38	$1.45 \cdot 10^{-4}$	BBHLW	0.85	$1.10 \cdot 10^{-10}$	
1550	2603.50	0.26	$1.01 \cdot 10^{-4}$	BBHLW	0.96	$1.30 \cdot 10^{-10}$	
1450	2499.59	3.21	$1.28 \cdot 10^{-3}$	BBHLW	0.41	$1.50 \cdot 10^{-11}$	
1500	2492.14	1.99	$7.98 \cdot 10^{-4}$	BBHLW	0.48	$3.90 \cdot 10^{-11}$	
1550	2484.74	1.26	$5.08 \cdot 10^{-4}$	BBHLW	0.55	$6.40 \cdot 10^{-11}$	
1450	2576.32	0.53	$2.05 \cdot 10^{-4}$	NPL	0.59	$7.30 \cdot 10^{-11}$	
1500	2567.37	0.34	$1.33 \cdot 10^{-4}$	NPL	0.66	$9.50 \cdot 10^{-11}$	
1550	2558.48	0.23	$8.84 \cdot 10^{-5}$	NPL	0.74	$1.30 \cdot 10^{-10}$	
1350	3227.09	0.07	$2.14 \cdot 10^{-5}$	NPL	0.83	$6.40 \cdot 10^{-10}$	[80]
1350	3203.35	0.09	$2.67 \cdot 10^{-5}$	NPL	0.78	$5.05 \cdot 10^{-10}$	

1350	3179.57	0.10	$3.22\cdot10^{-5}$	NPL	0.74	$4.73\cdot10^{-10}$	
1350	3154.83	0.12	$3.69\cdot10^{-5}$	NPL	0.69	$4.56\cdot10^{-10}$	
1350	3131.91	0.14	$4.36\cdot10^{-5}$	NPL	0.64	$2.33\cdot10^{-10}$	

Table 5-V: Recalculated slag density, viscosity, B and dr/dt of $MgAl_2O_4$ from literature

T [°C]	ρ_S [kg/m³]	η [Pa·s]	ν [m²/s]	Viscosity model	B	dr/dt [m/s]	Source
1600	2814.85	0.17	$5.96\cdot10^{-5}$	KF	1.44	$-2.09\cdot10^{-6}$	[113]
1504	2472.56	22.72	$9.19\cdot10^{-3}$	WF	1.33	$-3.67\cdot10^{-7}$	[114]
1504	2513.92	13.50	$5.37\cdot10^{-3}$	BBHLW	1.16	$-5.68\cdot10^{-7}$	
1504	2555.56	4.07	$1.59\cdot10^{-3}$	BBHLW	1.02	$-8.29\cdot10^{-7}$	
1550	2603.22	0.23	$8.72\cdot10^{-5}$	Iida	0.78	$-2.50\cdot10^{-6}$	[115]
1550	2624.93	0.83	$3.16\cdot10^{-4}$	BBHLW	1.17	$-1.62\cdot10^{-6}$	
1470	2597.30	1.79	$6.90\cdot10^{-4}$	BBHLW	0.78	$-5.66\cdot10^{-7}$	[79]
1500	2590.68	1.36	$5.27\cdot10^{-4}$	BBHLW	0.84	$-5.54\cdot10^{-7}$	
1530	2584.08	0.88	$3.42\cdot10^{-4}$	BBHLW	0.92	$-9.74\cdot10^{-7}$	

Table 5-VI to Table 5-X show the correlation matrices between the diffusion coefficients of CaO, MgO, Al_2O_3, SiO_2 and the dissolution rate of the $MgAl_2O_4$ specimens determined in this study and literature values and the parameters T, ν, $1/\nu$ und B.

Table 5-VI: Correlation matrix of $D_{eff,CaO}$ determined in this study and literature values

	T	ν	$1/\nu$	B	$D_{eff,CaO}$
T	1.00				
ν	0.01	1.00			
$1/\nu$	0.09	-0.50	1.00		
B	-0.08	0.57	-0.48	1.00	
$D_{eff,CaO}$	0.41	0.26	-0.06	0.14	1.00

Table 5-VII: Correlation matrix of $D_{eff,MgO}$ determined in this study and literature values

	T	ν	$1/\nu$	B	$D_{eff,MgO}$
T	1.00				
ν	-0.49	1.00			
$1/\nu$	0.37	-0.75	1.00		
B	-0.18	0.81	-0.73	1.00	
$D_{eff,MgO}$	0.32	-0.73	0.92	-0.81	1.00

Table 5-VIII: Correlation matrix of D_{eff,Al_2O_3} determined in this study and literature values

	T	ν	$1/\nu$	B	D_{eff,Al_2O_3}
T	1.00				
ν	-0.18	1.00			
$1/\nu$	0.69	-0.44	1.00		
B	0.64	-0.44	0.79	1.00	
D_{eff,Al_2O_3}	0.50	-0.27	0.74	0.45	1.00

Table 5-IX: Correlation matrix of D_{eff,SiO_2} determined in this study and literature values

	T	ν	$1/\nu$	B	D_{eff,SiO_2}
T	1.00				
ν	0.22	1.00			
$1/\nu$	-0.76	-0.59	1.00		
B	0.10	-0.21	0.18	1.00	
D_{eff,SiO_2}	-0.69	-0.61	0.96	0.13	1.00

Table 5-X: Correlation matrix of $dr/dt_{MgAl_2O_4}$ determined in this study and literature values

	$\boldsymbol{T}$	$\boldsymbol{\nu}$	$\boldsymbol{1/\nu}$	$\boldsymbol{B}$	$\boldsymbol{-dr/dt_{MgAl_2O_4}}$
$\boldsymbol{T}$	1.00				
$\boldsymbol{\nu}$	-0.39	1.00			
$\boldsymbol{1/\nu}$	0.87	-0.49	1.00		
$\boldsymbol{B}$	-0.38	0.91	-0.51	1.00	
$\boldsymbol{-dr/dt_{MgAl_2O_4}}$	0.72	-0.47	0.77	-0.52	1.00

A comparison between the actual signs of the parameter correlations, shown in Table 4-XIII, results in an error order of 6 for Table 5-VI, 4 for Table 5-VII and Table 5-X, 3 for Table 5-IX and 0 for Table 5-VIII. The maximum error order is again 10. This shows that such an analysis would only be meaningful for the data from Table 5-VIII. The diffusion coefficients of MgO, Al_2O_3 and SiO_2 as well as the dissolution rate of $MgAl_2O_4$ show the highest correlation with the parameter $1/\nu$. Figure 5-1 to Figure 5-5 show the diffusion coefficients and the dissolution rate as a function of $1/\nu$.

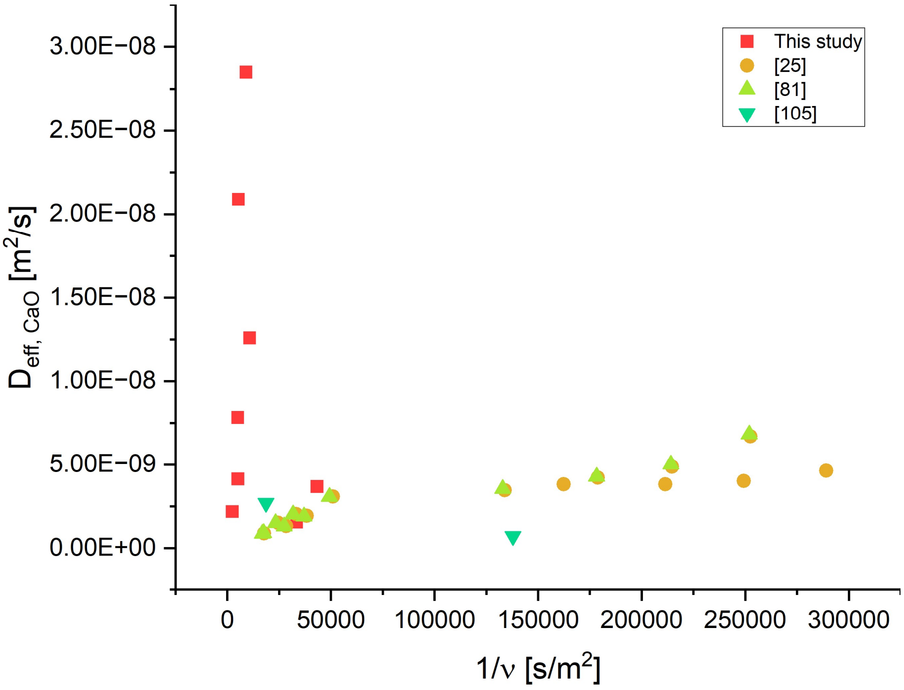

Figure 5-1: $D_{eff,CaO}$ as a function of $1/\nu$

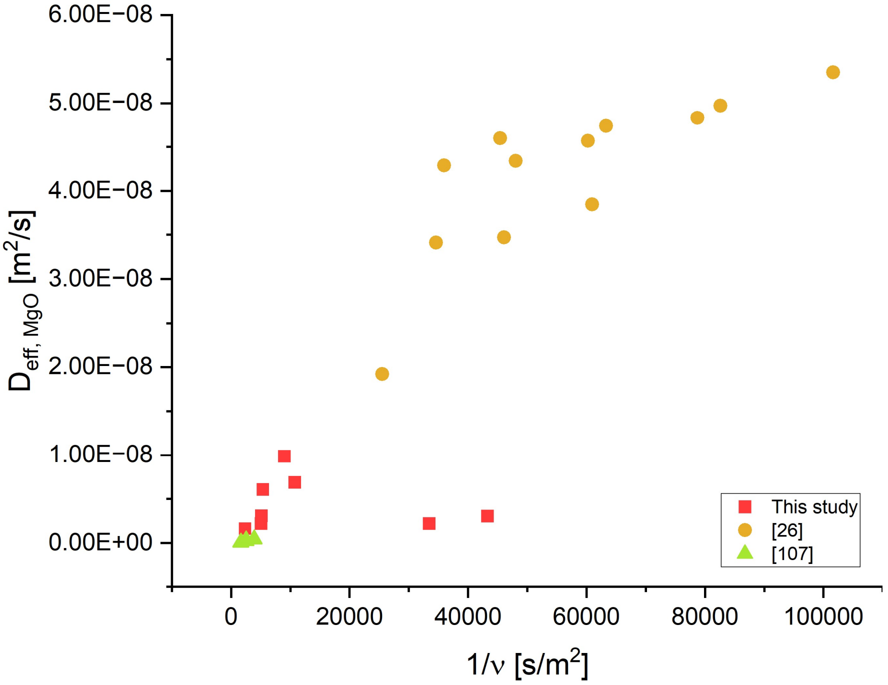

Figure 5-2: $D_{eff,MgO}$ as a function of $1/\nu$

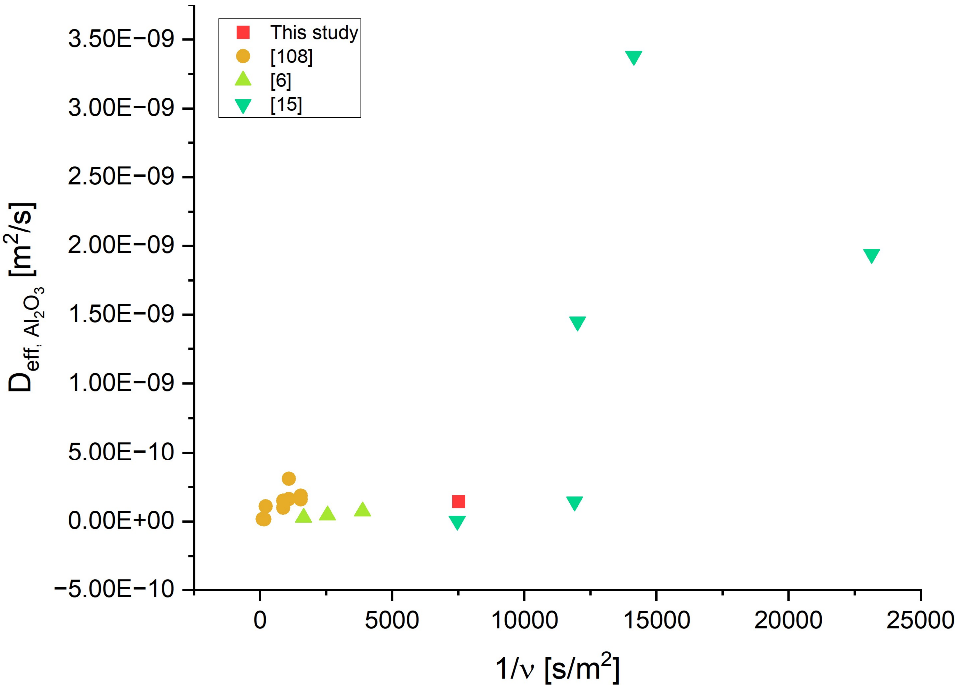

Figure 5-3: D_{eff,Al_2O_3} as a function of $1/\nu$

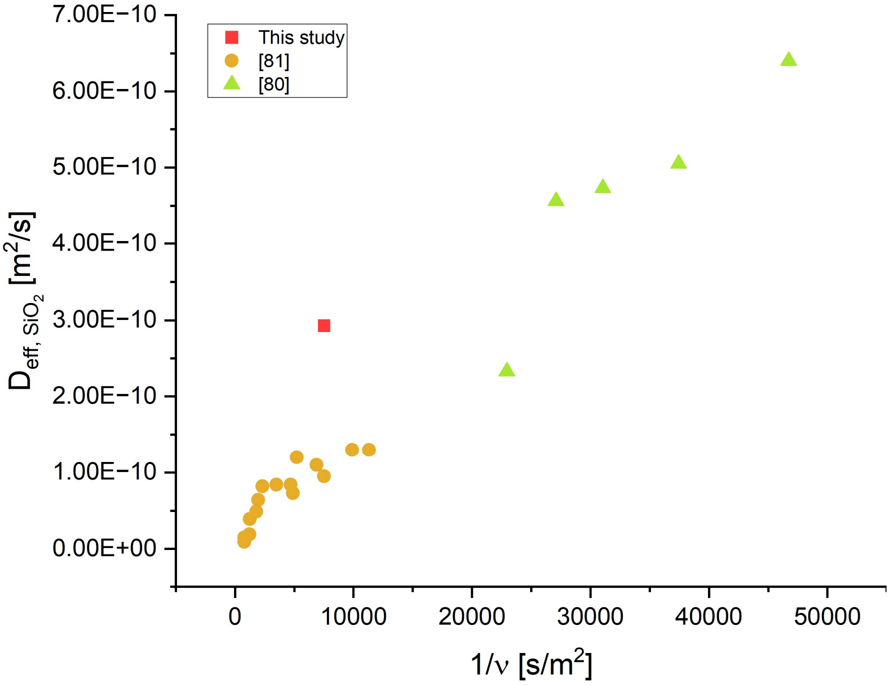

Figure 5-4: D_{eff,SiO_2} as a function of $1/\nu$

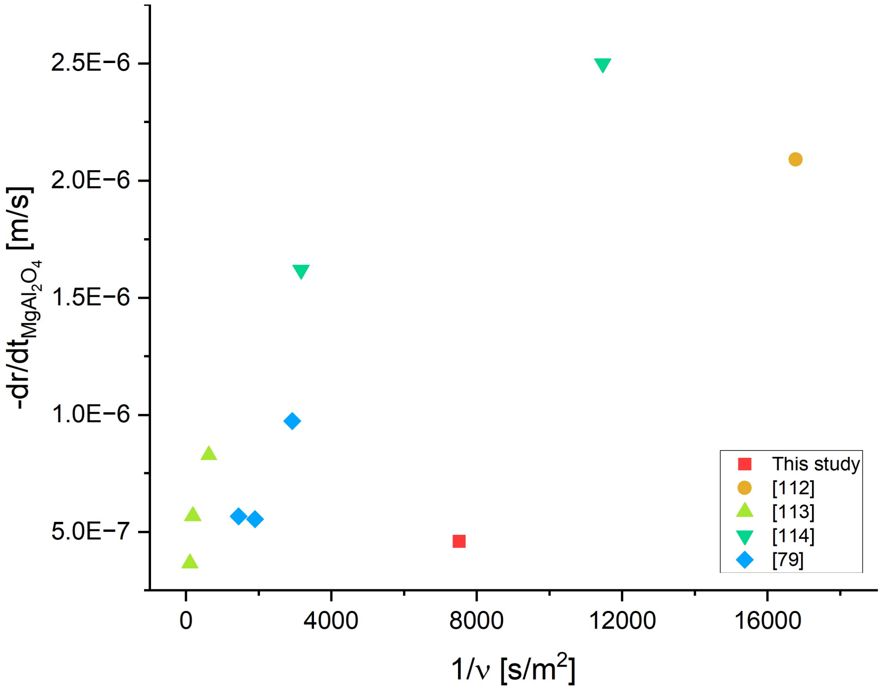

Figure 5-5: $-dr/dt_{MgAl_2O_4}$ as a function of $1/\nu$

Figure 5-4 is that one which most clearly shows the general trend that the diffusion coefficient and the dissolution rate increase with decreasing slag viscosity as it would correspond to the Stokes-Einstein relationship (Equation 4-1). The other diagrams are affected by too high unexplained variance to verify such relation. Again, incorporation of too many different slags and sources may increase the unexplained variance. However, D_{eff,Al_2O_3} in particular shows a considerable deviation from the linear relationship, whereas this is less affected for $D_{eff,MgO}$ and D_{eff,SiO_2} by a few outliers. Figure 5-1 shows an increase in $D_{eff,CaO}$ even at higher slag viscosities. This means that the present data set does not globally satisfy the Stokes-Einstein equation, as too many parameters that affect the diffusion coefficient dominate the influence of the viscosity.

Burhanuddin and Harmuth show in [116] for three selected slags that the proportionality between the effective binary diffusion coefficient of MgO to f/η is greater than to $1/\eta$. f stands for the thermodynamic factor of diffusion and is defined as shown in equation 5-1.

$$f = 1 + \frac{d \ln \gamma_i}{d \ln X_i} \qquad \text{5-1}$$

Here γ_i or X_i stands for the activity coefficient or mole fraction of component i.

The coefficient of determination of a linear correlation of the effective binary diffusion coefficients of CaO with $1/\eta$ in the different slags determined in this work is 0.33, while that with f/η is 0.23. Therefore, this relation is also not justified for the determined data. In this analysis, the values of $D_{eff,CaO}$ in the BOF slag were neglected, as the low viscosity of this slag makes such a correlation impossible. However, the values determined for $D_{eff,CaO}$ show a certain linear correlation with f. The coefficient of determination of the plot of $D_{eff,CaO}$ against f is 0.58. All values determined were included in this analysis. However, it must be noted here that too few data of a slag type are available to find a meaningful correlation between the effective binary diffusion coefficient of CaO and another thermodynamic parameter. The two outliers in Figure 5-2 are the values determined in this study for $D_{eff,MgO}$ in the BOF slag. The reason for the large deviation from the literature values is due to the calculated viscosity. The deviation of the dissolution rate of $MgAl_2O_4$ determined in this work from the literature values, shown in Figure 5-5 is due to the fact that all literature values except those of Wang and Sichen from [113] were determined using LSCM. The comparison shows that the dissolution rate in the dissolution experiments using the rotating finger method is lower than that in the LSCM investigations.

5.2 Enthalpy of formation

The deviations between the values of the enthalpies of formation obtained in this work and those of Gourishankar et al. in [74] may be explained by the experimental setup used. In [74] the mass loss rate of CaO single crystals in vacuum at a constant temperature was determined. The experimental temperature in [74] was between ~1560 and ~1800 °C. The researchers assumed that the local equilibrium is maintained by a rapid surface reaction and that mass loss is controlled by gas transport from the near-surface region. In further calculations, only Ca(g), O(g), and O_2(g) species were considered. Under the experimental conditions, all other species were considered negligible. They used the O_2(g)/O(g) equilibrium from the 1985 JANAF tables to solve the Langmuir equation and converted the measured mass-loss rates to the equilibrium constant. They determined a value of -602 kJ/mol for $\Delta_f H^\circ_{298,CaO}$ using the determined equilibrium constants and Gibbs energy functions for CaO(s), Ca(ref), and O_2(g), which were also taken from the 1985 JANAF tables. Gourishankar et al. in [74] explained the high mass loss rates occurring by a lower standard enthalpy of formation compared to the tabulated one. The high mass loss rate could also be explained by a reaction between gaseous products and carbon from the graphite susceptor with the sample to form CO(g).

In [93] Wakasugi et al. determined $\Delta_f H^\circ_{298,CaO}$ by the equilibration of silver and a CaO-saturated slag in a graphite crucible under argon atmosphere with 10% CO. In the experiments, the temperature ranged from ~1300 to ~1560 °C. They first measured the activity coefficient of Ca in Ag by equilibration of a CaC_2-saturated slag with Ag in a graphite crucible in an Ar atmosphere in a temperature range between ~1140 and ~1560 °C to determine $\Delta_f H^\circ_{298,CaO}$. Using the obtained activity coefficient, Wakasugi et al. in [93] could determine the free energy of formation function, which is used to calculate the standard enthalpy of formation. Considering the possible variables affecting the accuracy of the results in this work, such as exact gas composition, possible reactions of slag or gas phase with crucible material, and the precision of the measurement of the calcium content in silver, these results are questionable.

By critically reviewing the literature Liang et al. in [95] modeled thermodynamic functions for crystalline CaO. The modeling by Liang et al. in [95] is based in part on the specific heat capacity function for CaO from the SGTE pure substance database and the calorimetric work tabulated in the NIST-JANAF tables [71], which have been studied in more detail. Considering that the accuracy of the measurements from 1952 and 1956 can be questioned, the deviation from the values modeled by Liang et al. in [95] could be related to the accuracy of the values in the NIST-JANAF tables [71].

In the NIST-JANAF tables [71] the value for $\Delta_f H^\circ_{298,CaO}$ is based on only two experimental measurements. One of them was performed by Huber and Holley in [97] using bomb calorimetry to determine the enthalpy of combustion of Ca, and the second was performed by Rossini et al. in [99] using calorimetry with acidic solution. The difference between the two values for $\Delta_f H^\circ_{298,CaO}$ is only 0.07%. It is largely assumed that these values, as well as the value obtained from them, which is tabulated in [71], are correct. The accuracy of the results could be questionable due to the accuracy of the techniques used at the time of publication, as mentioned above.

Gourishankar et al. in [74] performed free evaporation experiments with MgO single crystals as well as sintered polycrystalline MgO specimens in the same way as with CaO, to determine $\Delta_f H^\circ_{298,MgO}$. In this case, the previously mentioned reason of the reaction of gaseous C with the sample surface does not explain the low mass loss rate, which, compared to other literature values and the value determined in this work, leads to a more negative standard enthalpy of formation. It may be a general problem in the measurements leading to the fact that the value for $\Delta_f H^\circ_{298,MgO}$ reported by Gourishankar et al. [74] is also not reliable.

In [94] Altmann performed Knudsen effusion experiments in a temperature range between ~1450 and ~2000 °C to investigate the evaporation behavior of MgO. For the experiments he used alumina cells. To calculate the partial pressure of magnesium, mass loss data obtained from the evaporation experiments were used. With the determined partial pressure $\Delta_f H^\circ_{298,MgO}$ was calculated. Due to spinel formation, the use of alumina cells presents a major problem here, as this changes the partial pressures of the species in the gas phase. Because of the reaction between cell and sample material and the resulting inaccuracy of the vapor pressure results, the values for $\Delta_f H^\circ_{298,MgO}$ given by Altman in [94] are not reliable.

$\Delta_f H^\circ_{298,MgO}$ in the NIST-JANAF tables [71] is based on the values of Holley and Huber in [96], who used bomb calorimetry for the determination of the enthalpy of combustion of metallic Mg, and Shomate and Huffman in [98], who used HCl solution calorimetry. Their determined values differ from each other by only 0.1%. Thermodynamic function modeling by Liang et al. in [95] is also based on these data. Here again, the accuracy of the determined values could be questioned due to the precision of the techniques used at the time of the publications in 1943 and 1951.

5.3 Activities

As already mentioned above, Wen et al. in [42] used a modified slag-metal equilibrium technique to determine the activity of CaO for solid reference state in a CaO-SiO_2-Al_2O_3-MgO slag. For this purpose, they heated a reference slag (C_2S saturated) and the slag to be measured together with tin to 1600 °C under CO atmosphere in a graphite crucible and kept this temperature for 24 hours. Afterwards, they quenched the crucible in oil, separated metal and slag phases, and analyzed both phases by inductively coupled plasma emission spectroscopy. Using the Ca content in the metal phase after the equilibrium experiments, they were able to calculate a_{CaO} of the slag using equation 5-2.

$$a_{CaO} = \frac{x_{Ca} \cdot a_{CaO}^0}{x_{Ca}^0} \tag{5-2}$$

Here, a_{CaO} or a_{CaO}^0 is the CaO activity of the measured slag or the reference slag, and x_{Ca} or x_{Ca}^0 is the Ca content of the metal phase in equilibrium with the measured slag or the reference slag. They determined the activity of the C_2S saturated reference slag using the same procedure, except that here the C_2S saturated slag was the slag to be measured and a CaO saturated slag (a_{CaO}=1) was the reference slag. Wen et al. reported in [42] an increase in a_{CaO} with increasing basicity (B_2) at 1600 °C. Furthermore, they recorded a decrease in CaO activity with increasing Al_2O_3 content of the slag at a basicity of 1.05 and a MgO/Al_2O_3 ratio of 0.35, while an increase was measured at the same MgO/Al_2O_3 ratio and a slag basicity of 1.20. In addition, they found an increase in a_{CaO} with increasing MgO/Al_2O_3 ratio, at a basicity of 1.05 and an Al_2O_3 content of 15 wt.-%. Figure 5-6 shows the results determined by Wen et al. in [42] for slags with an Al_2O_3 content of 15 wt.%. In addition, the isoactivity lines of CaO calculated using FactSage™ 7.3 are shown.

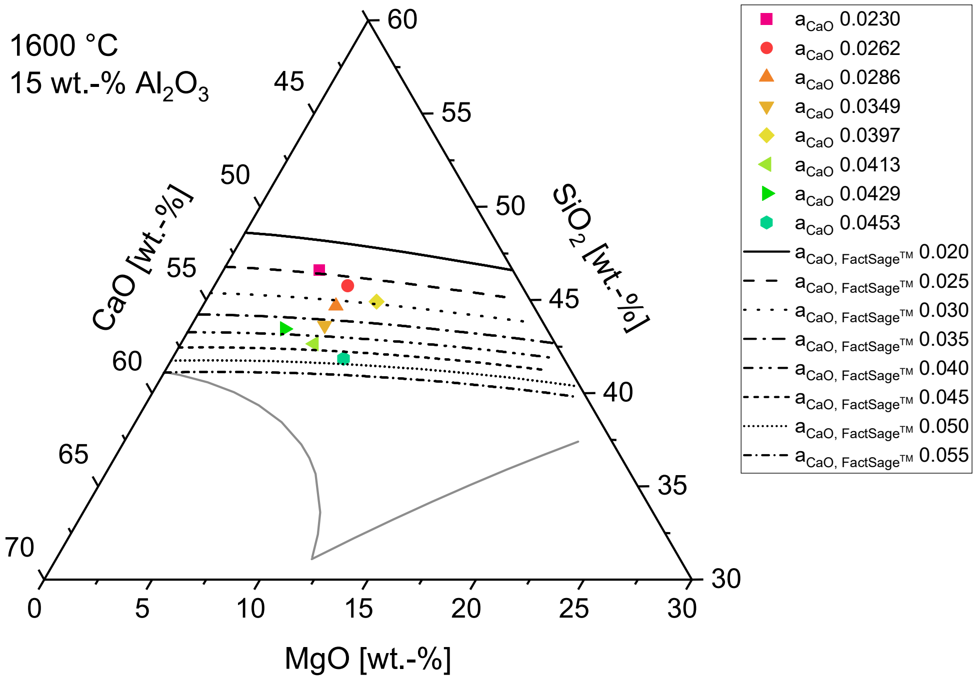

Figure 5-6: Experimentally determined values for a_{CaO} in the system $CaO-Al_2O_3-SiO_2-MgO$ [42]

As Figure 5-6 shows, the experimentally determined activity data of Wen et al. differ more or less from the theoretical ideal values (calculated with FactSage™ 7.3). This might be due to measurement uncertainties in the determination of a_{CaO} of the reference slag. These errors affect the accuracy of $a_{CaO}$of the measured slag.

In [117], Kume et al. determined the activities of CaO, Al_2O_3 and MgO for solid reference state in CaO-SiO_2, CaO-SiO_2-Al_2O_3, CaO-SiO_2-MgO and CaO-SiO_2-Al_2O_3-MgO slags using the equilibrium method. For this purpose, they heated synthetic slags together with a silicon-based alloy in Ar atmosphere in a graphite crucible up to 1550 and 1600 °C, respectively. To prevent excessive evaporation of Ca and Mg, they placed a graphite lid on the crucible. To achieve equilibrium between the metal and slag phase, they kept the test temperature in each case for 18 hours. After equilibrium was reached, the samples were quenched in an argon gas stream and the metal phase was analyzed by inductively coupled plasma spectroscopy. Kume et al. reported in [117] the reactions between the respective slag components and the molten Si alloy as shown in equations 5-3 to 5-5.

$$0.5\, Si(l) + CaO(s) \rightleftharpoons 0.5\, SiO_2(s) + Ca(l) \tag{5-3}$$

$$0.5\, Si(l) + MgO(s) \rightleftharpoons 0.5\, SiO_2(s) + Mg(l) \tag{5-4}$$

$$0.75\, Si(l) + AlO_{1.5}(s) \rightleftharpoons 0.75\, SiO_2(s) + Al(l) \tag{5-5}$$

To calculate the activities, they used relationships for change in standard Gibbs energy in [J/mol]. As shown in equations 5-6 to 5-8.

$$\Delta G^\circ = -R \cdot T \cdot \ln \frac{a_{SiO_2}^{0.5} \cdot \gamma_{Ca\,in\,Si} \cdot x_{Ca}}{a_{Si}^{0.5} \cdot a_{CaO}} = 156000 - 20.0 \cdot T \tag{5-6}$$

$$\Delta G^\circ = -R \cdot T \cdot \ln \frac{a_{SiO_2}^{0.5} \cdot \gamma_{Mg\,in\,Si} \cdot x_{Mg}}{a_{Si}^{0.5} \cdot a_{MgO}} = 134700 - 16.85 \cdot T \tag{5-7}$$

$$\Delta G^\circ = -R \cdot T \cdot \ln \frac{a_{SiO_2}^{0.75} \cdot \gamma_{Al\,in\,Si} \cdot x_{Al}}{a_{Si}^{0.75} \cdot a_{AlO_{1.5}}} = 132100 - 14.31 \cdot T \tag{5-8}$$

γ_i is the activity coefficient of component i in the Si alloy, which Kume et al. taken from Miki et al. reported in [118] and [119], a_i is the activity of component i in the slag, and x_i is the content of component i in the Si alloy. In addition to the activity coefficients, they took the activities of SiO_2 from [120], which enabled them to calculate the activities of CaO, Al_2O_3, and MgO. Figure 5-7 and Figure 5-8 show the measured activity data of Kume et al. from [117] together with the theoretical isoactivities calculated using FactSage™ 7.3.

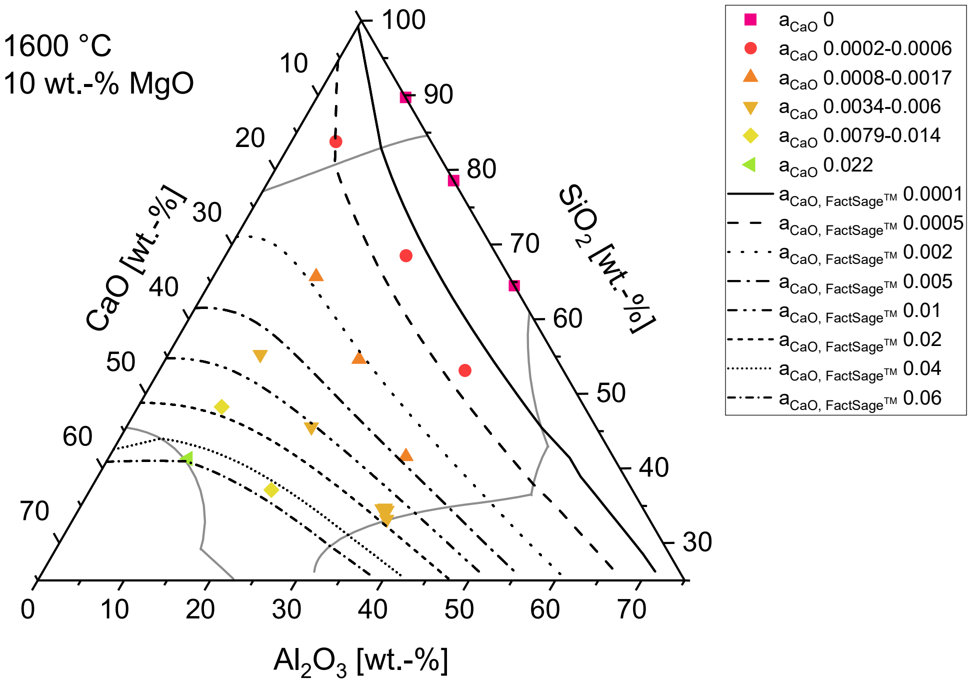

Figure 5-7: Experimentally determined values for a_{CaO} in the system CaO-Al2O3-SiO2-MgO [117]

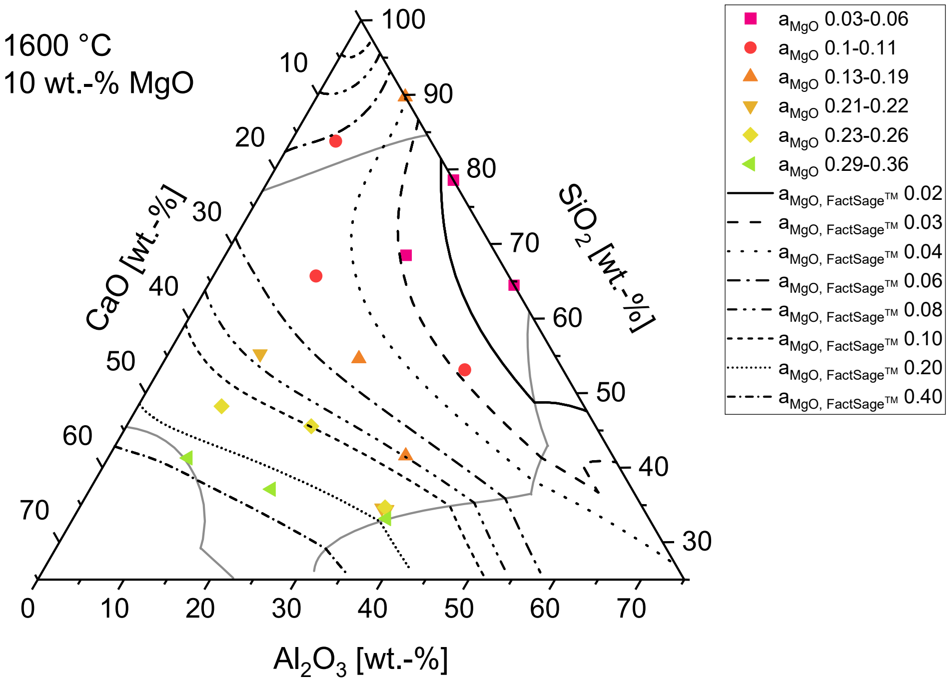

Figure 5-8: Experimentally determined values for a_{MgO} in the system CaO-Al2O3-SiO2-MgO [117]

The differences between the values for a_{CaO} and a_{MgO} experimentally determined by Kume et al. in [117] and the ideal values calculated using FactSage™ 7.3 could be caused by the literature data required for the calculation of the activities.

Jakobson and Tangstad determined in [121] the activities of CaO, MgO and SiO_2 for solid reference state by the equilibrium method in the binary system CaO-SiO_2 and MgO-SiO_2 as well as in the ternary system CaO-MgO-SiO_2. Therefore, they equilibrated the slags with silicon by holding them at 1600 °C for 6 hours under argon atmosphere. After the holding time, the samples were cooled to the melting point of silicon in the furnace within 2 minutes. The metal phase was then separated from the slag phase and analyzed by inductively coupled plasma mass spectrometry. They determined the activity of SiO_2 in the different slag types from the Ca and Mg contents in the metal phase, respectively. In turn, they used these together with self-interaction coefficients of the respective species in silicon from [119] and thermodynamic data from [71] to determine the CaO and MgO activity. In Figure 5-9 and Figure 5-10, the trends for a_{CaO} and a_{MgO} determined by Jakobson and Tangstad in [121] are compared with the isoactivities calculated using FactSage™ 7.3. The data were taken from the diagrams published in [121].

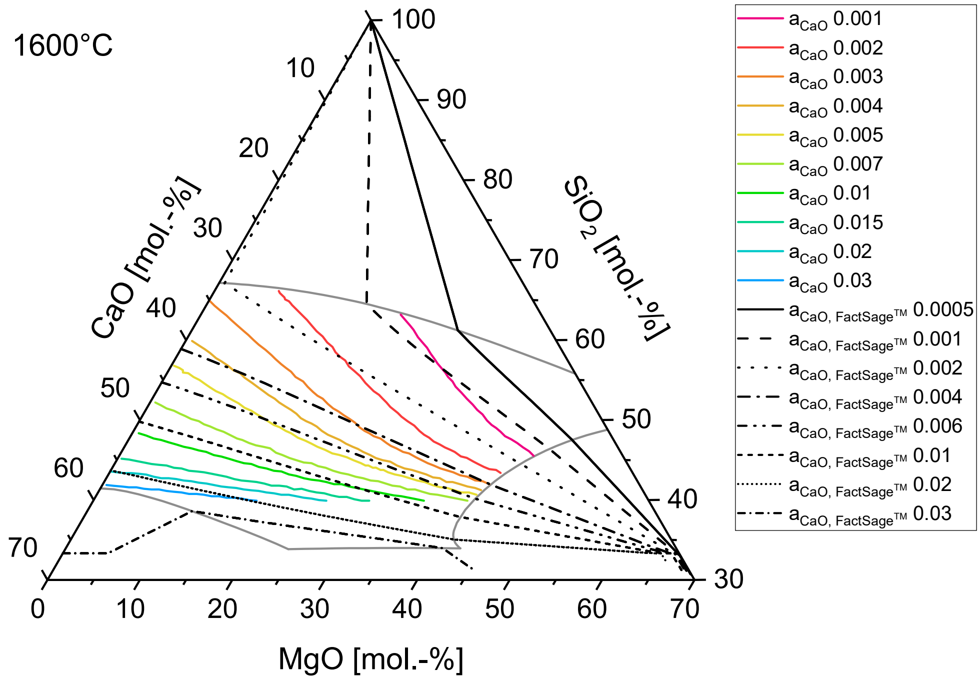

Figure 5-9: Experimentally determined values for a_{CaO} in the system CaO-SiO_2-MgO [121]

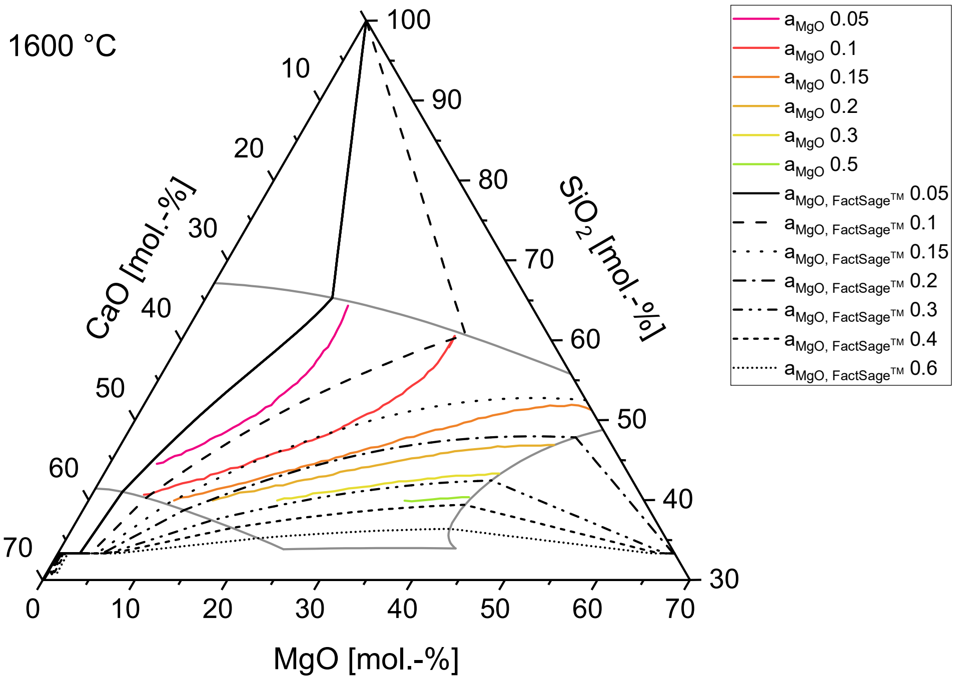

Figure 5-10: Experimentally determined values for a_{MgO} in the system CaO-SiO_2-MgO [121]

The comparison shown in Figure 5-9 and Figure 5-10 illustrates deviations of the experimentally determined activity trends from the ideal ones. For small activity values, the curves determined by Jakobson and Tanstad also show different slopes compared to the curves calculated using FactSage™ 7.3. The deviations here could again be due to the literature values used.

In [52], Stolyarova et al. used Knudsen effusion mass spectrometry to determine the activity of CaO and SiO_2 for solid reference state in the binary CaO-SiO_2 system at 1660 °C. They used a tungsten cell for the measurements. The ionization energy was 70 eV. They used gold to calibrate the KEMS system. a_{CaO} was calculated as shown in equation 5-9.

$$a_{CaO} = \frac{I_{CaO^+}}{I^{\circ}_{CaO^+}} \qquad \text{5-9}$$

I_{CaO^+} and $I^{\circ}_{CaO^+}$ are the measured ion intensities of CaO^+ in the vapor phase above the CaO-SiO_2 system and pure CaO, respectively. For the determination of a_{SiO_2}, they assumed the reaction shown in equation 5-10.

$$SiO_2 \rightleftharpoons SiO + O \qquad \text{5-10}$$

To calculate the required oxygen partial pressure, they used the ratio of the partial pressures of WO_3 and WO_2, also assuming the reaction shown in equation 5-11.

$$WO_3 \rightleftharpoons WO_2 + O \qquad \text{5-11}$$

The calculation of a_{SiO_2} was then performed with the following formula (equation 5-12).

$$a_{SiO_2} = \frac{I_{SiO^+} \cdot \frac{I_{WO_3^+}}{I_{WO_2^+}}}{I^{\circ}_{SiO^+} \cdot \frac{I^{\circ}_{WO_3^+}}{I^{\circ}_{WO_2^+}}} \qquad \text{5-12}$$

I_{SiO^+} and $I^{\circ}_{SiO^+}$ are the measured ion intensities of SiO$^+$ in the mass spectra of the vapor over the CaO-SiO$_2$ system and pure SiO$_2$, respectively. $\frac{I_{WO_3^+}}{I_{WO_2^+}}$ resp. $\frac{I^{\circ}_{WO_3^+}}{I^{\circ}_{WO_2^+}}$ are the ratios of the measured ion intensities of WO_3^+ and WO_2^+ in the vapor phase mass spectra over the CaO-SiO$_2$ system and pure SiO$_2$ in the evaporation processes from the tungsten cell. The values for a_{CaO} and a_{SiO_2} determined in this way, compared to those obtained using FactSage™ 7.3 and using the FToxid as well as FactPS databases, show a positive and negative deviation, respectively. In Figure 5-11, the investigated compositions and the respective measured activities are plotted in the binary CaO-SiO$_2$ system. In addition, the activity curves calculated using FactSage™ are shown.

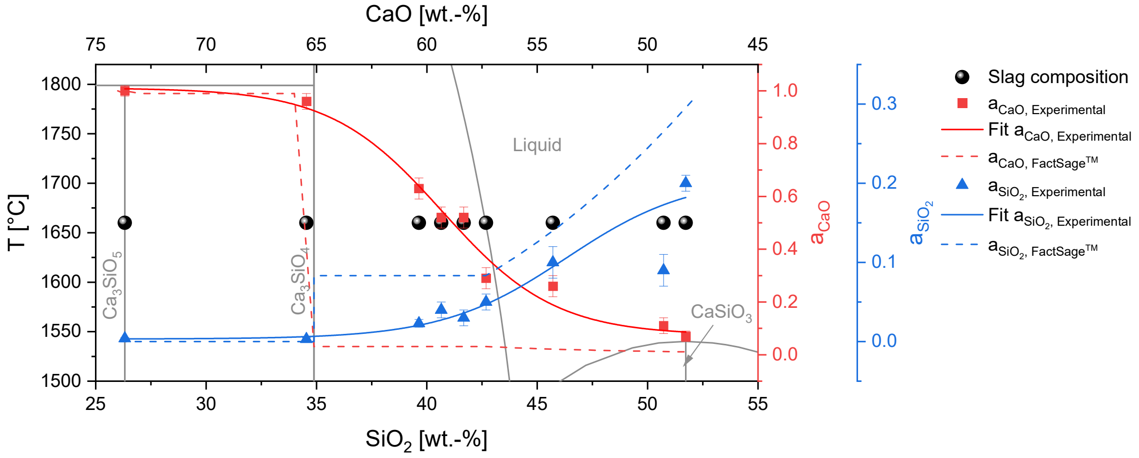

Figure 5-11: Experimentally determined values for a_{CaO} and a_{SiO_2} in the CaO-SiO$_2$ system [52]

A reason for the deviations between the experimental determined activities of Stolyarova et al. in [52] could be the high evaporation rate of SiO$_2$ in the form of SiO and the resulting rapid change of the slag composition. If the SiO$_2$ content in the slag decreases, its activity is reduced and the activity of CaO increases.

In [53], Stolyarova et al. investigated the CaO-Al$_2$O$_3$ system at 1660 °C using KEMS. With the results, they were able to determine the activity of CaO and Al$_2$O$_3$ for solid reference state. They used silver and gold to calibrate the KEMS system. Molybdenum cells were used in the evaporation experiments of the binary system. The ionization energy in the measurement was

70 eV. Stolyarova et al. calculated a_{CaO} and $a_{Al_2O_3}$ using the equations shown in equations 5-13 and 5-14.

$$a_{CaO} = \frac{p_{Ca} \cdot p_O}{p_{Ca}^{\circ} \cdot p_O^{\circ}} \qquad 5\text{-}13$$

$$a_{Al_2O_3} = \frac{{p_{Al}}^2 \cdot {p_O}^3}{{p_{Al}^{\circ}}^2 \cdot {p_O^{\circ}}^3} \qquad 5\text{-}14$$

Here, p_i or p_i° again is the partial pressure of the respective species i above the CaO-Al$_2$O$_3$ system or the individual pure oxide, respectively. They calculated the required oxygen partial pressure p_O for the calculation of the activities as shown in equation 5-15.

$$p_O = K^{\circ} \frac{I_{MoO_3^+} \cdot \sigma_{MoO_2}}{I_{MoO_2^+} \cdot \sigma_{MoO_2}} \qquad 5\text{-}15$$

K° is the equilibrium constant for the reaction below (equation 5-16). σ_{MoO_2} is the ionization cross section, this was determined using Mann's data from [122] and I_i is the measured ion intensity of species i.

$$MoO_3 \rightleftharpoons MoO_2 + O \qquad 5\text{-}16$$

Stolyarova et al. took the thermodynamic data for the calculation of the equilibrium constant from Glushko et al. in [123]. The resulting values for a_{CaO} and $a_{\mathrm{Al_2O_3}}$ show a small deviation compared to the results calculated using FactSage™ 7.3 and the FToxid and FactPS databases. In Figure 5-12, the activity curves given by Stolyarova et al. in [53] are plotted in the binary CaO-Al$_2$O$_3$ system. In addition, the activity curves calculated using FactSage™ are shown.

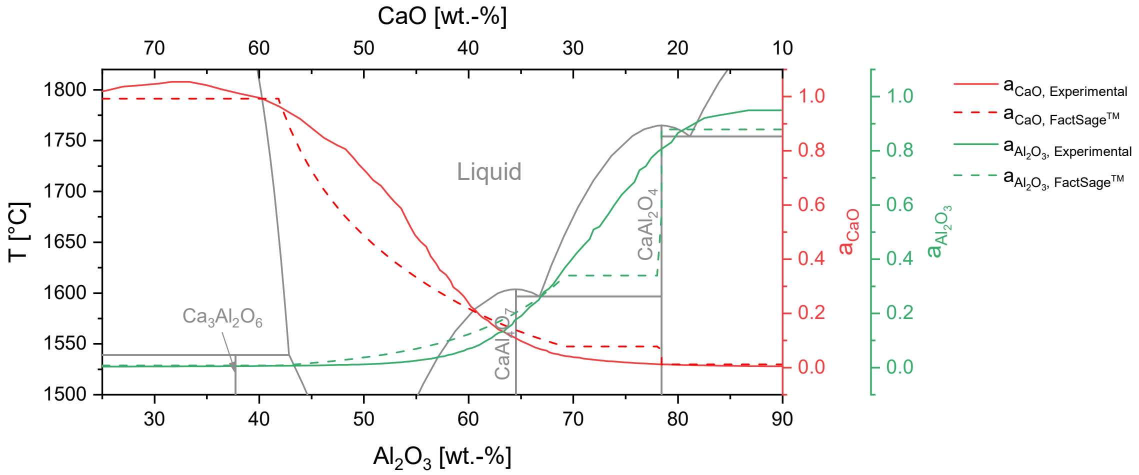

Figure 5-12: Experimentally determined values for a_{CaO} and $a_{Al_2O_3}$ in the system CaO-Al$_2$O$_3$ [53]

The experimentally determined activities of CaO and Al_2O_3 by Stolyarova et al. in [53] show a good agreement with the ideal values calculated with FactSage™ 7.3. While the activity values in [53] show only slight deviations from the ideal values, the values for a_{CaO} and a_{SiO_2} in [52] deviate more clearly from the ideal values. This could be explained by the high evaporation rate of SiO_2 in the form of SiO and thus by a rapid compositional change of the measured samples.

In [124], Stolyarova et al. carried out evaporation experiments with different slags in the CaO-Al_2O_3-SiO_2 system using KEMS. By determining the partial pressures of the different species, they were able to calculate the activities of CaO, Al_2O_3 and SiO_2 for solid reference state at 1660 °C. The mass spectrometer was calibrated by determining the vapor pressures of silver and gold. The ionization energy in the experiments with the different slags was 70 eV. They chose molybdenum as cell material. The calculation of the activity of each slag species is shown in equations 5-17 to 5-20.

$$a_{CaO} = K \cdot \frac{I_{Ca^+}}{I^{\circ}_{Ca^+}} \tag{5-17}$$

$$a_{Al_2O_3} = K^3 \cdot \frac{{I_{Al^+}}^2}{{I^{\circ}_{Al^+}}^2} \tag{5-18}$$

$$a_{SiO_2} = K \cdot \frac{I_{SiO^+}}{I^{\circ}_{SiO^+}} \tag{5-19}$$

$$K = \frac{\frac{I_{MoO_3^+}}{I_{MoO_2^+}}}{\frac{I^{\circ}_{MoO_3^+}}{I^{\circ}_{MoO_2^+}}} \tag{5-20}$$

The measured values for a_{CaO}, $a_{Al_2O_3}$ and a_{SiO_2} determined by Stolyarova et al. in [124] are shown in Figure 5-13 to Figure 5-15 in the CaO-Al_2O_3-SiO_2 ternary system together with the theoretical isoactivities of the different species calculated using FactSage™ 7.3.

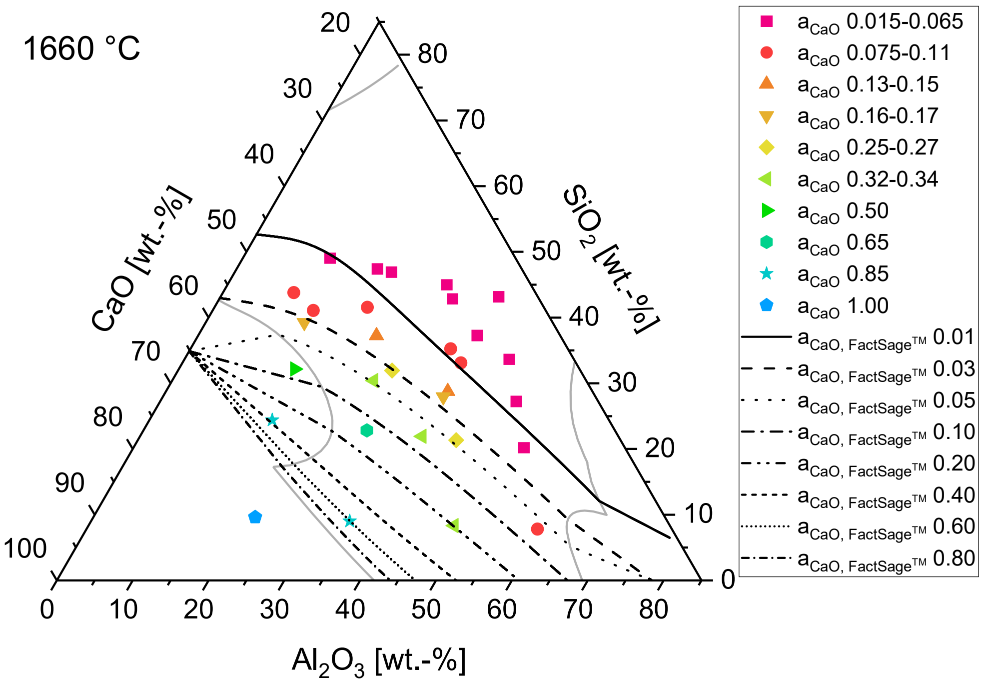

Figure 5-13: Experimentally determined values for a_{CaO} in the system CaO-Al2O3-SiO2 [124]

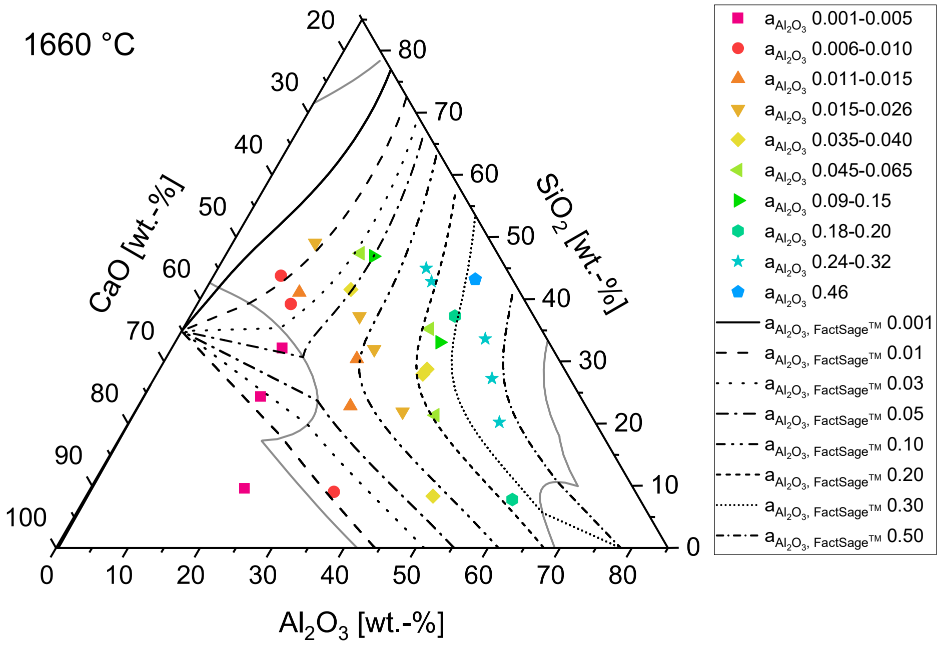

Figure 5-14: Experimentally determined values for $a_{Al_2O_3}$ in the system CaO-Al2O3-SiO2 [124]

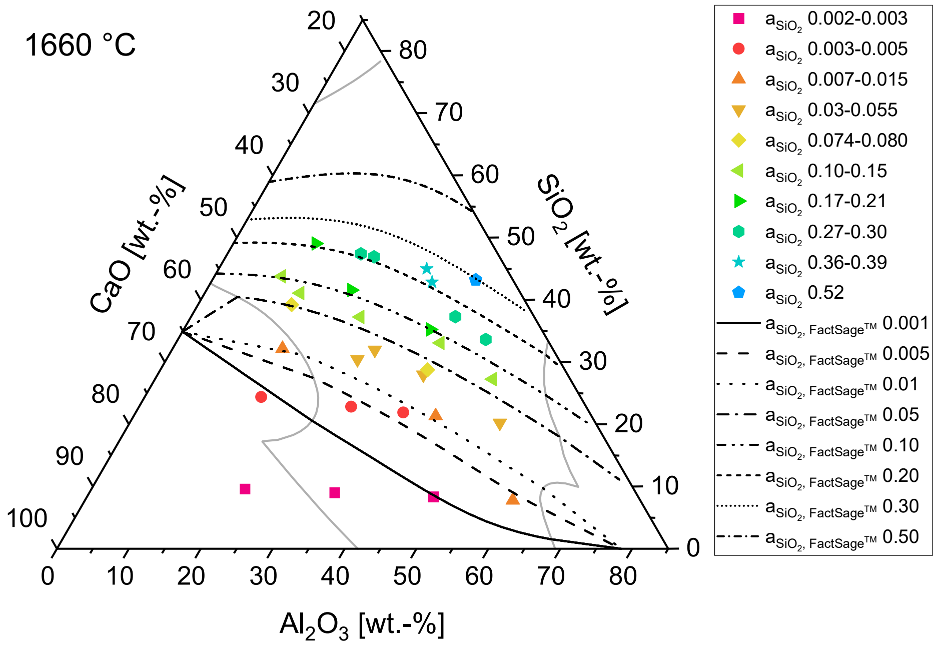

Figure 5-15: Experimentally determined values for a_{SiO_2} in the system CaO-Al_2O_3-SiO_2 [124]

The experimental activity values determined by Stolyarova et al. in [124] show a more or less large deviation from the isoactivities of the different species calculated by FactSage™. These deviations can be explained by the, already mentioned, high evaporation rate of SiO_2 in the form of SiO and the associated rapid change of the slag composition. This would explain why the determined value for the SiO_2 activity was too low in most cases and too high for the CaO and Al_2O_3 activity.

Table 5-XI shows the mean absolute and relative deviation of the results of this study and the previously mentioned authors compared to the calculations of the activity of CaO and MgO in the slag for solid reference state performed with FactSage™ 7.3 using the FactPS and FToxid databases.

Table 5-XI: Deviation between experimentally determined and calculated activities

Slag / Slag system	**Method**	**Species i**	**T / T range [°C]**	**Δa_i [-]**	**Δa_i [%]**	**Source**
BF	KEMS	CaO	1500-1900	-0.0128	51	This study
BF	KEMS	MgO	1500-1900	-0.0643	149	
BOF	KEMS	CaO	1500-1900	0.0066	33	
CA	KEMS	CaO	1500-1900	0.0992	23	
Woll	KEMS	CaO	1500-1900	-0.0236	178	
DS	KEMS	CaO	1500-1900	0.1615	51	
DS	KEMS	MgO	1500-1900	0.2128	51	
DS sat.	KEMS	CaO	1600-1900	0.2944	38	
DS sat.	KEMS	MgO	1600-1900	0.2946	49	
$CaO-SiO_2-Al_2O_3-MgO$	Slag-Metal equilibration	CaO	1600	-0.0006	9	[42]
$CaO-SiO_2-Al_2O_3-MgO$	Slag-Metal equilibration	CaO	1600	0.0065	51	[117]
		MgO		-0.1063	144	
$CaO-SiO_2-MgO$	Slag-Metal equilibration	CaO	1600	-0.0001	18	[121]
		MgO		0.0168	18	
$CaO-SiO_2$	KEMS	CaO	1660	-0.2445	926	[52]
$CaO-Al_2O_3$	KEMS	CaO	1660	-0.0592	29	[53]
$CaO-SiO_2-Al_2O_3$	KEMS	CaO	1660	-0.1345	527	[124]

From this comparison, the small deviations in the results for $a_{CaO}$by Wen et al. from [42] and the large deviations in the results for a_{CaO} by Stolyarova et al. from [52] and [124] compared to the values calculated using FactSage™ 7.3 are especially notable. As already mentioned, the deviations in the results of Stolyarova et al. can be attributed to the high evaporation rate of SiO_2 and the resulting rapid compositional change. In the KEMS investigations of this study, this influence could be reduced, as already mentioned, by shortening the dwell time at the respective measuring temperature and decreasing the general experiment time. If one compares the deviations in the results of the other authors listed in Table 5-XI, no statement can be made as to whether the equilibration method or the KEMS provides more accurate results. However, it can be stated without doubt that the equilibration method, in contrast to the KEMS, is much more widely used for such applications and consequently much better researched.

In contrast to the measurements using the equilibrium method, it should be mentioned again here that the activity determination using KEMS can be performed without any literature values or additional measurements.

6 Summary, conclusion, and outlook

The objective of this work was to determine the diffusion coefficients and activities of CaO and MgO in different slags. For the determination of the diffusion coefficients, dissolution experiments in several slags and at different temperatures were carried out using the rotating cylinder method. Therefore, an experimental setup was designed, which allows to perform experiments under reproducible conditions. Based on the experimental setup, a calculation model was developed allowing the calculation of diffusion coefficients from the data of the dissolution experiments. In addition to the diffusion coefficients of CaO and MgO, those of SiO_2 and Al_2O_3 and the dissolution rate of $MgAl_2O_4$ in a ladle furnace slag at 1550 °C were also determined. For the experimental determination of the activities of CaO and MgO, a method allowing their determination without the need for literature data or further experiments was sought, thus reducing possible sources of error. Taking this requirement into account, an extensive literature study provided Knudsen effusion mass spectrometry (KEMS) as the most suitable method. Using this method, the activities of Ca, CaO as well as Mg and MgO in different slags were determined. Furthermore, the formation enthalpies of CaO and MgO could be calculated.

The results of dissolution tests of CaO and MgO showed that the dissolution rate of oxides in a slag increases with increasing temperature.

The dissolution experiments of Al_2O_3, SiO_2 and $MgAl_2O_4$ in the ladle furnace slag at 1550 °C showed that the spinel dissolves faster than SiO_2 and the latter faster than the Al_2O_3 samples. This was explained by the difference of the bulk and saturation concentration of the slag for the respective oxide and for the spinel dissolution by the size of the diffusing species.

By using the determined dissolution rates as well as geometrical and physical properties of the samples, the diffusion coefficients of the individual oxides in the different slags could be calculated. The diffusion coefficients determined, especially for CaO, show that the slag viscosity alone is not sufficient to describe the influence of the slag composition on the dissolution or diffusion of a species. While the determined effective binary diffusion coefficients of MgO, Al_2O_3 and SiO_2 together with literature data showed a more or less linear relationship with the inverse kinematic slag viscosity, $D_{eff,CaO}$ did not show such a correlation. This in turn indicated that the present data set does not fulfill the Stokes-Einstein relationship due to other parameters dominating the influence of viscosity on diffusion. The analysis of the values for $D_{eff,CaO}$ determined in this work showed a certain linear relationship with the thermodynamic factor of diffusion. Currently, too few data of one slag type are available to find a significant correlation between $D_{eff,CaO}$ and another thermodynamic parameter. Additionally, the comparison of the dissolution rate of $MgAl_2O_4$ showed that the experimental setup has a significant influence on it.

The enthalpy of formation for CaO, determined by KEMS investigations, deviates on average by 10.5 kJ/mol from the usually used -635 kJ/mol. The deviation of the enthalpy of formation of MgO determined in this work from the commonly accepted -601 kJ/mol is on average 3.5 kJ/mol.

The temperature dependence of the activity of Ca, CaO as well as of Mg and MgO in different slags could be determined experimentally using KEMS. Since this method has still been used quite rarely in the sector of metallurgical research, new findings could be obtained from these experiments. For example, the investigation of slag systems containing SiO_2 at high temperatures is problematic due to the high evaporation rate of SiO_2 in the form of SiO and the associated rapid change in composition. This could be overcome by reducing the residence time at the respective measurement temperatures. Furthermore, the measurement of the partial pressure of O and O_2, respectively, is associated with errors due to possible residual gases in the system. This source of error could be eliminated by calculating these partial pressures from those of Ca or Mg. Depending on the slag system and species, the determined activity data show a more or less large deviation from the ideal theoretical values.

A literature review about activity determination of individual components in metallurgical slags showed that the widely used equilibrium method leads to more or less significant deviations from the ideal theoretical values. However, the KEMS is the only method which allows activity determination theoretically without literature data or additional experiments.

As mentioned in the chapter 1 kinetic and thermodynamic models of metallurgical processes are necessary for the creation of digital twins of these. Digitalization enables the estimation and improvement of resource efficiency, therefore the diffusion coefficients and activities determined in this thesis can be used to optimize processes and thereby increase resource efficiency. The calculation model developed to determine the diffusion coefficients allows the calculation of these in a wide variety of slags by implementing a density model and different viscosity models. In addition, the fluid mechanical influence on the diffusivity determination is better represented by the method applied here than in most publications on this topic. The successful use of the KEMS for determining activities in slags has confirmed the suitability of this method for such measurements. This confirmation allows considerations to be made for further slag investigations using KEMS. The measurements carried out with this method could serve as a verification of the results obtained with the most commonly used equilibration method.

The designed experimental setup and the corresponding calculation model for the determination of diffusion coefficients could be used in subsequent studies to determine further diffusion coefficients. The possible variables would be 1) slag composition 2) slag temperature and 3) sample material. As already mentioned, the KEMS could be used for a variety of other investigations of slags, for example for the evaporation behavior of different slag components, the determination of partial pressures and reaction enthalpies. All the quantities determined could be used to improve thermodynamic and kinetic models and thus help to optimize metallurgical processes and increase resource efficiency through digitalization. This would subsequently help to save on input materials and contribute to environmental and climate protection.

Bibliography

[1] M.A. Reuter, Digitalizing the Circular Economy. Metallurgical and Materials Transactions B 47 (2016), 6, pp. 3194–3220. doi:10.1007/s11663-016-0735-5

[2] M. Reuter and A. van Schaik, Opportunities and limits of recycling: A dynamic-model-based analysis. MRS Bulletin 37 (2012), 4, pp. 339–347. doi:10.1557/mrs.2012.57

[3] M.A. Reuter, The simulation of industrial ecosystems. Minerals Engineering 11 (1998), 10, pp. 891–918. doi:10.1016/S0892-6875(98)00078-8

[4] M.A. Reuter, A. van Schaik and J. Gediga, Simulation-based design for resource efficiency of metal production and recycling systems: Cases - copper production and recycling, e-waste (LED lamps) and nickel pig iron. The International Journal of Life Cycle Assessment 20 (2015), 5, pp. 671–693. doi:10.1007/s11367-015-0860-4

[5] N.M. Piatak and V. Ettler, Metallurgical Slags: Environmental Geochemistry and Resource Potential. Cambridge (2021), Royal Society of Chemistry.

[6] B. Burhanuddin, Experimental studies of alumina and magnesia dissolution in silicate and aluminate melts. PhD Thesis, Leoben (May 2022).

[7] D.J. Min and F. Tsukihashi, Recent advances in understanding physical properties of metallurgical slags. Metals and Materials International 23 (2017), 1, pp. 1–19. doi:10.1007/s12540-017-6750-5

[8] F.N.H. Schrama, E.M. Beunder, B. van den Berg, Y. Yang and R. Boom, Sulphur removal in ironmaking and oxygen steelmaking. Ironmaking & Steelmaking 44 (2017), 5, pp. 333–343. doi:10.1080/03019233.2017.1303914

[9] D.M. Ogris and E. Gamsjäger, Numerical Treatment of Oxide Particle Dissolution in Multicomponent Slags with Local Gibbs Energy Minimization. steel research international 93 (2022), 8. doi:10.1002/srin.202200056

[10] F. Verhaeghe, S. Arnout, B. Blanpain and P. Wollants, Lattice Boltzmann model for diffusion-controlled dissolution of solid structures in multicomponent liquids. Physical review. E, Statistical, nonlinear, and soft matter physics 72 (2005), 3 Pt 2, pp. 36308. doi:10.1103/PhysRevE.72.036308

[11] F. Verhaeghe, S. Arnout, B. Blanpain and P. Wollants, Lattice-Boltzmann modeling of dissolution phenomena. Physical review. E, Statistical, nonlinear, and soft matter physics 73 (2006), 3 Pt 2, pp. 36316. doi:10.1103/PhysRevE.73.036316

[12] F. Verhaeghe, J. Liu, M. Guo, S. Arnout, B. Blanpain and P. Wollants, Dissolution and diffusion behavior of Al_2O_3 in a $CaO–Al_2O_3–SiO_2$ liquid: An experimental-numerical approach. Applied Physics Letters 91 (2007), 12. doi:10.1063/1.2786854

[13] F. Verhaeghe, J. Liu, M. Guo, S. Arnout, B. Blanpain and P. Wollants, Determination of the dissolution mechanism of Al_2O_3 in $CaO-Al_2O_3-SiO_2$ liquids using a combined experimental-numerical approach. Journal of Applied Physics 103 (2008), 2. doi:10.1063/1.2830852

[14] R. Sarkar, U. Roy and D. Ghosh, A Model for Dissolution of Lime in Steelmaking Slags. Metallurgical and Materials Transactions B 47 (2016), 4, pp. 2651–2665. doi:10.1007/s11663-016-0659-0

[15] S. Michelic, J. Goriupp, S. Feichtinger, Y.-B. Kang, C. Bernhard and J. Schenk, Study on Oxide Inclusion Dissolution in Secondary Steelmaking Slags using High Temperature Confocal Scanning Laser Microscopy. steel research international 87 (2016), 1, pp. 57–67. doi:10.1002/srin.201500102

[16] I. Barin, Thermochemical data of pure substances. Third edition, Weinheim, New York (1995), VCH.

[17] A.A. Abel, Activity measurement in metallurgical slags. Master Thesis, Freiberg (2020).

[18] World Steel Association AISBL, World Steel in Figures 2023. https://worldsteel.org/steel-topics/statistics/world-steel-in-figures-2023/#crude-steel-production-by-process-2022, Accessed: 08.08.2023

[19] J. Schenk, Eisen- und Stahlmetallurgie I: LV-Nr.: 220.040. Lecture notes, Leoben (2017).

[20] G.C. Wang, Ferrous metal production and ferrous slags, in: The Utilization of Slag in Civil Infrastructure Construction. pp. 9–33 (2016), Elsevier.

[21] A. Ghosh and A. Chatterjee, Ironmaking and steelmaking: Theory and practice. 3. print, New Delhi (2010), PHI Learning.

[22] J. Schenk and C. Bernhard, Eisen- und Stahlmetallurgie II Modul 1: LV-Nr.: 220.041. Lecture notes, Leoben (2019).

[23] S. Amini, Dissolution Rate and Diffusivity of Lime in Steelmaking Slag and Development of Fluoride-Free Fluxes. PhD Thesis, New South Wales (2005).

[24] J. Guarco, H. Harmuth and S. Vollmann, Method for determination of mass transfer coefficients for dissolution of dense ceramics in liquid slags. International Journal of Heat and Mass Transfer 186 (2022), pp. 122494. doi:10.1016/j.ijheatmasstransfer.2021.122494

[25] S. Amini, M. Brungs, O. Ostrovski and S. Jahanshani, Effects of additives and temperature on dissolution rate and diffusivity of lime in Al_2O_3-CaO-SiO_2 based slags. Metallurgical and Materials Transactions B 37 (2006), 5, pp. 773–780. doi:10.1007/s11663-006-0059-y

[26] S. Amini, M. Brungs, S. Jahanshahi and O. Ostrovski, Effects of Additives and Temperature on the Dissolution Rate and Diffusivity of MgO in CaO–Al_2O_3 Slags under Forced Convection. ISIJ International 46 (2006), 11, pp. 1554–1559. doi:10.2355/isijinternational.46.1554

[27] J. Guarco, Burhanuddin, S. Vollmann and H. Harmuth, Sherwood correlation for finger-test experiments. Results in Engineering 15 (2022). doi:10.1016/j.rineng.2022.100610

[28] J. Guarco, Burhanuddin, S. Vollmann and H. Harmuth, Method for determination of effective binary diffusivities in dissolution of dense ceramic materials. Ceramics International 48 (2022), 6, pp. 7456–7463. doi:10.1016/j.ceramint.2021.11.264

[29] W.G. Cochran, The flow due to a rotating disc. Mathematical Proceedings of the Cambridge Philosophical Society 30 (1934), 3, pp. 365–375. doi:10.1017/S0305004100012561

[30] V.G. Levich, Physicochemical Hydrodynamics. New York (1962), Englewood Cliffs, N.J., Prentice-Hall.

[31] A.R. Cooper and W.D. Kingery, Dissolution in Ceramic Systems: I, Molecular Diffusion, Natural Convection, and Forced Convection Studies of Sapphire Dissolution in Calcium Aluminum Silicate. Journal of the American Ceramic Society 47 (1964), 1, pp. 37–43. doi:10.1111/j.1151-2916.1964.tb14638.x

[32] F. Tachibana and S. Fukui, Convective Heat Transfer of the Rotational and Axial Flow between Two Concentric Cylinders. Bulletin of JSME 7 (1964), 26, pp. 385–391. doi:10.1299/jsme1958.7.385

[33] H. Harmuth, Continuous Refractory Wear. Lecture notes, Leoben (2021).

[34] H.J. Merk, Mass transfer in laminar boundary layers calculated by means of a perturbation method. Applied Scientific Research 8 (1959), 1, pp. 237–260. doi:10.1007/BF00411753

[35] J. Xin, L. Gan, N. Wang and M. Chen, Accurate Density Calculation for Molten Slags in SiO_2-Al_2O_3-CaO-MgO-'FeO'-'Fe_2O_3' Systems. Metallurgical and Materials Transactions B 50 (2019), 6, pp. 2828–2842. doi:10.1007/s11663-019-01674-1

[36] S. Vargas, F.J. Frandsen and K. Dam-Johansen, Rheological properties of high-temperature melts of coal ashes and other silicates. Progress in Energy and Combustion Science 27 (2001), 3, pp. 237–429. doi:10.1016/S0360-1285(00)00023-X

[37] R. Pummill, PHYSICAL AND COMPUTATIONAL STUDIES OF SLAG BEHAVIOR IN AN ENTRAINED FLOW GASIFIER. PhD thesis, Utah (August 2012).

[38] T. Iida, H. Sakai, Y. Kita and K. Shigeno, An Equation for Accurate Prediction of the Viscosities of Blast Furnace Type Slags from Chemical Composition. ISIJ International 40 (2000), Suppl, S110-S114. doi:10.2355/isijinternational.40.Suppl_S110

[39] L. Forsbacka, L. Holappa, T. Iida, Y. Kita and Y. Toda, Experimental study of viscosities of selected CaO-MgO-Al_2O_3-SiO_2 slags and application of the Iida model. Scandinavian Journal of Metallurgy 32 (2003), 5, pp. 273–280. doi:10.1034/j.1600-0692.2003.00652.x

[40] M. Kekkonen, H. Oghbasilasie and S. Louhenkilpi, Viscosity models for molten slags. Aalto University publication series SCIENCE+TECHNOLOGY, Aalto (December 2012).

[41] K.C. Mills and S. Sridhar, Viscosities of ironmaking and steelmaking slags. Ironmaking & Steelmaking 26 (1999), 4, pp. 262–268. doi:10.1179/030192399677121

[42] Q. Wen, F. Shen, H. Zheng, J. Yu, X. Jiang and Q. Gao, Activity of CaO in CaO–SiO_2–Al_2O_3–MgO Slags. ISIJ International 58 (2018), 5, pp. 792–798. doi:10.2355/isijinternational.ISIJINT-2017-735

[43] Y. Kang, Sichen, Du and K. Morita, Activities of SiO_2 in Some CaO-Al_2O_3-SiO_2(-10%MgO) Melts with Low SiO_2 Contents at 1873 K. ISIJ International 47 (2007), 6, pp. 805–810. doi:10.2355/isijinternational.47.805

[44] E.T. Turkdogan, SLAG OXYGEN SENSOR. US 6,340,418 B1, United States (Jan. 22).

[45] E.T. Turkdogan, Theoretical concept on slag–oxygen sensors to measure oxide activities related to FeO, SiO_2, and CaO contents of steelmaking slags. Ironmaking & Steelmaking 27 (2000), 1, pp. 32–36. doi:10.1179/030192300677354

[46] M. Iwase, N. Yamada, H. Akizuki and E. Ichise, Activities of Fe_xO in complex slags used during the final stages of external dephosphorization of hot metal. Archiv für das Eisenhüttenwesen 55 (1984), 10, pp. 471–476. doi:10.1002/srin.198405377

[47] M. Miller and K. Armatys, Twenty Years of Knudsen Effusion Mass Spectrometry: Studies Performed in the Period 1990-2010. The Open Thermodynamics Journal 7 (2013), 1, pp. 2–9. doi:10.2174/1874396X01307010002

[48] M. Heyrman, C. Chatillon, H. Collas and J.-L. Chemin, Improvements and new capabilities for the multiple Knudsen cell device used in high-temperature mass spectrometry. Rapid Communications in Mass Spectrometry 18 (2004), 2, pp. 163–174. doi:10.1002/rcm.1298

[49] J. Nakano, T. Nagai, J. Bennett, A. Nakano and K. Morita, A High Temperature Double Knudsen Cell Mass Spectrometry Study of Gas Species Evolved From Coalpetcoke Mixed Feedstock Slags, in: R.G. Reddy, P. Chaubal, P.C. Pistorius, U. Pal (Eds.), Advances in Molten Slags, Fluxes, and Salts: Proceedings of the 10th International Conference on Molten Slags, Fluxes and Salts 2016. pp. 1119–1125, Cham (2016), Springer International Publishing.

[50] M. Allibert, C. Chatillon, K.T. Jacob and R. Lourtau, Mass-Spectrometric and Electrochemical Studies of Thermodynamic Properties of Liquid and Solid Phases in the System CaO-Al_2O_3. Journal of the American Ceramic Society 64 (1981), 5, pp. 307–314. doi:10.1111/j.1151-2916.1981.tb09608.x

[51] C. Chatillon, L.-F. Malheiros, P. Rocabois and M. Jeymond, High-temperature mass spectrometry with the Knudsen cell: II. Technical constraints in the multiple-cell method for activity determinations. High Temperatures-High Pressures 34 (2002), 2, pp. 213–233. doi:10.1068/htjr021

[52] V. Stolyarova, S. Shornikov, G. Ivanov and M. Shultz, High Temperature Mass Spectrometric Study of Thermodynamic Properties of the CaO-SiO_2 System. Journal of The Electrochemical Society 12 (1991), 138, pp. 3710–3714.

[53] V.L. Stolyarova, S.I. Shornikov and M.M. Shultz, High-temperature mass spectrometric study of the thermodynamic properties of the CaO-Al_2O_3 system. Rapid Communications in Mass Spectrometry 9 (1995), 8, pp. 686–692. doi:10.1002/rcm.1290090811

[54] Z.H. Dong, D. Sergeev, D. Kobertz, N. D’Souza, S. Feng, M. Müller and H.B. Dong, Vaporization of Ni, Al and Cr in Ni-Base Alloys and Its Influence on Surface Defect Formation During Manufacturing of Single-Crystal Components. Metallurgical and Materials Transactions A 51 (2020), 1, pp. 309–322. doi:10.1007/s11661-019-05498-1

[55] D. Spathara, D. Sergeev, D. Kobertz, M. Müller, D. Putman and N. Warnken, Thermodynamic study of single crystal, Ni-based superalloys in the γ+γ′ two-phase region using Knudsen Effusion Mass Spectrometry, DSC and SEM. Journal of Alloys and Compounds 870 (2021), pp. 159295. doi:10.1016/j.jallcom.2021.159295

[56] M. Heyrman, I. Nuta and C. Chatillon, Knudsen cell, High Temperature Mass Spectrometry. Miscellaneous Methods and Applications of Elemental MS (2010), pp. 717–729.

[57] K. Hilpert, High temperature mass spectrometry in materials research. Rapid Communications in Mass Spectrometry 5 (1991), 4, pp. 175–187. doi:10.1002/rcm.1290050408

[58] D. Kobertz, M. Müller and A. Molak, Vaporization and caloric studies on lead titanate. Calphad 46 (2014), pp. 62–79. doi:10.1016/j.calphad.2014.02.001

[59] D. Kobertz, Investigations at High Temperature in Both Equilibrium and Kinetic State with Knudsen Effusion Mass Spectrometry (KEMS) and a Skimmer Integrated Coupling System of Mass Spectrometer and Thermal Analysis (STAMS). The Open Thermodynamics Journal 7 (2013), 1, pp. 71–76. doi:10.2174/1874396X01307010071

[60] N. Jacobson, D. Kobertz and D. Sergeev, Introduction to proceedings of the workshop on Knudsen Effusion Mass Spectrometry. Calphad 65 (2019), pp. 111–126. doi:10.1016/j.calphad.2019.01.004

[61] K. Hilpert, Chemistry of inorganic vapors, in: Noble Gas and High Temperature Chemistry. Structure and Bonding. pp. 97–198 .

[62] G.R. Belton and R.J. Fruehan, Determination of activities by mass spectrometry. I. The liquid metallic systems iron-nickel and iron-cobalt. The Journal of Physical Chemistry 71 (1967), 5, pp. 1403–1409. doi:10.1021/j100864a034

[63] D. Raj, L. Bencze, D. Kath, W.A. Oates, J. Herrmann, L. Singheiser and K. Hilpert, Thermodynamic activity measurements in the B2 phases of the Fe–Al and Ni–Al systems. Intermetallics 11 (2003), 11-12, pp. 1119–1124. doi:10.1016/S0966-9795(03)00149-3

[64] A. Neckel and S. Wagner, Massenspektrometrische Bestimmung thermodynamischer Aktivitäten. Berichte der Bunsengesellschaft 2 (1969), 73, pp. 210–217.

[65] L. Bencze, M. Ryś-Matejczuk, E. Yazhenskikh, M. Ziegner and M. Müller, Investigation of Vaporization of Alkali Metals from Solidified Gasifier Slags by Knudsen Effusion Mass Spectrometry. Energy & Fuels 30 (2016), 1, pp. 657–665. doi:10.1021/acs.energyfuels.5b01620

[66] L. Bischof, P.A. Sossi, D. Sergeev, M. Müller and M.W. Schmidt, Quantification of thermodynamic properties for vaporisation reactions above solid Ga_2O_3 and In_2O_3 by Knudsen Effusion Mass Spectrometry. Calphad 80 (2023), pp. 102507. doi:10.1016/j.calphad.2022.102507

[67] J. Drowart and P. Goldfinger, Investigation of Inorganic Systems at High Temperature by Mass Spectrometry. Angewandte Chemie International Edition in English 6 (1967), 7, pp. 581–596. doi:10.1002/anie.196705811

[68] E.H. Copland and N.S. Jacobson, Measuring Thermodynamic Properties of Metals and Alloys, in: Mass Spectrometry Handbook. pp. 1143–1180 .

[69] T. Babeliowsky, A. Boerboom and J. Kistemaker, Mass spectrometric determination of the heat of vaporization of CaO. Physica 28 (1962), 11, pp. 1155–1159. doi:10.1016/0031-8914(62)90061-7

[70] K. Nakajima, Determination of Optimal Vapor Pressure Data by the Second and Third Law Methods. Mass spectrometry 5 (2016), 2, S0055. doi:10.5702/massspectrometry.S0055

[71] Chase, Malcolm, W., Jr., Journal of Physical and Chemical Reference Data: NIST-JANAF thermochemical tables. 4. ed., Woodbury, NY (1998), American Chemical Society and American Institute of Physics.

[72] J. Drowart, C. Chatillon, J. Hastie and D. Bonnell, High-temperature mass spectrometry: Instrumental techniques, ionization cross-sections, pressure measurements, and thermodynamic data (IUPAC Technical Report). Pure and Applied Chemistry 77 (2005), 4, pp. 683–737. doi:10.1351/pac200577040683

[73] I. Barin, O. Knacke and O. Kubaschewski, Thermochemical properties of inorganic substances: Supplement. Berlin, Heidelberg (1977), Springer Berlin Heidelberg.

[74] K.V. Gourishankar, M.K. Ranjbar and G.R. St. Pierre, Revision of the enthalpies and gibbs energies of formation of calcium oxide and magnesium oxide. Journal of Phase Equilibria 14 (1993), 5, pp. 601–611. doi:10.1007/BF02669141

[75] M.A. Duchesne, A.M. Bronsch, R.W. Hughes and P.J. Masset, Slag viscosity modeling toolbox. Fuel 114 (2013), pp. 38–43. doi:10.1016/j.fuel.2012.03.010

[76] P.R. Sahm, I. Egry and T. Volkmann, Schmelze, Erstarrung, Grenzflächen: Eine Einführung in die Physik und Technologie flüssiger und fester Metalle. Berlin, Heidelberg, s.l. (1999), Springer Berlin Heidelberg.

[77] K.C. Mills, M. Hayashi, L. Wang and T. Watanabe, The Structure and Properties of Silicate Slags, in: Treatise on Process Metallurgy. pp. 149–286 (2014), Elsevier.

[78] Y. Waseda and J.M. Toguri, The Structure and Properties of Oxide Melts (1998), WORLD SCIENTIFIC.

[79] M. Valdez, K. Prapakorn, A. W.Cramb and S. Seetharaman, A study of the dissolution of Al_2O_3, MgO and $MgAl_2O_4$ particles in a $CaO-Al_2O_3-SiO_2$ slag. Steel Research 72 (2001), 8, pp. 291–297. doi:10.1002/srin.200100120

[80] B. Yu, X. Lv, S. Xiang and J. Xu, Dissolution Kinetics of SiO_2 into $CaO-Fe_2O_3-SiO_2$ Slag. Metallurgical and Materials Transactions B 47 (2016), 3, pp. 2063–2071. doi:10.1007/s11663-016-0627-8

[81] S. Maroufi, S. Amini, S. Jahanshahi and O. Ostrovski, Diffusion Coefficients and Structural Parameters of Molten Slags, in: R.G. Reddy, P. Chaubal, P.C. Pistorius, U. Pal (Eds.), Advances in Molten Slags, Fluxes, and Salts: Proceedings of the 10th International Conference on Molten Slags, Fluxes and Salts 2016. pp. 493–500, Cham (2016), Springer International Publishing.

[82] A. Halwax, D. Sergeev, M. Müller and J. Schenk, Enthalpy of Formation of Calcium and Magnesium Oxide Obtained by Knudsen Effusion Mass Spectrometry. Metallurgical and Materials Transactions B (2024). doi:10.1007/s11663-024-02995-6

[83] D.W. Bonnell and J.W. Hastie, Program SIGMA. Program SIGMA is available on request, together with σ vs. E coefficient data. IBM PC Executable Format or as Source Code National Institute of Standards and Technology (1990-1997), Gaithersburg, (unpublished work).

[84] K.L. Bell, H.B. Gilbody, J.G. Hughes, A.E. Kingston and F.J. Smith, Recommended Data on the Electron Impact Ionization of Light Atoms and Ions. Journal of Physical and Chemical Reference Data 12 (1983), 4, pp. 891–916. doi:10.1063/1.555700

[85] J.B. Mann, Recent Developments in Mass Spectrometry, in: Proceedings of the Conference on Mass Spectrometry. Tokyo, pp. 814–819, Baltimore (1970), University Park Press.

[86] C.B. Alcock, V.P. Itkin and M.K. Horrigan, Vapour Pressure Equations for the Metallic Elements: 298–2500K. Canadian Metallurgical Quarterly 23 (1984), 3, pp. 309–313. doi:10.1179/cmq.1984.23.3.309

[87] M. Monroe, Molecular Weight Calculator (2014).

[88] W. Lotz, Electron-impact ionization cross-sections and ionization rate coefficients for atoms and ions from hydrogen to calcium. Zeitschrift für Physik 216 (1968), 3, pp. 241–247. doi:10.1007/bf01392963

[89] H. Deutsch, K. Becker, M. Probst and T.D. Märk, Chapter 3 The Semiempirical Deutsch–Märk Formalism, in: Advances in Atomic Molecular and Optical Physics. pp. 87–155 (2009), Elsevier.

[90] D. Margreiter, H. Deutsch and T.D. Märk, A semiclassical approach to the calculation of electron impact ionization cross-sections of atoms: from hydrogen to uranium. International Journal of Mass Spectrometry and Ion Processes 139 (1994), pp. 127–139. doi:10.1016/0168-1176(94)90024-8

[91] R.S. Freund, R.C. Wetzel, R.J. Shul and T.R. Hayes, Cross-section measurements for electron-impact ionization of atoms. Physical review. A, Atomic, molecular, and optical physics 41 (1990), 7, pp. 3575–3595. doi:10.1103/physreva.41.3575

[92] D. Sergeev, E. Yazhenskikh, D. Kobertz and M. Müller, Vaporization behavior of Na_2CO_3 and K_2CO_3. Calphad 65 (2019), pp. 42–49. doi:10.1016/j.calphad.2019.02.004

[93] T. Wakasugi and N. Sano, Re-evaluation of standard free energy of formation of CaO. Metallurgical and Materials Transactions B 20 (1989), 3, pp. 431–433. doi:10.1007/BF02696994

[94] R.L. Altman, VAPORIZATION OF MAGNESIUM OXIDE AND ITS REACTION WITH ALUMINA. The Journal of Physical Chemistry 67 (1963), 2, pp. 366–369. doi:10.1021/j100796a037

[95] S.-M. Liang, A. Kozlov and R. Schmid-Fetzer, The Mg–Ca–O system: Thermodynamic analysis of oxide data and melting/solidification of Mg alloys with added CaO. International Journal of Materials Research 109 (2018), 3, pp. 185–200. doi:10.3139/146.111596

[96] C.E. Holley and E.J. Huber, The Heats of Combustion of Magnesium and Aluminum. Journal of the American Chemical Society 73 (1951), 12, pp. 5577–5579. doi:10.1021/ja01156a020

[97] E.J. Huber and C.E. Holley, The Heat of Combustion of Calcium. The Journal of Physical Chemistry 60 (1956), 4, pp. 498–499. doi:10.1021/j150538a026

[98] C.H. Shomate and E.H. Huffman, Heats of Formation of MgO, $MgCl_2$ $MgCl_2{\cdot}H_2O$, $MgCl_2{\cdot}2H_2O$, $MgCl_2{\cdot}4H_2O$, and $MgCl_2{\cdot}6H_2O$. Journal of the American Chemical Society 65 (1943), 8, pp. 1625–1629. doi:10.1021/ja01248a048

[99] F.D. Rossini, D.D. Wagman, W.H. Evans, S. Levine and I. Jaffe, Selected Values of Chemical Thermodynamic Properties. Washington, D.C. (1952), U.S. Government Printing Office.

[100] T. Deng, J. Gran and D. Sichen, Dissolution of Lime in Synthetic 'FeO'-SiO_2 and CaO-'FeO'-SiO_2 Slags. steel research international 81 (2010), 5, pp. 347–355. doi:10.1002/srin.201000017

[101] T. Deng and Sichen, Du, Study of Lime Dissolution Under Forced Convection. Metallurgical and Materials Transactions B 43 (2012), 3, pp. 578–586. doi:10.1007/s11663-011-9629-8

[102] M. Kosaka and S. Minowa, Mass-Transfer from Solid Metal Cylinder into Liquid Metal. Tetsu-to-Hagane 52 (1966), 12, pp. 1748–1762. doi:10.2355/tetsutohagane1955.52.12_1748

[103] M. Umakoshi, K. Mori and Y. Kawai, Dissolution Rate of Sintered MgO into Molten Fe_tO-CaO-SiO_2 Slags. Tetsu-to-Hagane 67 (1981), 10, pp. 1726–1734. doi:10.2355/tetsutohagane1955.67.10_1726

[104] M. Matsushima, S. Yadoomaru, K. Mori and Y. Kawai, A Fundamental Study on the Dissolution Rate of Solid Lime into Liquid Slag. ISIJ International 17 (1977), 8, pp. 442–449. doi:10.2355/isijinternational1966.17.442

[105] T. Hamano, M. Horibe and K. Ito, The Dissolution Rate of Solid Lime into Molten Slag Used for Hot-metal Dephosphorization. ISIJ International 44 (2004), 2, pp. 263–267. doi:10.2355/isijinternational.44.263

[106] N. Maruoka, A. Ishikawa, H. Shibata and S. Kitamura, Dissolution Rate of Various Limes into Steelmaking Slag. High Temperature Materials and Processes 32 (2013), 1, pp. 15–24. doi:10.1515/htmp-2012-0049

[107] J.-Y. Choi, H.-G. Lee and J.-S. Kim, Dissolution Rate of Al_2O_3 into Molten CaO-SiO_2-Al_2O_3 Slags. ISIJ International 42 (2002), 8, pp. 852–860. doi:10.2355/isijinternational.42.852

[108] Burhanuddin, H. Harmuth and S. Vollmann, Quantification of Magnesia Dissolution in Silicate Melts and Diffusivity Determination Using Rotating Finger Test. Applied Sciences 12 (2022), 24, pp. 12791. doi:10.3390/app122412791

[109] B.J. Monaghan and L. Chen, The Dissolution of Alumina in CaO-SiO_2-Al_2O_3 Slags. steel research international 76 (2005), 5, pp. 348–354. doi:10.1002/srin.200506021

[110] S. Taira, K. Nakashima and K. Mori, Kinetic Behavior of Dissolution of Sintered Alumina into CaO-SiO_2-Al_2O_3 Slags. ISIJ International 33 (1993), 1, pp. 116–123. doi:10.2355/isijinternational.33.116

[111] Y. Lin, B. Yan, Y. Wen, Z. Liang, T. Fabritius and Q. Shu, Dissolution behavior of silica in molten CaO–SiO_2–Fe_2O_3–MgO–MnO slag. Journal of the American Ceramic Society 105 (2022), 6, pp. 3774–3785. doi:10.1111/jace.18346

[112] X. Yu, R.J. Pomfret and K.S. Coley, Dissolution of alumina in mold fluxes. Metallurgical and Materials Transactions B 28 (1997), 2, pp. 275–279. doi:10.1007/s11663-997-0094-3

[113] H. Wang and Sichen, Du, Dissolution of MgO·Al_2O_3 spinel and MgO in CaO-Al_2O_3-MgO-SiO_2 slag under forced convection, DiVA, id: diva2:1141959.

[114] B.J. Monaghan and L. Chen, Effect of changing slag composition on spinel inclusion dissolution. Ironmaking & Steelmaking 33 (2006), 4, pp. 323–330. doi:10.1179/174328106X101547

[115] R. Hagemann, L. Pettsold and P.R. Sheller, The Process of Oxide Non-Metallic Inclusion Dissolution in Slag. Metallurgical and Mining Industry 2 (2010), 4, pp. 262–266.

[116] Burhanuddin and H. Harmuth, Dissolution of Magnesia in Silicate Melts and Diffusivity Determination from CLSM Studies. Applied Sciences 13 (2023), 14, pp. 8458. doi:10.3390/app13148458

[117] K. Kume, K. Morita, T. Miki and N. Sano, Activity Measurement of CaO-SiO_2-$AlO_{1.5}$-MgO Slags Equilibrated with Molten Silicon Alloys. ISIJ International 40 (2000), 6, pp. 561–566. doi:10.2355/isijinternational.40.561

[118] T. Miki, K. Morita and N. Sano, Thermodynamic properties of aluminum, magnesium, and calcium in molten silicon. Metallurgical and Materials Transactions B 29 (1998), 5, pp. 1043–1049. doi:10.1007/s11663-998-0073-3

[119] T. Miki, K. Morita and N. Sano, Thermodynamic Properties of Si–Al, –Ca, –Mg Binary and Si–Ca–Al, –Ti, –Fe Ternary Alloys. Materials Transactions, JIM 40 (1999), 10, pp. 1108–1116. doi:10.2320/matertrans1989.40.1108

[120] K. Morita, K. Kume and N. Sano, A Newly Developed Method for Determining SiO_2 Activity of the Silicate Slags Equilibrated with Molten Silicon Alloys. ISIJ International 40 (2000), 6, pp. 554–560. doi:10.2355/isijinternational.40.554

[121] L.K. Jakobsson and M. Tangstad, Thermodynamic Activities and Distributions of Calcium and Magnesium Between Silicon and CaO-MgO-SiO_2 Slags at 1873 K (1600 °C).

Metallurgical and Materials Transactions B 46 (2015), 2, pp. 595–605. doi:10.1007/s11663-014-0268-8

[122] J.B. Mann, Ionization Cross Sections of the Elements Calculated from Mean-Square Radii of Atomic Orbitals. The Journal of Chemical Physics 46 (1967), 5, pp. 1646–1651. doi:10.1063/1.1840917

[123] V.P. Glushko, L.V. Gurvich, I.V. Weitz, V.A. Medvedev, G.A. Hachkuruzov, V.S. Jungmann, G.A. Bergmann and V.F. Baibuz, Thermodynamic properties of substances. 1-4, Moscow (1978-1982).

[124] V. Stolyarova, S. Shornikov and M. Shultz, High-Temperature Mass Spectrometric Study of the Thermodynamic Properties of the CaO-Al_2O_3-SiO_2 System. High Temperature and Material Science (1996), 36, pp. 15–35.

Nomenclature

A_i	Area	[m^2]
a_i	Activity of component i	[-]
a_{ij}	Interaction factor between component i and j	[cm^3/mol]
B	Mass transfer parameter	[-]
B_2	Binary basicity	[-]
B_4	Four-component basicity	[-]
B_i	Basicity index	[-]
B_i^*	Modified basicity index	[-]
c_0^l	Bulk concentration of the melt of the respective substance	[%]
c_1^l	Concentration of the dissolving species at the solid-melt interface	[%]
c_s^l	Saturation concentration of the melt of the respective substance	[%]
D	Diffusion coefficient	[m^2/s]
D_{eff}	Effective binary diffusion coefficient	[m^2/s]
dm/dt	Mass loss rate	[kg/s]
dr/dt	Dissolution rate	[m/s]
E	Open circuit voltage	[mV]
F	Faraday constant	[A·s/mol]
f	Thermodynamic factor of diffusion	[-]
f_i	Fugacity of component i in a solution	[Pa] or [atm]
f_i°	Fugacity of component i in its standard sate	[Pa] or [atm]
G	Integral molar free energy of a solution at temperature T	[J/mol]
gef_T°	Gibbs energy function	[J/mol·K]

$\bar{G}_i$	Partial molar free energy of component i in solution	[J/mol]
G_i°	Molar free energy of component i in its standard state	[J/mol]
$\bar{G}_i^m$	Partial molar free energy of mixing of component i in solution	[J/mol]
H_{298}°	Enthalpy at 1 bar and 298 K	[J/mol]
H_T°	Enthalpy at 1 bar and temperature T	[J/mol]
I_i	Ion intensity of component i in a solution	[-]
I_i°	Ion intensity of component i in its standard state	[-]
j	Diffusive mass flux	[kg/m^2·s] or [mol/m^2·s]
$\bar{j}_i$	Average mas flow density	[kg/m^2·s]
$K \setminus K_P$	Equilibrium constant	[-]
k	Pressure calibration factor	[-]
k_b	Boltzmann constant	[m^2·kg/s^2·K]
L	Characteristic length	[m]
l	Immersion length	[m]
M_i	Molar mass of component i	[kg/mol]
n_i	Number of moles of component i \ Number of oxygen atoms of species i \ Isotopic abundance of species i	[mol] \ [-] \ [-]
p_i	Partial pressure of component i in a solution	[Pa] or [atm]
p_i°	Partial pressure of component i in its standard sate	[Pa] or [atm]
R	Universal gas constant	[J/mol·K]
r	Radius of diffusing species	[m]
R_1	Mean radius of cylindrical sample	[m]
R_2	Inner radius of crucible	[m]
Re	Reynolds number	[-]
Sc	Schmidt number	[-]
Sh	Sherwood number	[-]
Sh_0	Sherwood number without considering effect of convective component of mass flow on boundary layer thickness	[-]
S_i	Combination of several mass spectrometric constants	[-]
S_T°	Entropy at the standard-state pressure of 1 bar and temperature T	[J/mol·K]
T	Temperature	[K] or [°C]
Ta	Taylor number	[-]
T_R	Reference temperature	[K]
T_S	Temperature shift needed for normalization of viscosity curves	[K]
u	Characteristic flow velocity	[m/s]

V^{EX}	Temperature-independent molar excess volume of the slag	[m^3/mol]
$V_i(T)$	Temperature-dependent partial volume of component i	[m^3/mol]
$V_{i,R}$	Partial molar volume of component i at the reference temperature	[m^3/mol]
V_m	Molar volume of the slag	[m^3/mol]
w_0	Bulk concentration of the melt of the respective substance	[wt.-%]
w_i	Concentration of component i	[wt.-%]
w_s	Saturation concentration of the melt of the respective substance	[wt.-%]
X_i	Molar fraction of component i	[-]
x_i	Sum of molar fractions of glass modifying or amphoteric slag components.	[-]
β	Mass transfer coefficient	[m/s]
γ_i	Activity coefficient of component i	[-]
δ	Effective boundary layer thickness	[m]
Δc	Difference between c_s^l and c_0^l	[%]
ΔG	Change in Gibbs energy	[J/mol]
ΔG°	Change in Gibbs energy (reactants and products in standard state)	[J/mol]
ΔG^m	Integral molar free energy of mixing of a solution	[J/mol]
$\Delta G^\circ_{(T)}$	Change in standard Gibbs energy	[J/mol]
$\Delta_r gef^\circ_T$	Change of Gibbs energy function for the investigated reaction	[J/mol·K]
ΔH_{sub}	Enthalpy of sublimation	[kJ/mol]
$\Delta_f H^\circ_{298}$	Standard enthalpy of formation	[kJ/mol]
$\Delta_r H^\circ_T$	Reaction enthalpy at temperature T	[J/mol]
$\Delta_r H^\circ_{Tm}$	Reaction enthalpy at the mean temperature of the measurement	[J/mol]
$\Delta_r S^\circ_T$	Reaction entropy at temperature T	[J/mol·K]
η	Dynamic viscosity	[Pa·s] or [kg/m·s]
η_0	Hypothetical viscosity of the slag	[Pa·s]
η_{0i}	Hypothetical viscosity of component i	[Pa·s]
Λ	Optical basicity	[-]
Λ^{corr}	Corrected optical basicity	[-]
Λ_i	Optical basicity of component i	[-]
ν	Kinematic viscosity	[m^2/s]
ρ_i	Density	[kg/m^3]
σ_i	Ionization cross-section of species i	[10^{-16} cm^2]
χ_D	Correction factor	[-]
ω	Angular velocity	[rad/s]

Abbreviations

BBHLW	Browning, Bryant, Hurst, Lucas, Wall
BF	Blast furnace
BOF	Basic oxygen furnace
CA	Calcium aluminate
DRI	Direct reduced iron
DS	Desulphurization slag
EAF	Electric arc furnace
EDX	Energy-dispersive X-ray spectroscopy
EMF	Electromotive force
HBI	Hot-briquetted iron
HT-LSCM	High temperature laser scanning confocal microscopy
KEMS	Knudsen effusion mass spectrometry
KF	Kalmanovitch-Frank
LD	Linz-Donawitz
LF	Ladle furnace
LSCM	Laser scanning confocal microscopy
NPL	National Physical Laboratory
PCI	Pulverized coal injection
sat.	Saturated
super sat.	Super saturated
WF	Watt-Fereday
Woll	Wollastonite
Γ_i	Simplexes or complexes

Chemical elements and molecules

$(Mg, Fe)_2SiO_4$	Olivine
$(Mg, Fe)O$	Magnesiowüstite
Ag	Silver
Al_2O_3	Aluminum oxide \ Alumina
Ar	Argon
Au	Gold
B_2O_3	Boron trioxide
C	Carbon
C_2S	Dicalcium silicate (2CaO SiO_2)
Ca	Calcium
CaC_2	Calcium carbide
$CaCl_2$	Calcium chloride
$CaCO_3$	Calcium carbonate \ Limestone
CaF_2	Calcium fluoride
$CaMg(CO_3)_2$	Dolomite
CaO	Calcium oxide \ Lime
CaS	Calcium sulfide
CaSi	Calcium monosilicate
CO	Carbon monoxide
Cr_2O_3	Chromium(III) oxide
CrO	Chromium(II) oxide
Fe_2O_3	Iron(III) oxide \ Hematite

Fe_3O_4	Iron(II, III) oxide \ Magnetite
FeO	Iron(II) oxide \ Wüstite
H_2	Hydrogen
HCl	Hydrochloric acid
K_2O	Potassium oxide
Li_2O	Lithium oxide
Mg	Magnesium
$MgAl_2O_4$	Spinel
MgO	Magnesium oxide \ Magnesia
MgS	Magnesium sulfide
Mn	Manganese
MnO	Manganese(II) oxide
Mo	Molybdenum
MoO_2	Molybdenum dioxide
MoO_3	Molybdenum trioxide
N_2	Nitrogen
Na_2O	Sodium oxide
Ni	Nickel
O	Atomic oxygen
O_2	Molecular oxygen
P	Phosphorus
P_2O_5	Phosphorus pentoxide
Pt	Platinum
S	Sulphur
Si	Silicon
SiC	Silicon carbide
SiO	Silicon monoxide
SiO_2	Silicon dioxide \ Quartz
TiO_2	Titanium dioxide
WO_2	Tungsten(IV) oxide
WO_3	Tungsten(VI) oxide
ZrO_2	Zirconium dioxide

List of tables

List of figures